

**UNIVERSITÀ DEGLI STUDI DI NAPOLI “FEDERICO II”**



**FACOLTÀ DI INGEGNERIA**

**PhD in Aerospace, Naval and Quality Engineering**

**XXII Cycle**

**A study on self-rewetting fluids for heat  
transfer in microgravity**

---

***Ing. Anselmo Cecere***

**Tutor:**

***Ch.mo Prof. Ing. Raffaele Savino***

**Coordinatore:**

***Ch.mo Prof. Ing. Antonio Moccia***

# Contents

Abstract.....	v
Preface .....	vi
List of figures .....	viii
List of tables .....	xi
1 Heat pipe & Self-rewetting fluids .....	1
1.1 Introduction.....	1
1.2 Heat pipe: basically principle and application .....	1
1.3 Operative limit of heat pipe system .....	5
1.4 Marangoni effect.....	8
1.5 Self-rewetting working fluid based on Marangoni effect .....	10
1.6 A review on the experimental result of self-rewetting heat pipes.....	12
2 Marangoni heat pipe: An experiment on board of the MIOsat Italian microsatellite ...	17
2.1 Introduction.....	17
2.2 MIOsat mission.....	17
2.3 Marangoni heat pipe experiment .....	19
2.3.1 Layout of the experimental payload .....	20
2.3.2 Experimental procedure.....	22
2.4 Thermal analyses .....	24
2.4.1 Nadir pointing configuration .....	28
2.4.2 Sun pointing attitude.....	31
2.5 Conclusion .....	33
3 Surface tension measurements .....	35
3.1 Surface tension and wettability.....	35
3.2 Theory of pedant drop method.....	37

3.3	Experimental setup.....	42
3.4	Surface tension measurements.....	47
3.5	Contact Angle Measurements.....	51
3.6	Syntesis.....	52
4	On ground activity in view of the MIOsat mission.....	56
4.1	Introduction.....	56
4.2	Breadboard for the thermal characterization of heat pipe.....	56
4.3	Filling procedure.....	59
4.4	Numerical simulation of groove heat pipe.....	60
4.4.1	Analytic model.....	61
4.4.2	Numerical simulation.....	64
4.4.3	Experimental result.....	67
4.5	A comparative study of different working fluid.....	69
4.5.1	Flow visualization in glass capillary.....	69
4.5.2	Thermal characterization of copper wickless heat pipe.....	74
4.6	Conclusion.....	76
5	Marangoni convection in a shallow cell.....	77
5.1	Introduction.....	77
5.2	Experimental setup.....	77
5.3	Flow visualization.....	79
5.4	Mach Zehnder interferometry.....	81
5.4.1	Index of refraction measurements.....	83
5.4.2	Data processing.....	85
5.4.3	Laboratory results.....	87
5.5	Numerical simulation.....	90
5.6	Two-wavelength Mach Zehnder interferometer: water butanol case.....	96

6 Conclusion and future research .....	101
References .....	102

## **Abstract**

In a number of water alcohols solutions the surface tension is an increasing function of temperature. Such mixtures are generally referred as self-rewetting fluids because convection driven by a reverse Marangoni effect is direct from cold to hot region along liquid-vapour interface. Within two phase heat transfer device, like heat pipes, liquid condensed is spontaneously driven to the hot evaporator improving the thermal performances and increasing the maximum heat flux. The research activities focused on numerical simulation and experimental laboratory for thermal characterization of heat pipe filled with self-rewetting fluids. Measurements of thermo-physical properties, in particular surface tension, have been carried out for several binary and ternary mixtures. A comparison between heat pipe filled ordinary and self-rewetting fluids has been carried out. Flow visualization of self-rewetting fluids has been obtained using optical diagnostic systems.

**KEYWORDS:** Heat Pipe, Marangoni Effect, Self-rewetting fluid, Microgravity Experiment, Interferometry.

# Preface

This work has been developed during the last three years and it is now presented in the form of final dissertation in partial fulfillment of the requirements for the Ph.D. in Aerospace Engineering. The study focused on the self-rewetting fluids, i.e. fluids with unique surface tension properties, as innovative working fluids for heat transfer applications. Self-rewetting working fluids are water alcohols solution that exhibit a reverse Marangoni flow along a liquid-vapor interface. When used as working fluid in two phase heat transfer device, such heat pipes, Marangoni effect driving the liquid towards the hot side increasing the heat transfer limit of the system.

Recently, heat pipe filled with innovative self-rewetting working fluid has been selected for a heat transfer microgravity experiment on board micro-satellite. The main objective of this work is the characterization of these solution when used as working fluid for heat transfer applications.

In the first chapter an overview on self-rewetting fluids as innovative working fluid for heat transfer applications is presented.

In the second chapter the architecture of a flight payload and the experimental procedure of microgravity experiment have been defined. Preliminary thermal analysis has been carried out to calculate the operative temperature of flight payload.

In the third chapter surface tension and contact angle measurements have been carried out for both ordinary and self-rewetting fluid based on binary and ternary mixtures.

In fourth chapter a number of different on-ground activities have been carried out to investigate the thermal performances of heat pipes filled with both ordinary and self-rewetting working fluids.

The finally chapter is devoted to a deeper analysis of the behaviour of self-rewetting fluids in a configuration quite similar to heat pipe applications using optical diagnostic systems.

I would like to express my deep appreciation to my tutor Prof. Raffaele Savino for his full support and guidance throughout the course of these three years. I due my thanks to, Prof. Stephan Van Vaerenbergh of Université Libre de Bruxelles and Prof. Luigi Carotenuto of MARS center for their ever clear discussions.

I owe a great thank to Dr. Diego Paterna and Dr. Mario De Stefano Fumo for his valuable help in this research effort and for their friendship. I would like also to thank my colleague of

Ph.D. course, and friend, Roberto Di Paola for the collaboration in the many research activities performed.

Thanks to Ada for the time spent together, Maria for correcting this thesis (and not only), Tiziana for her love in Bruxelles, and Alessandra (wherever you are, I hope you're well).

I cannot forget to be grateful for the support at home provided by my family, which allowed me to achieve this objective.

**Anselmo Cecere**

## List of figures

Figure 1.1 - Heat pipe thermal cycle. ....	2
Figure 1.2 - Heat pipe applications.....	3
Figure 1.3 - Some typical heat pipe wick structure: homogenous (a-c), composite (d-f). ....	5
Figure 1.4 – Scheme of interface between two immiscible fluids .....	8
Figure 1.5 - Surface tension behaviour and anomalous Marangoni effect in Self-Rewetting fluids.....	11
Figure 1.6 - Marangoni effect at liquid vapor interface. ....	12
Figure 1.7 - Surface tension gradient driven flow directed from cold side to hot side. ....	13
Figure 1.8 - Infrared images of the wickless heat pipes filled with water and binary mixture in normal gravity and low gravity, $P = 12W$ .....	15
Figure 2.1- MIOsat mission.....	18
Figure 2.2 - View of the experimental heat pipe payload on board the MIOsat satellite....	21
Figure 2.3 - Possible accommodation of heat pipes experimental payload. ....	22
Figure 2.4 - Experimental procedure of heat pipes experiment .....	23
Figure 2.5 - Sun-synchronous orbit of the MIOsat satellite. ....	24
Figure 2.6 - MIOsat orbital attitude. a) nadir pointing attitude, b) sun pointing attitude....	25
Figure 2.7 – Orbital scheme for the nadir pointing attitude. a) prospective view, b) lateral view. ....	29
Figure 2.8 - Temperature of the heat pipe radiator during the nadir pointing attitude.....	30
Figure 2.9 - Orbital scheme for the sun pointing attitude. a) prospective, b) lateral view..	31
Figure 2.10 – Variation of earth factor of view during sun pointing attitude.....	32
Figure 2.11 - Temperature of the heat pipe radiator during the sun pointing attitude.....	33
Figure 3.1 – Molecular interaction at liquid-air interface .....	35
Figure 3.2 - Wetting and non wetting contact. ....	36
Figure 3.3 - The pendant drop geometry. ....	38
Figure 3.4 - Experimental configuration with all subsystems .....	43
Figure 3.5 - Tensiometer OCA15+.....	44
Figure 3.6 - Graphic interface of SCA20 software control .....	45
Figure 3.7 - Evaluation of the radius of curvature at the apex of drop.....	46
Figure 3.8 - Surface tension measurements of pure liquids. ....	48

Figure 3.9 - Surface tension measurements of binary mixtures .....	48
Figure 3.10 - Normalized surface tension measurements of binary mixtures .....	49
Figure 3.11 - Surface tension measurements of self rewetting brines .....	50
Figure 3.12 - Sessile drop method for contact angle measurements .....	51
Figure 4.1 - Laboratory breadboard for thermal test of heat pipe. a) prospective view, b) extrude view .....	57
Figure 4.2 – Data acquisition system.....	58
Figure 4.3 - Sketch of the filling facility used to fill heat pipes .....	59
Figure 4.4 - Groove geometry .....	60
Figure 4.5 – a) operative limit of heat pipe b) operative region due to the capillary limit..	63
Figure 4.6 - Sketch for the groove heat pipe used for the numerical simulation.....	64
Figure 4.7 - Geometrical model of groove heat pipe.....	65
Figure 4.8 - Temperature distribution of liquid and vapor at steady state condition. ....	65
Figure 4.9 - Transient variation of the pressure and temperature vapour.....	66
Figure 4.10 - Comparison between experimental, numerical and analytical result. a) capillary limit of heat pipe system, b) thermal resistance at different filling ratio. ....	68
Figure 4.11 - Boiling behaviour of heat pipes filled with water and with self-rewetting fluid in vertical configuration. Input power 18W.....	70
Figure 4.12 - Slug boiling behaviour in water $\alpha = 45^\circ$ . Input power 18W. ....	71
Figure 4.13 - Slug boiling behaviour in self-rewetting fluid $\alpha = 45^\circ$ . Input power 18W. ....	71
Figure 4.14 - Dry-out behaviour in water (horizontal). Input power 18W.....	72
Figure 4.15 - Slug boiling behaviour in self-rewetting fluid (horizontal configuration). Input power 18W.....	72
Figure 4.16 - Digital and thermographic images of glass capillary in horizontal configuration filled with pure FP-40 (a) and with self-rewetting brine FP-40/heptanol solution (b). Input power 18W.....	73
Figure 4.17 - Thermographical image of copper wickless heat pipes with aluminum radiators filled water (top), self-rewetting brine (centre) and self-rewetting fluid (down).....	75
Figure 5.1 - Sketch of shallow cell used for the experiments.....	78
Figure 5.2 - Tracks of aluminum particles seeded in the fluid.....	80
Figure 5.3 - View of two-color mach zender setup developed at MARS laboratory.....	81
Figure 5.4 - Mach-Zehnder experimental set-up .....	82

Figure 5.5 - Change in interference pattern at initial and steady state condition. ....	83
Figure 5.6 - Refractive index measurements. a) water/heptanol, b) water/butanol. ....	84
Figure 5.7 - Routine employed to retrieval the phase by the fringe pattern using FFT. ....	86
Figure 5.8 - Unwrapped phase between steady-state and initial condition. ....	86
Figure 5.9 - Unwrapped phase for pure liquid and water heptanol solution. a) ethanol, b) water, c) water-heptanol. ....	87
Figure 5.10 - Temperature map. a) ethanol, b) water, c)water/heptanol mixture. ....	89
Figure 5.11 - Geometric model of quartz cuvette. ....	90
Figure 5.12 - Scheme of air-liquid interface. ....	91
Figure 5.13 – Numerical results of Marangoni flow – Ethanol. a) Velocity profile, b) temperature map. ....	92
Figure 5.14 - Numerical results of Marangoni flow – Water. a) Velocity profile, b) Temperature map. ....	93
Figure 5.15 - Numerical results of Marangoni flow – Water/heptanol. a) Velocity profile, b) Temperature map. ....	94
Figure 5.16 - Comparison between the three different case. ....	95
Figure 5.17 - Unwrapped iso-phase for water/butanol solution. a) $\lambda_{RED} = 633.3nm$ , b) $\lambda_{BLUE} = 488nm$ . ....	96
Figure 5.18 - Temperature and map concentration for water butanol solution. ....	97
Figure 5.19 - Distribution of liquid surface temperature for water butanol mixture. ....	98
Figure 5.20 - Distribution of liquid surface concentration. ....	99

## List of tables

Table 1-1 Typical heat pipe performance for space application's .....	4
Table 1-2 Propriety of wick materials .....	6
Table 1-3 Classification of fluids from surface tension behavior. ....	26
Table 2-1 MIOsat orbital parameters .....	18
Table 2-3 Mean temperature and fluctuation for the two orbital configuration.....	33
Table 3-1 Contact angle measurements. ....	52
Table 3-2 Thermophysical properties of self-rewetting fluids.....	53
Table 3-3 Comparison of the different working fluid .....	54
Table 4-1 Thermal resistance of glass wickless heat pipe .....	74
Table 4-2 Groove dimension.....	61
Table 4-2 Thermal resistance of glass wickless heat pipe. Input power 18W .....	73
Table 4-3 Thermal resistance of heat pipe filled with water, self-rewetting fluid, and self-rewetting brine.....	75
Table 5-1 Liquid used in the experiment. ....	79
Table 5-2 Coefficient of refractive index with temperature.....	88
Table 5-3 Surface tension derivative used in the numerical simulation. ....	91
Table 5-4 Coefficient of refractive index with mass fraction and temperature.....	97
Table 5-5 Comparison between different self-rewetting solutions and self-rewetting brine... ..	99



# 1 Heat pipe & Self-rewetting fluids

## 1.1 Introduction

Heat pipes are self-contained heat transfer devices offering many advantage in electronic cooling, air conditioning, thermal control of spacecraft and satellites, propulsion, power generation, energy recovering, chemical engineering and other applications. By using the latent heat of vaporization of a working fluid to transfer heat efficiently at a nearly constant temperature, they are able to passively transfer several hundred times the amount of heat energy compared to solid copper.

The development of heat pipe concept originally started with Perkins [1] who initially proposed a concept of the working fluid only in one phase. The Perkins tube was the jumping point for the development of the modern heat pipe, whose concept relied on a wicking system to transport the liquid against the gravity and the condenser. Grover and his co-workers of the Los Alamos Scientific Laboratory independently invented the concept in 1963 and built the first prototypes [2]. Grover also coined the name "*heat pipe*" and stated: "*with certain limitations on the manner of use, a heat pipe can be regarded as a synergistic engineering structure which is equivalent to a material having a thermal conductivity greatly exceeding that of any known metal*".

## 1.2 Heat pipe: basically principle and application

The heat pipe device is an evacuated and hermetically sealed, straight or curved metal tube, with an inner wick structure and a small amount of working fluid in equilibrium with its vapor phase. When one end of the pipe is heated the liquid evaporates or boils absorbing the latent

heat of vaporization. The hot vapour flows to the other side of the tube (at lower pressure and temperature) where it is condensed back into liquid form; a heatsink or another cooling system dissipates the released latent heat (see Figure 1.1).

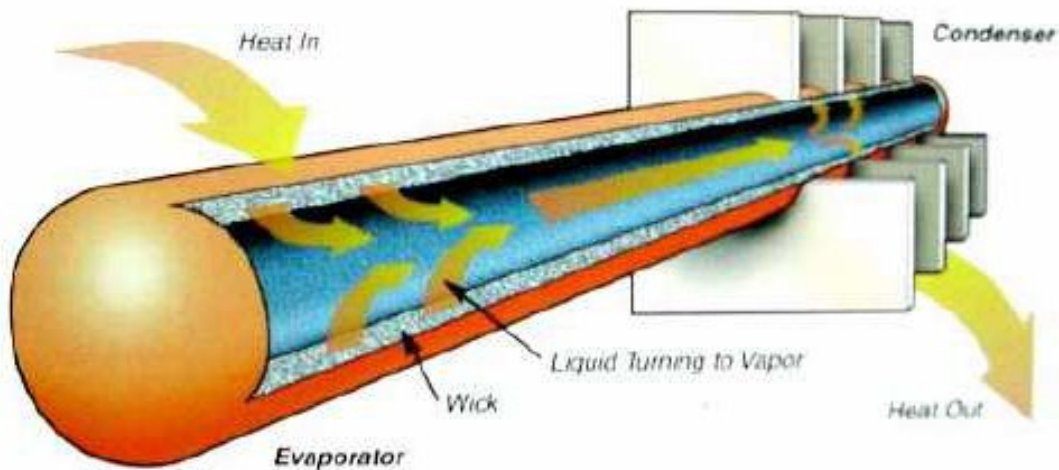


**Figure 1.1 - Heat pipe thermal cycle.**

The recondensed liquid then flows back through the capillary wicking structure to the hot end, resulting in a cyclic evaporation-condensation process. The vapour pressure drop between the evaporator and the condenser is very small and, therefore, the boiling – condensing cycle is essentially an isothermal process.

Since the latent heat of evaporation is usually very large (about 2.26 MJ/Kg for water), a large amount of heat (several orders of magnitude larger than in conventional convective systems with an equivalent temperature difference) can be transported with a very small temperature difference and with small lightweight structures [4].

Today heat pipes are being studied for a wide variety of applications, covering almost the complete spectrum of temperature encountered in heat transfer process. According to the operating temperature ranges heat pipes are referred to as “Cryogenic” (0 to 150 °K), “Low Temperature” (150 to 750 °K) and “High Temperature” (750 to 3000 °K). This work cover only heat pipe systems falling into the category “Low temperature heat pipes”. Figure 1.2 show some typical applications of heat pipes technology [5].

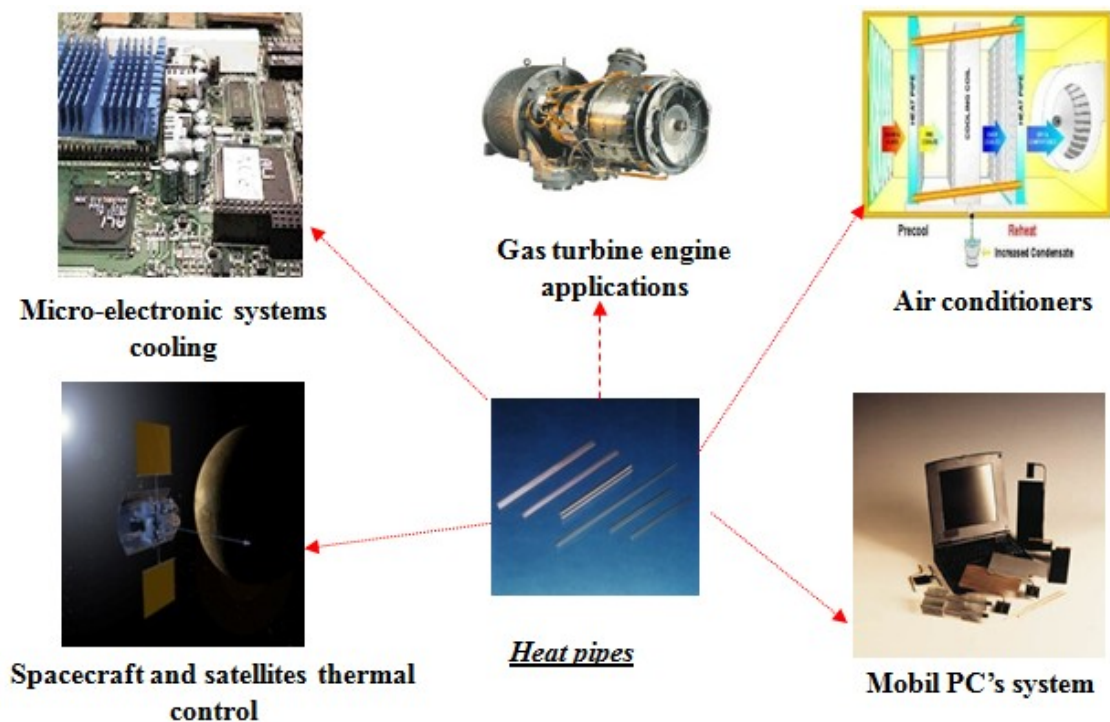


**Figure 1.2 - Heat pipe applications**

In general, because their low-height, zero-maintenance, reliability and high efficiency, heat pipes are used in all heat transfer applications were, due to the requirement of high efficiency and compact size, thermal management is a critical factor and directly influence cost, reliability and performances. Mobil PC's system, micro-electronic system cooling, gas turbine are some typical application of heat pipes technology.

In particular, heat pipe are extensively used from the aerospace designers to solve the ever-present temperature control problems on spacecraft and satellite [6]. Their principal function is to transport heat from dissipative equipment to radiative panels. The common working fluid is ammonia as its operational temperature is well suited to space applications (-40, 80 °C).

Space environment demands that heat pipes respond to particular features:

- high thermal conductivity;
- lightweight and compact design;
- uniform temperature;
- autonomous and reliable concept with no maintenance.

Typical heat pipe performance for space application's are listed in Table 1-1.

**Table 1-1 Typical heat pipe performance for space application's**

Diameters ( <i>mm</i> )	(8 – 25)
Lengths ( <i>m</i> )	0.25 – 4
Linear mass ( <i>g/m</i> )	350/670
Heat Transport capacity ( <i>W m</i> )	50/600
Maximum heat flux density ( <i>W/cm<sup>2</sup></i> )	3/10
Operating temperature range	-40, 80
Life time (years)	15/20
Diameters ( <i>mm</i> )	(8 – 25)
Lengths ( <i>m</i> )	0.25 – 4
Linear mass ( <i>g/m</i> )	350/670

Future missions will require extended heat pipe performances, in particular improvement of the heat transport capacity of at least 15% - 30% and the extension of the maximum operating temperature range to 150°C.

Other type of heat pipe are also manufactured. Flat heat [7] pipe and flexible heat pipe [8] have advantage and drawbacks' respect to the classical cylindrical geometry. For instance, for the flat heat pipe the increased in surface area to volume ratio maximize power density but the thermal resistance increases as the heat pipe becomes more flat, thereby tending to reduce thermal performances. Flexible heat pipes allow for misalignment between heat source and heat sink and can be successfully employed in presence of oscillations and vibrations. Furthermore, flexible systems can be very useful in some applications where relative motion is required (e.g. between movable portions of computers, such as base section and a LCD display of a laptop).

Capillary pumped loop (CPL) and the loop heat pipe (LHP) have been developed to obtain higher pumping capability over long distances at any orientation in a gravitational field or at low-gravity conditions [9-10]. CPLs and LHPs are very similar devices, and in fact represent two extremes out of a spectrum of design possibilities. Instabilities for CPLs and LHPs have demonstrated a deleterious effect on their heat transport capacity and the mechanisms leading to instability are unknown [11]. Obviously, the instability of CPLs and LHPs is one of the major concerns in space applications. The undesirable behavior of the LHPs, such as temperature hysteresis and temperature overshoot during startup, are also serious concerns for

LHPs in space applications. However, both will continue to find applications in space missions [12].

### 1.3 Operative limit of heat pipe system

The simplest heat pipe is a cylindrical straight pipe which is easy to fabricate and has a low cost of production. Basically, the system include:

- 1) a container (sealed and vacuum);
- 2) a wick or capillary structure;
- 3) a working fluid.

The wick structure, responsible for the return of the liquid to the evaporator, can be homogeneous (axial groove, arterial groove, etc.) or composite (screen mesh, wire, etc.), Figure 1.3 illustrates common wicking structure presently in use for heat pipe technology.

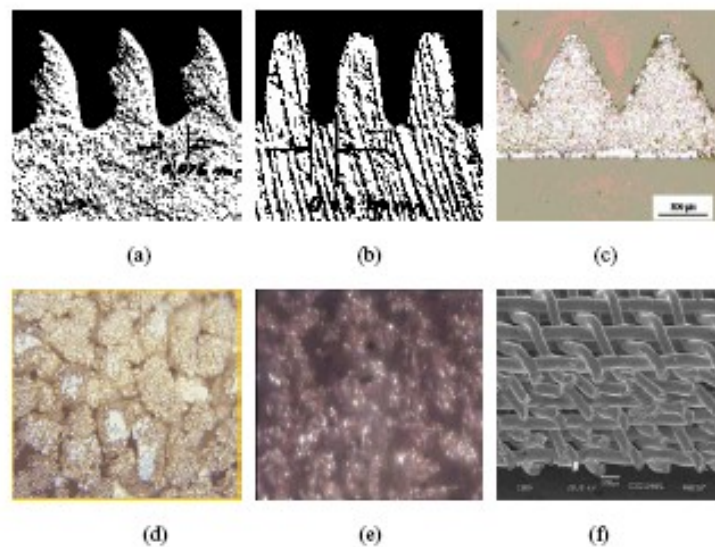


**Figure 1.3 - Some typical heat pipe wick structure: homogenous (a-c), composite (d-f).**

Each wick structure has advantages and drawbacks, see Table 1-2.

**Table 1-2 Propriety of wick materials**

<b>Wicking material</b>	<b>Conductivity (straight)</b>	<b>Overcome gravity</b>	<b>Thermal resistance</b>	<b>Stability</b>	<b>Conductivity lost</b>
Axial groove	Good	Poor	Low	Good	Average
Screen mesh	Average	Average	Average	Average	Low
Fine fiber	Poor	Good	High	Poor	Average
Sintetering (powered)	Average	Excellent	High	Average	High

The temperature range, generally between the triple point and the critical point of the working fluid, determine the choice of the working liquid. The main requirements for a suitable working fluid are compatibility with the materials forming wick and envelope wall, good thermal stability, wettability of wick and wall materials, an operating vapor pressure that is not too high or low over the operating temperature range, high latent heat, high thermal conductivity, low liquid and vapor viscosities, high surface tension and acceptable freezing point.

The container must be lightweight, compatible with the working fluid and must exhibit good thermal conductivity.

Although heat pipe performances and operation are strongly dependent on shape, working fluid and wick structure the fundamental phenomena that governs the operation arises from difference in capillarity pressure across the liquid vapour-interface in the evaporator and condenser . In most of the applications, a serious constraint is the reduction of heat transport capabilities when the condenser is located below the evaporator in a gravitational field, or when the heat pipes are used in low-gravity conditions. The amount of heat exchange that a heat pipe can handle is related to the ability of the condensate liquid layer to counter flow the vaporization process.

For wicked heat pipes the capillary pressure due to the wick structure is responsible for stable working fluid circulation and sets an operational limit with respect to the total pressure drop. When this capillary pressure is not sufficient to promote the flow of liquid from the condenser to the evaporator, the hat pipe is said to have reached his capillarity limit and dry-out of the evaporator occurs.

The net capillary pressure drop between the evaporator and condenser section must be greater than the summation of all the pressure losses occurring throughout the liquid and vapor flow paths [4]:

$$(\Delta p_c)_m \geq \Delta p_v + \Delta p_l + \Delta p_{\perp} + \Delta p_{\parallel} \quad (1.1)$$

where  $(\Delta p_c)_m$  is the maximum capillary pressure difference generated within capillary wicking structure between evaporator and condenser section,  $\Delta p_v$  and  $\Delta p_l$  are the sum of inertial and viscous pressure drops occurring in vapor and liquid phase respectively and  $\Delta p_{\perp}$  and  $\Delta p_{\parallel}$  are the normal and axial hydrostatic pressure drop.

As the heat transfer rate increases the pressure losses in the system increase due to the larger flow rate. The surface temperature at the evaporator section gradually raises, while the outer surface temperature at the condenser section declines. When the capillary pressure is no longer greater than all the pressure gradients across the liquid-vapor path, the liquid layer dries out at the source of heat and the temperature rises immediately at unacceptable values.

The available capillary pressure-pumping head is:

$$(\Delta p_c)_m = \frac{2\sigma \cos \vartheta}{r_{ef}} \quad (1.2)$$

where  $\sigma$  is the surface tension of the working fluid,  $r_{ef}$  is the effective pore radius of the wick,  $\vartheta$  is the effective contact angle, which should be the dynamic contact angle and its value changes with the heat load at the evaporator section. So, the available capillary pressure-pumping head is a function of the surface tension and contact angle of the working fluid that is consequently a key factor for the capillary limit of all heat pipe systems.

During steady-state operation, several other mechanisms can limit the maximum amount of heat that a particular heat pipe can transfer [13]. Among these are the viscous limit, sonic limit, entrainment limit and boiling limit. The viscous limit deal with the pressure drops occurring in the vapor phase. The sonic limit results from the occurrence of choked flow in the vapor passage, while the entrainment limit is due to the high liquid vapor shear stress developed as the vapor passes in a counterflow direction over the liquid-saturated wick. The boiling limit is reached when the heat flux applied in the evaporator portion is so high that

nucleate boiling occurs in the evaporator wick. This create vapor bubbles that partially block the return of fluid and may ultimately lead to a premature dry-out.

Other question regarding the use of heat pipe filling with water in cold ambient. In fact, basically, water, having a large evaporation latent heat and a high surface tension is used in many cases in which heat pipes must operate at moderate temperatures. As a result, in cold climates, the working fluid may freeze when the heat pipe is not under operation.

#### 1.4 Marangoni effect

Marangoni convection arises when there is a variation in the surface tension along a liquid surface. It produces motion from regions of low surface tension towards those at high surface tension (see Figure 1.4).

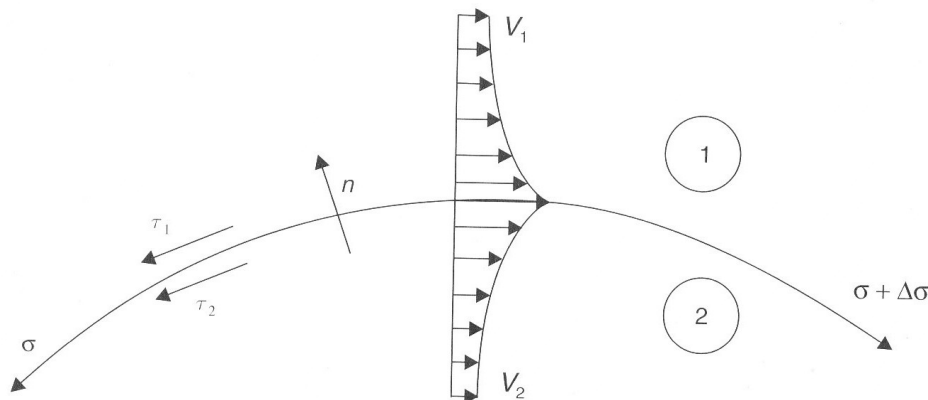


**Figure 1.4 – Scheme of interface between two immiscible fluids**

Marangoni convection can play an important role in many processes involving a non-isothermal interface. For instance, in industrial processes, Marangoni convection reinforces or competes against the normal buoyancy-induced convection. It is very important to analyze accurately the effects of their joint interactions in ground-based processes [14]. Microgravity is a tool well suited for the careful and accurate study of the surface-tension-induced

phenomena that are very difficult to isolate in terrestrial laboratories, and where they are disturbed, even shielded, by gravity effects.

Marangoni flow are caused at liquid-fluid interface by an imbalance of the surface tension. The imbalance may be caused by non-uniformities, along the interface, of the parameters on which the interface tension depend. For a binary mixture, the main parameters on which surface tension depend are the composition and the temperature. In a linear approximation the surface tension variation  $\partial\sigma/\partial x$  along the interface is related to the temperature and specie concentrations by [15]:

$$\frac{\partial\sigma}{\partial x} = \sigma_T \frac{\partial T}{\partial x} + \sigma_c \frac{\partial c}{\partial x} \quad (1.3)$$

So, the Marangoni flow can be the result of concentration and/or temperature gradients. Usually the effect is called solutal Marangoni effect in the case of concentration gradient and thermo-capillary effect in the case of thermal gradient.

In a heat pipe system this effect has show to be detrimental because that surface tension gradients may result in thermo-capillary stresses reducing the wettability of the liquid [16-17]. The experimental results show that heating retards the spreading process by creating thermo-capillary flows and increases the contact angle. These effects arise from the negative-gradient relation of the surface tension with temperature. For most common liquids, including water, the surface tension decreases as temperature increases, and therefore, the liquid body moves towards the region of colder temperature preventing liquid spreading on heated substrates. As a result, the available capillary-pressure-pumping-head decreases as the operating temperature of heat pipe increases. For instance, based on Eq. (1.2), the following equation can be derived:

$$\frac{\partial\Delta p_c}{\partial T} = \frac{2}{r_{ef}} \cos \vartheta \frac{\partial\sigma}{\partial T} - \frac{2\sigma}{r_{ef}} \sin \vartheta \frac{\partial\vartheta}{\partial T} \quad (1.4)$$

Because of a negative value of  $\partial\sigma/\partial T$  and a positive value of  $\partial\vartheta/\partial T$ , the left side of equation is negative, meaning a decrease of the available capillary-pressure-pumping head when the temperature at the evaporator is increased.

Recent efforts have been made to try to enhance heat transfer capabilities through Marangoni effects using binary mixtures [18-19]. A classification of the binary mixtures based on the surface tension behavior has been disclosed in Ref. [20], see Table 1-3.

**Table 1-3 Classification of fluids from surface tension behavior.**

	<b>Single component</b>	<b>Negative Mixtures</b>	<b>Positive Mixtures</b>	<b>Self-Rewetting</b>
$\frac{\partial \sigma}{\partial T}$	<0	<0	<0	>0
$\frac{\partial \sigma}{\partial c}$	-	<0	>0	>0

Generally, a number of different solution with different concentration can be used. For what are termed positive mixtures, the surface tension of the more volatile component is smaller than that of the less volatile component. The Marangoni forces due to a solutal Marangoni effect tend to draw liquid toward the heated surface, resulting in a flow opposite to the thermo-capillary convection for an upward facing heater.

Self-rewetting fluids are particularly solution that allow a reverse Marangoni flow due both to thermo-capillary and solutal Marangoni effect. This liquid will be analyzed in detail in the next paragraphs.

### **1.5 Self-rewetting working fluid based on Marangoni effect**

In general, for all the working fluids used in conventional heat pipes (pure liquids), the surface tension is a decreasing function of the temperature ( $\sigma_T < 0$ ) and this has been shown to be detrimental, because surface motions due to a surface temperature gradient are directed toward the cold regions of the surface, which may be unfavorable for the return of the liquid to the evaporator.

In Ref. [21-25] the use of very dilute alcohol solutions dilute with a high number of carbon atoms (number of carbons atoms  $> 4$ ) such as butanol, pentanol, exanol, heptanol or octanol,

that, according to previous works [26-27], exhibit an anomalous dependency of the surface tension with temperature in some ranges of concentrations, has been proposed as innovative working fluid for heat pipe applications. A patent along this line has been also disclosed [28].

For dilute aqueous solutions of these alcohols, so called self-rewetting fluids, the surface tension, as a function of the temperature, goes through a minimum and there is a range of temperature in which the surface tension increases as shown in Figure 1.5.

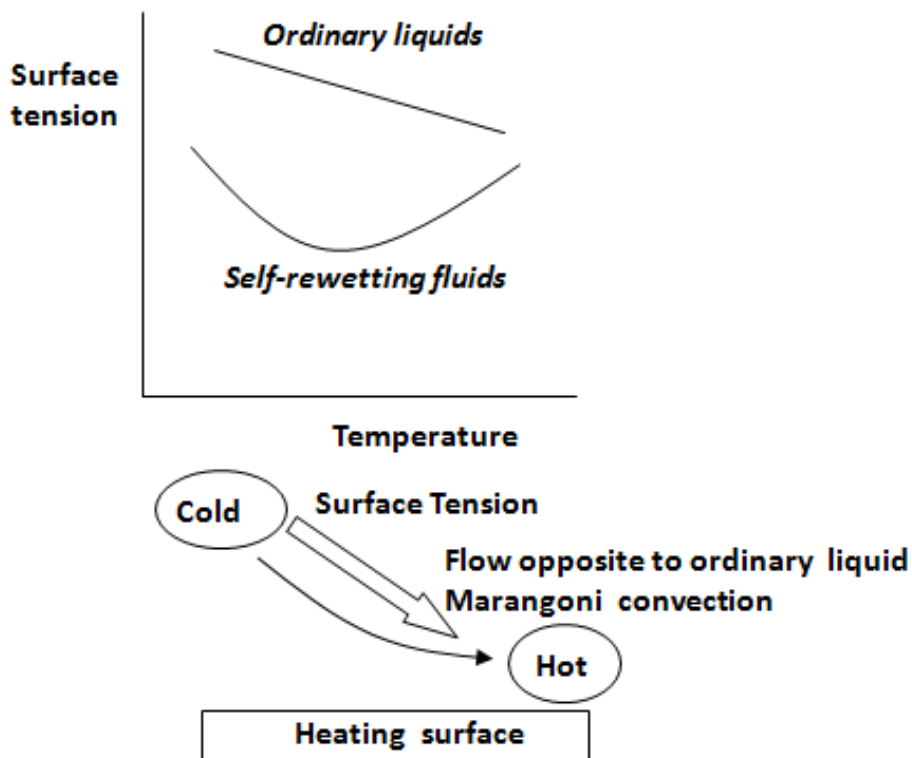


**Figure 1.5 - Surface tension behaviour and anomalous Marangoni effect in Self-Rewetting fluids.**

Therefore, in presence of liquid systems with interfaces and temperature gradients, it is expected to observe surface flows directed from the cold to the hot regions, for temperatures higher than that of the minimum of the surface tension. In addition, since these solutions are in non-azeotropic compositions, alcohol-rich composition preferentially evaporates in the course of liquid/vapor phase change. The surface tension gradient along the liquid-vapour interface, caused by both temperature and concentration gradients, is therefore expected to

spontaneously transport liquid toward hot spot or dry patch on heater surfaces (see Figure 1.6).

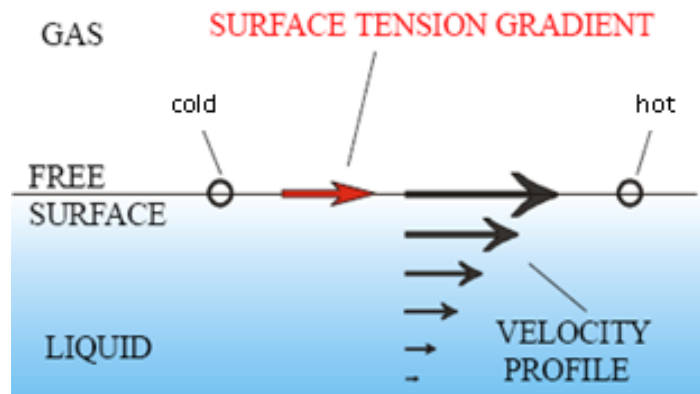


**Figure 1.6 - Marangoni effect at liquid vapor interface.**

The expression “self-rewetting fluid” comes from such particular surface tension-oriented liquid behaviour.

## 1.6 A review on the experimental result of self-rewetting heat pipes

Although the basic aspects of the Marangoni effect are clear, its influence in heat pipes still needs for a more realistic mathematical model and corresponding experimental research. In fact, the role of surface tension becomes dominant in heat and mass transfer processes decreasing the Bond number, i.e. under microgravity conditions and/or reducing the systems size. In these processes, however, surface tension-driven flow has not drawn much attention from the heat transfer point of view, probably due to the fact that the direction of thermocapillary flow is normally directed from interface regions at higher temperature towards lower temperature regions. If the direction of the flow becomes inverse, as in the case of “self-rewetting” fluids or a positive mixtures, the situation can be drastically changed.

Preliminary microgravity experiments in wickless heat pipes were performed in a drop tower in Japan [29-32], using a water–ethanol solution as working fluid (positive mixture) in place of distilled water. In this paper the authors focused their attention in the rewetting problem of the evaporator in wickless heat pipes filled with ethanol/water mixture, so that the evaporation of the more volatile component (ethanol) in the evaporator area could induce a solutal Marangoni flow for the evaporator liquid-supply into wickless heat pipes.

The results pointed out that the condensed liquid in the condenser section is turned back more to the heating section when the ethanol concentration is relatively low. These results could be explained by the Marangoni effect induced by concentration gradients.

The great advantage of self-rewetting fluids is represented by the possibility to develop in the course of liquid/vapour phase change a surface tension gradient driven flow, induced by both temperature and alcohol concentration gradient, direct from the cold region, where liquid condensates, to the hot region (see Figure 1.7) [33].

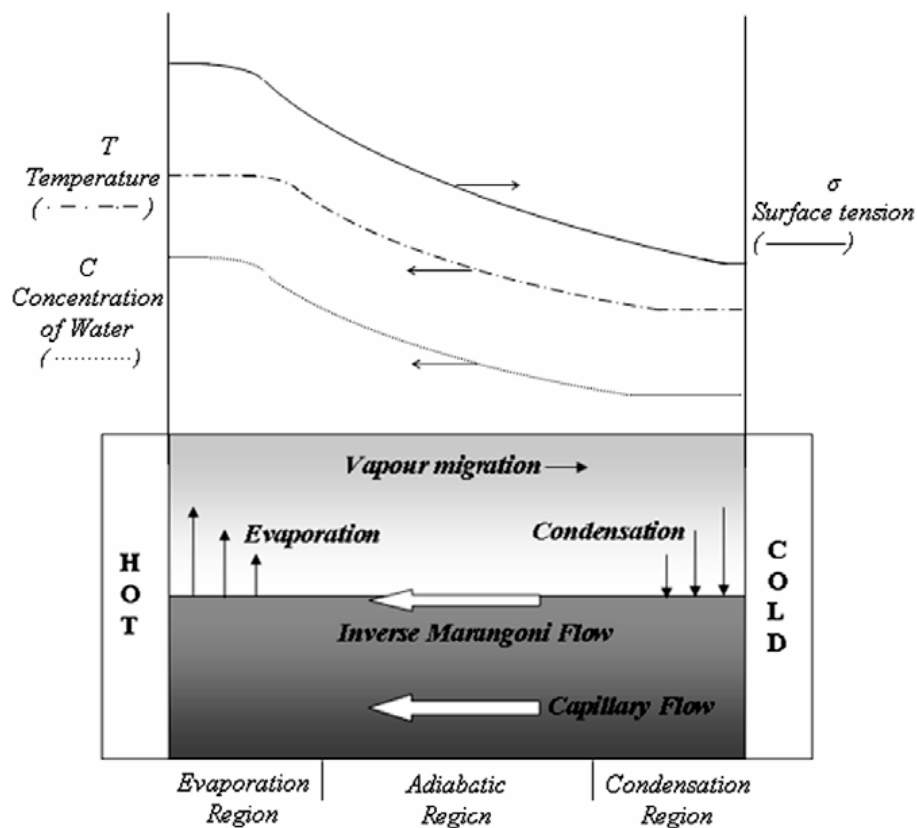


**Figure 1.7 - Surface tension gradient driven flow directed from cold side to hot side.**

The anticipated behaviour of self-rewetting fluids was indeed studied theoretically and numerically in Ref [34-35]. The strong liquid inflow due to reverse Marangoni flow should enhance the capillary pressure head expected with ordinary working fluids and increase the capillarity limit.

A number of research activity has been conducted in recent years to study the behaviour of self rewetting fluids in heat pipe systems [36-38]. Experiments on the thermal performance of wicked tubular heat pipes in horizontal configuration have provided the following experimental evidence: 1) Dryout limit is appreciable, up to 70%, and is increased by the substitution of self-rewetting fluids for water, the most conventional working fluid; 2) thermal performance of self-rewetting fluid heat pipes is fairly uniform with the same specifications compared with that of water heat pipes.

One of the most interesting applications of these studies is the use of self-rewetting fluids in wickless heat pipes under reduced gravity conditions. The particular surface tension characteristics of self-rewetting fluids allow for an enhancement of spontaneous liquid circulation driven by the Marangoni effect due to only thermo-capillary and concentration gradient.

In Ref. [39] a comparative study of heat pipes with different self-rewetting working fluids under microgravity conditions has been carried out during the 45th ESA parabolic flight campaign. A review on the experimental results fluids is also described in references [40]. Figure 1.8 compares the IR images taken in normal gravity and in low gravity for a power  $P=12W$  for two copper wickless heat pipe. The heat pipe on the left is filled with water and the other is filled with aqueous alcohol solution [41].

In the case of the water heat pipe the temperature in the evaporation region appreciably increases in low gravity (and correspondingly the temperature of the condenser decreases). In contrast to this, the temperature distribution of the heat pipe filled with the binary mixture is almost the same in normal gravity and in reduced gravity and its temperature distribution is more uniform. The temperature is almost constant along the adiabatic region of the heat pipe filled with the alcohol solution. On the contrary, the temperature decay along the heat pipe filled with water confirms that dry-out conditions are reached and that the heat pipe is less efficient.

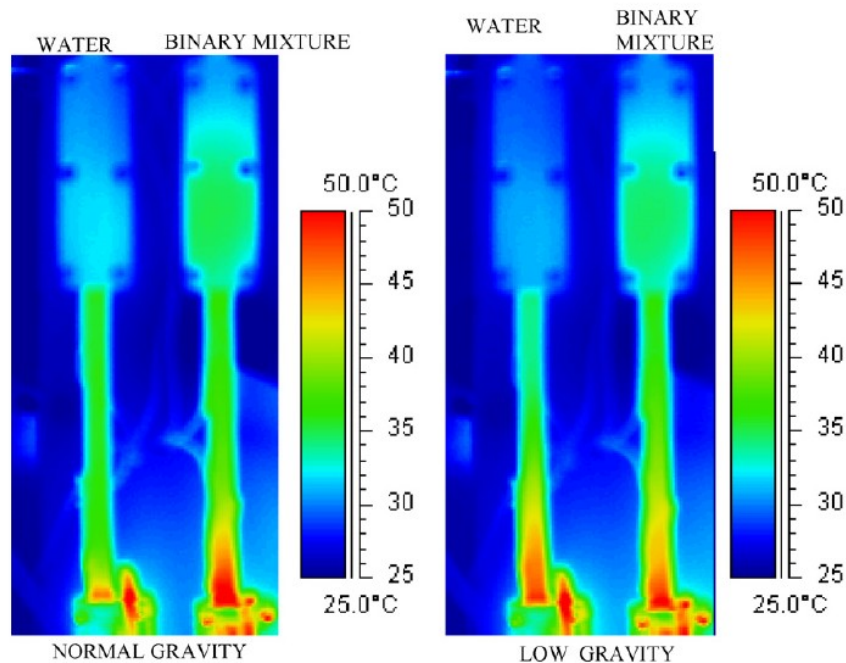


**Figure 1.8 - Infrared images of the wickless heat pipes filled with water and binary mixture in normal gravity and low gravity,  $P = 12W$ .**

The following advantages can be envisaged in comparison with conventional heat pipes with ordinary liquids (e.g. water):

- better thermal performances, in comparison to conventional heat pipes with capillary structures or axial grooves, filled with ordinary liquids (larger heat fluxes and lower thermal resistance);
- identification of liquid solutions with relatively low freezing point (compared to water), able to extend the performances of conventional ammonia-based heat pipes for space applications;
- possibility to use different materials for the heat pipe structure which are not compatible with ammonia but compatible with the selected self-rewetting liquids;
- possibility to develop simple, innovative wickless heat pipes for space applications;
- development of thin lightweight heat pipes;
- development of flexible heat pipes to be used for inflatable and deployable ultra-light weight radiator panels.

This preliminary result have show the potentiality of self-wetting fluid under microgravity conditions. A dedicated experiment is in preparation to be carried out on board an Italian microsatellite as a microgravity platform.

## **2 Marangoni heat pipe: An experiment on board of the MIOsat Italian microsatellite**

### **2.1 Introduction**

MIOsat is a technological and scientific mission based on microsatellite. The main payload is represented by optical instruments for earth observation; however other three small technological experiments have to be integrated in the satellite. Among them, MIOsat will host a dedicated payload to investigate innovative heat pipes filled with self-rewetting fluid to be operated in space under a microgravity environment.

In this chapter a preliminary definition of the flight payload and the experimental procedure have been defined. Preliminary thermal analyses has been carried out to calculate the operative temperature of the flight payload.

### **2.2 MIOsat mission**

MIOSAT (“Missione Ottica su microSATellite”) is a low-cost technological / scientific mission for Earth Observation founded by the Italian Space Agency (ASI). The spacecraft is a microsatellite weighting around 120kg embarking three innovative optical instruments (ALISEO multi spectral radiometer, Mach-Zehender micro-interferometer, and an high resolution panchromatic camera with a deployable telescope). Figure 2.1 show a picture of MIOsat mission.

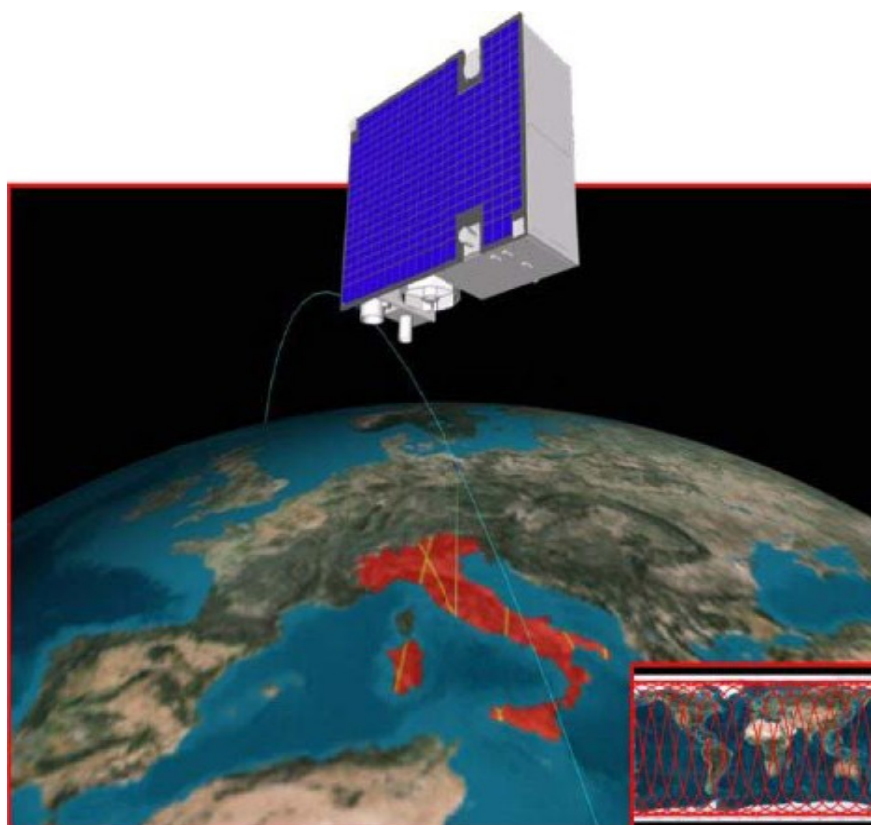


**Figure 2.1- MIOsat mission**

MIOSAT phase B is current ongoing and the launch is scheduled for 2012 on a Vega launch vehicle from Kourou. In Table 2-1 are listed the main orbital parameter of MIOsat mission.

**Table 2-1 MIOsat orbital parameters**

Altitude	500 Km
Eccentricity	0
Inclination	97,4065°
Anomaly of ascendant node	10:30 local hour
9:30 - 10:30 a.m. local time	9:30 - 10:30 a.m. local time
Orbit	polar, sun-synchronous
Expected life-time	2-3 years
Size	1m x 1m x 1m
Mass	Less than 120 Kg
Power	Less than 150 W

MIOSAT satellite will be placed along a sun-synchronous circular LEO orbit, at about 520 km of altitude. The satellite is designed for an operational lifetime of three years. Details on MIOSAT mission and system architecture are given in Ref. [42].

MIOSAT mission has a technological and application objective. Since MIOsat mission has application objectives related to Earth Observation as primary aim (such hydrology and costal resources, cartography, support to Environmental Management in case of natural disasters, etc.), the mission will envisage to demonstrate the feasibility of technologies that have never been flown before on low earth orbit microsattelites. In particular, the satellite will embark three technological experiments to be tested on-orbit. The experiments are:

- 1) Mini Sun Sensor based on COTS components, in CMOS technology
- 2) Reprogrammable GPS/Galileo receiver based on SDR techniques.
- 3) Heat pipe experiment: an heat transfer experiment on self rewetting fluid.

Two attitude configuration are provided for the satellite: a nadir pointing attitude, during this time will be active the main payload of satellite; a sun pointing attitude which will give the possibility to test the three technological payload.

### **2.3 Marangoni heat pipe experiment**

Marangoni heat pipe is a microgravity experiment on heat pipe filled with innovative self-rewetting working fluid [43]. The primary goals of the experiment are:

- 1) investigate on the thermal performances of heat pipe filled with self-rewetting fluid in microgravity environment; in particular to show the advantages related to the reverse Marangoni effect, typical of suitable liquid mixtures with surface tension increasing with temperature (self-rewetting fluids);

2) test an innovative flexible, inflatable and deployable ultra-light weight radiator panel in laminated/polyimide filled with self-rewetting fluid in space ambient.

For this purpose, a number of heat pipes will be manufactured with a conventional metallic structure (copper or aluminium) and will be filled with ordinary and innovative working fluids. One of them will be selected as reference heat pipe and charged with water or ammonia, representing the most common working fluids used in terrestrial or space heat pipes. The other heat pipes will be charged with binary or multi-component self-rewetting solutions with particular surface tension properties.

The experiments will be conducted in parallel on several heat pipes to carry out quantitative comparisons between the performances of the reference heat pipe and those having the same geometry and structure, but filled with self-rewetting fluids.

Furthermore, the comparison between the thermal performances between on-ground and at microgravity condition will give information on the behaviour of self-rewetting fluid in microgravity environment.

The most attractive benefit of the applications of self-rewetting fluids to space thermal management should be the realization of “wickless” heat pipes. The particular surface tension characteristics of self-rewetting fluids allow for an enhancement of spontaneous liquid circulation driven by the Marangoni effect due to only thermo-capillary and concentration gradient. The concept of wickless heat pipe can be extended to an advanced light-weight flexible, inflatable and deployable heat pipe radiator concept [44]. A number of light weight flexible heat pipe radiator concepts have been presented in past decades, but only wickless structure enables one to reduce the weight drastically and realize the concept. This innovative concept will be tested for the first time on board MIOsat satellite.

### **2.3.1 Layout of the experimental payload**

A preliminary definition of the MIOsat flight heat pipe experiment has been carried out during the phase A/B of the MIOsat program. Figure 2.2 shows a view of the experimental payload that will fly on board of the satellite.

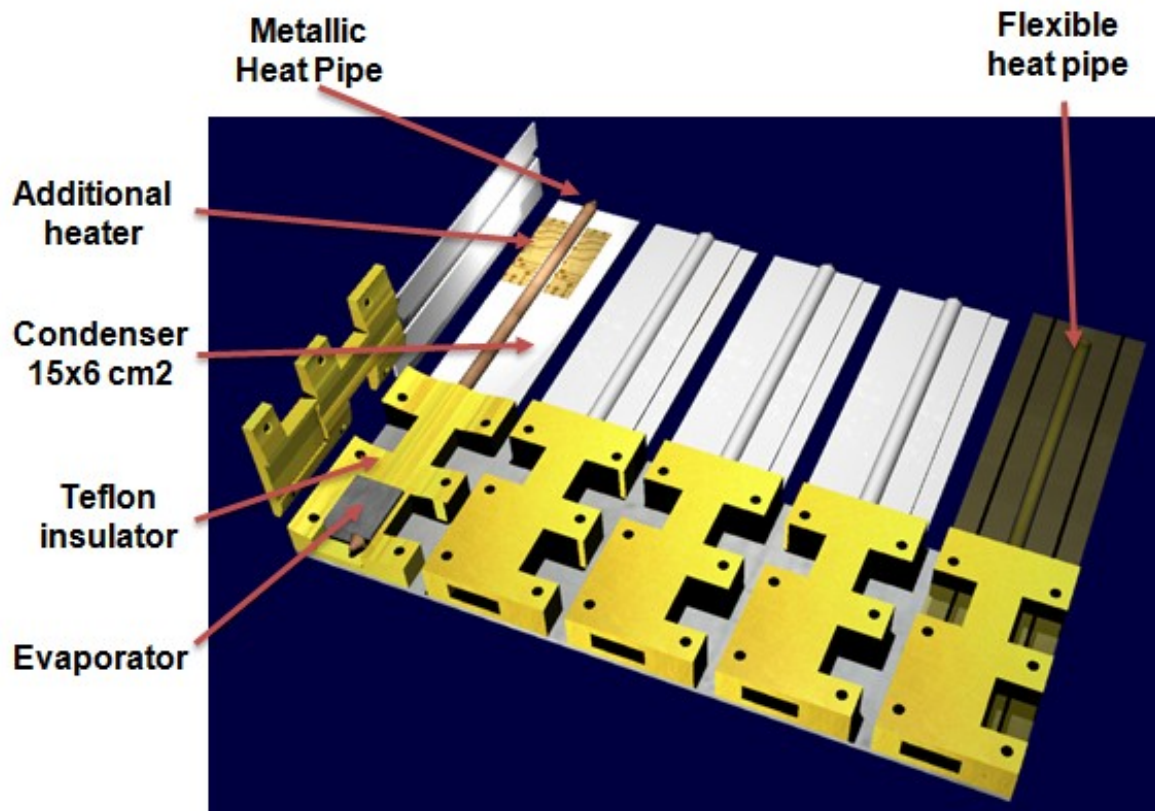
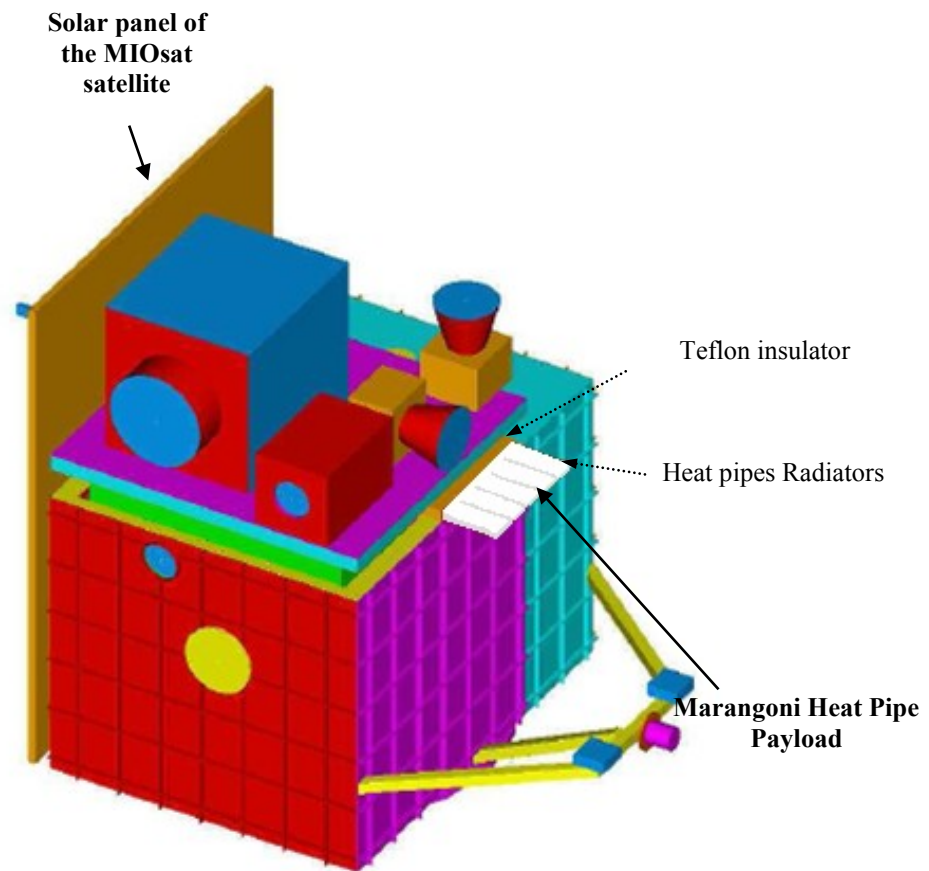


Figure 2.2 - View of the experimental heat pipe payload on board the MIOsat satellite

Heat will be supplied by cartridge heaters at the evaporator sections and dissipated at the condenser sections composed by aluminum radiators, whose frontal area is  $15 \times 6 \text{ cm}^2$ . A high conductivity paste between the heat pipe and the condenser/evaporator sections will optimize the thermal contact between pipe and radiator. In order to maximize the power radiated by the radiators, a thin coat of white paint suitable for space applications will be applied over their surface.

A teflon fixing block as well as insulating washers will minimize the heat loss caused by the heat fluxes exchange between the payload and the satellite. A number of thin thermistors will be used to measure the temperature distribution along each heat pipe, from the evaporator to the condenser.

Figure 2.3 shows a possible accommodation of the experimental payload on the satellite.



**Figure 2.3 - Possible accommodation of heat pipes experimental payload.**

The heat pipes radiators protrude outside from the back face of the satellite. Since the payload is located behind the satellite solar panels, it always looks at the deep vacuum or at earth during the orbit. Therefore it is always cooled at very low temperature, before heaters activation. An additional thin foil kapton heater will be located in the condenser section to warm up the pipe temperature before the experiment execution.

### **2.3.2 Experimental procedure**

The heat pipe experiment will be operated continuously for three orbital periods per day when the satellite is in sun-pointing attitude. The data will be stored by the On Board Data Handling (OBDH) and down linked to ground after the end of each experimental run during the following orbits in S-band. The overall data packet size comes out to be 10 Mbits.

The heat pipe performances will be evaluated measuring the temperatures distributions along two heat pipes simultaneously powered. The power shall be the same for both heat pipes, and shall be controlled for the whole period with a tolerance 0.5 Watt around the setting value, in the range 0 - 50 Watt.

The power levels and heat pipes will be selected by the investigator from ground and the commands sent to the satellite using telecommands arranged in a time-tagged table that the OBDH stores and sends to the payload. At the experiment activation, the OBDH must be able to control the warm-up temperature and activate the additional heater if one of the temperature of the selected heat pipes is below a TBD set temperature (in the range between 10 and 30°C) value. The OBDH will keep active that additional heater until all temperature readings of the selected heat pipes exceed this value (see Figure 2.4).

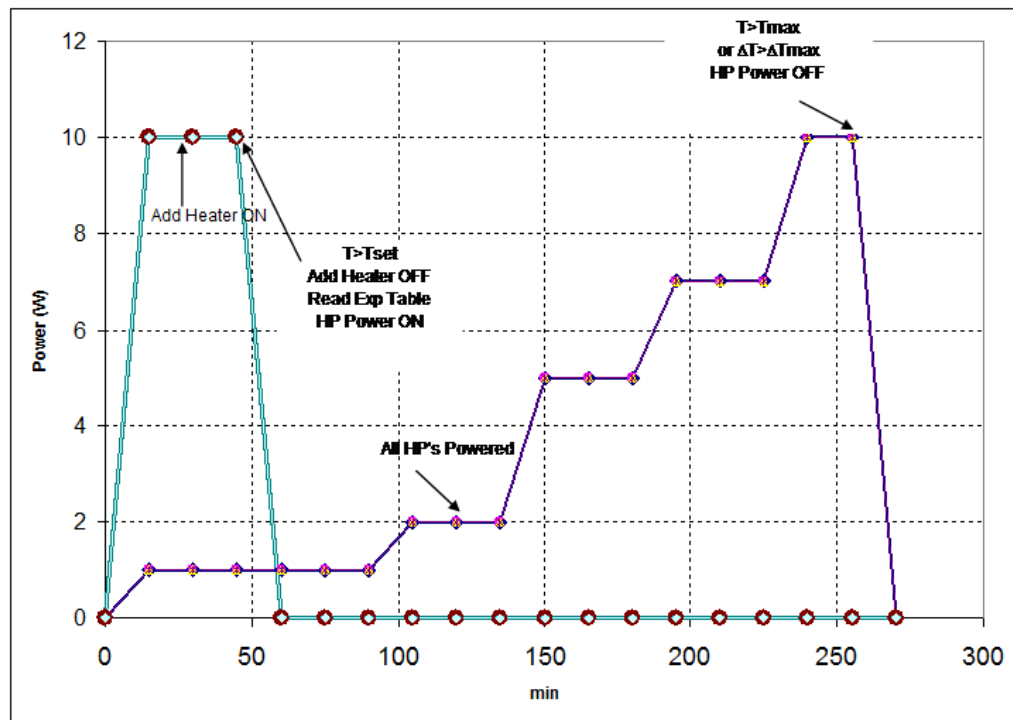


**Figure 2.4 - Experimental procedure of heat pipes experiment**

Then, OBDH has to switch-off the additional heater. Eventually the additional heater can be switched off if it is still active after a certain time and no warm up has been fully reached.

## 2.4 Thermal analyses

Marangoni heat pipe payload will be accommodate on the external surface of the MIOsat satellite (see Figure 2.3), so the operative temperature of the payload depend on the condition of the external environment. Preliminary thermal analyses have been carried out to calculate the operative temperature of the payload during the experiment.

MIOSAT will move on a sun-synchronous orbit, the major characteristic of a sun-synchronous orbit is that the inclination between sunrays and orbit plane is constant (Figure 2.5), so it is always possible to know how much sun illumination meets with each satellite's wall during its orbital motion.

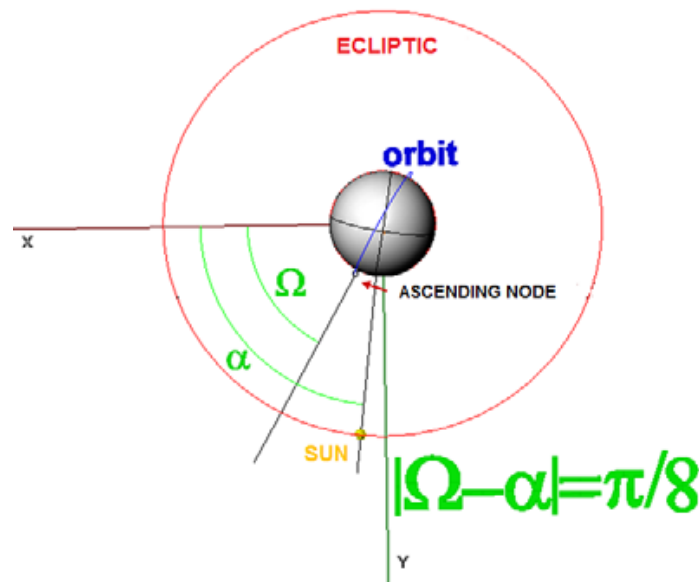


Figure 2.5 - Sun-synchronous orbit of the MIOsat satellite.

Because of the local hour at the ascending node is 10.30 a.m., the angle between the right ascension of the ascending node ( $\Omega$ ) and the right ascension of the Sun ( $\alpha$ ) is  $\pi/8$ . This value is constant during the time.

Thermal analysis has been carried out for both the attitude configuration of the MIOsat satellite using a simplified scheme. The microsatellite has been considerate as a cubic block, one of the six face is the solar panel of the satellite that obscure the other face when the satellite is in sun-pointing attitude. Figure 2.6 show a scheme of the two considered attitude configurations.

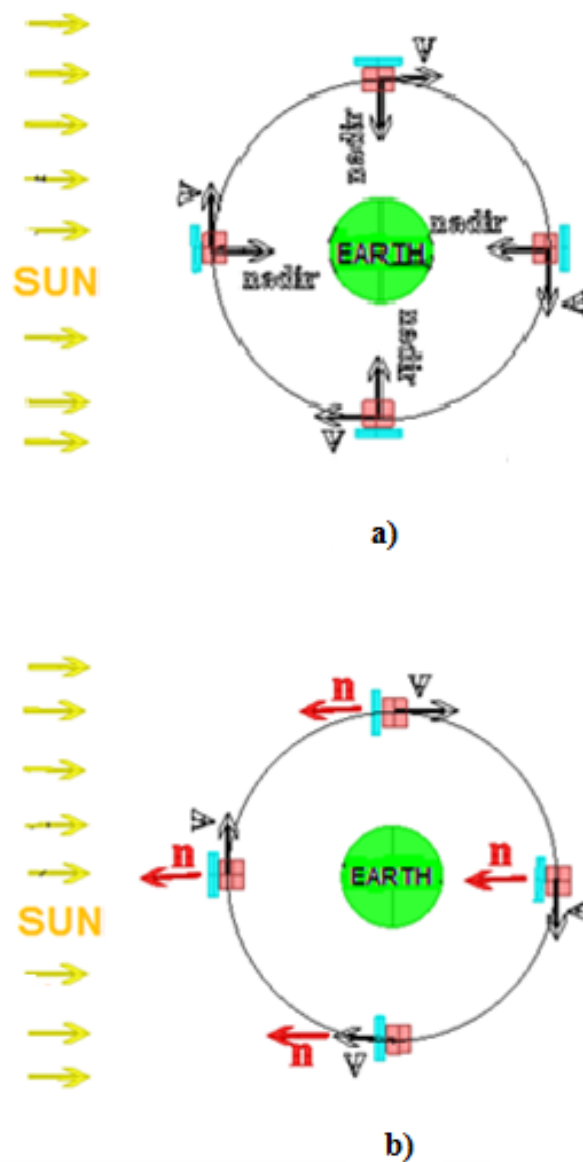


Figure 2.6 - MIOsat orbital attitude. a) nadir pointing attitude, b) sun pointing attitude.

When satellite is sun pointed, his solar panel is perpendicular to solar rays; when satellite is nadir pointed, one of his walls is constantly perpendicular to nadir direction.

The heat pipes will be put on one of the internal walls, parallel to it, so only radiators are exhibited to external environment. Transient thermal analyses have been carried out for heat

pipe radiator by using a lumped approach. Table 2-2 summarizes the optical and thermal properties of heat pipe radiator used in analysis.

**Table 2-2 Thermal and optical property of heat pipe radiator.**

Density $\rho$ (Kg/m <sup>3</sup> )	Specific heat $Cp$ (j/KgK)	Emissivity $\epsilon_{IR}$	Absorbance $\alpha_S$
2700	929	0.975	0.214

The white painting foreseen in the space payload will guarantee a relative high emissivity in the infrared spectrum and a relatively low absorbance in visible range.

The reference equation for the thermal balance is [45-46]:

$$mc \frac{dT}{dt} = -\epsilon_{IR} \tilde{\sigma} 2A_{RAD} T^4 + Q \quad (2.1)$$

Where  $\tilde{\sigma}$  is the constant of Stefan-Boltzmann (in this work has been indicated with the symbol  $\tilde{\sigma}$  to distinguish from the surface tension),  $\epsilon_{IR}$  the infrared emissivity,  $A_{rad}$  the area of the heat pipe radiator, and  $Q$  the instantaneous power stored by the radiator.

Since the satellite will move on LEO orbit the main heat sources are:

1) solar radiation:

$$Q_{SUN} = G_S A_{RAD} \alpha_S \theta_S \quad (2.2)$$

where  $\theta_S$  is the angle between surface radiator and Sun and  $G_S$  is the solar constant ( $G_S = 1423 \text{ W/m}^2$ ).

2) albedo; is the sun radiation reflected by the earth.

$$Q_{ALBESO} = G_S A_{RAD} \alpha_S \theta_S K_A \quad (2.3)$$

$K_A$  is the albedo factor ( $K_A = 0,3$ ).

3) infrared earth emissivity; the earth has been modeled as a black body at 280K. The power stored by radiator is:

$$Q_{EARTH} = F_{EARTH} \varepsilon_{IR} \tilde{\sigma} 2A_{RAD} T^4 \quad (2.4)$$

where  $F_{EARTH}$  is the earth factor of view between the Earth and surface radiator.

In addition, the power exchanged between the payload and the satellite has been evaluated considering the wall of the satellite, with a temperature of 210K, perpendicular to one of the wall radiator:

$$Q_{PAR} = F_{PAR} A_{RAD} \varepsilon_{IR} \sigma T^4 \quad (2.5)$$

The instantaneous power stored during the eclipse period is:

$$Q = Q_{EARTH} + Q_{PAR} + Q_{SP} \quad (2.6)$$

and:

$$Q = Q_{SUN} + Q_{EARTH} + Q_{SUN} + Q_{ALBEDO} + Q_{SP} \quad (2.7)$$

during the no eclipse period. In this equation has been included the power dissipated by radiator towards the deep space ( $Q_{SP}$ ).

The  $Q$  variation depends on orbital motion, too. In fact, during the no eclipsed period  $Q_{SUN}$  can be zero if the considered satellite wall doesn't see the Sun. The same can happen for  $Q_{EARTH}$  or  $Q_{ALBEDO}$  if the wall is opposite to the Earth. So it's important to analyze how the Sun's and Earth's factor of view change during the orbital motion.

The Sun's factor of view is  $\cos \vartheta_S$ , where  $\vartheta_S$  is the angle between the solar rays direction and the normal to the considered wall. The Earth's factor of view depends on the solid angle through which wall sees the Earth. It's algebraic expression is:

$$F_{EARTH} = \frac{1}{A_{WALL}} \int_{A_{WALL}} \frac{\cos\phi_1 \cos\phi_2}{\pi r^2} dA_{WALL} dA_{EARTH} \quad (2.8)$$

where  $A_{Wall}$  is the area of the wall radiator and  $A_{Earth}$  is the area of the Earth's section seen by the wall.

Two particular conditions have been evaluated: wall parallel to nadir direction and wall perpendicular to nadir direction. The Earth's factor of view has been calculated numerically for both cases, the obtained values are:

1) Wall parallel to nadir direction:  $F_{Earth} = 0,27$

2) Wall perpendicular to nadir direction:  $F_{Earth} = 0,86$

In the case of the power exchanged between the payload and the satellite the factor of view is  $F_{SATELLITE} = 0,27$ . Equation (2.1) has been solved numerically by a fourth order Runge–Kutta method.

Below the mean temperature are analyzed for the two attitude configuration.

#### 2.4.1 Nadir pointing configuration

During this time will be active the optical payload of the satellite and the experiment is switch off. Figure 2.7 show the prospective and lateral views of the orbital motion when the satellite is in nadir pointing attitude.

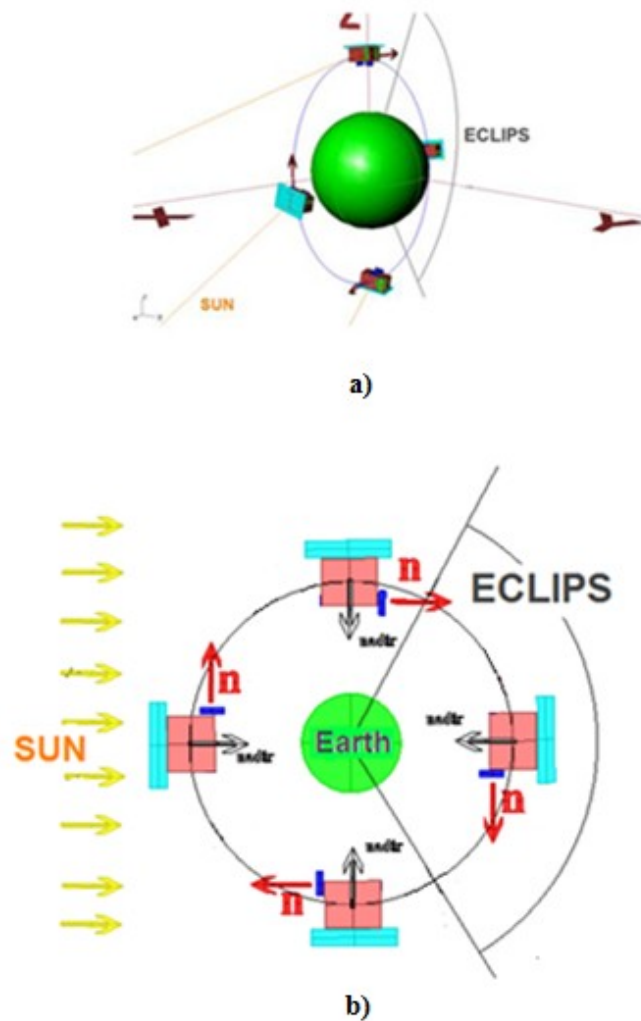


Figure 2.7 – Orbital scheme for the nadir pointing attitude. a) prospective view, b) lateral view.

In this case the radiator surface is constantly perpendicular to the earth during the orbit so the earth factor of view is 0,27. The sun factor of view depend on the orbital motion by the relationship:

$$\cos \vartheta_s = \left| \cos \frac{\pi}{8} \cos \omega t \right| \quad (2.9)$$

where  $\omega$  is the angular frequency of the orbital motion:

$$\omega = \frac{2\pi}{T} = 0.0011 \frac{rad}{sec} \quad (2.10)$$

The temperature changes of radiator are show in Figure 2.8.

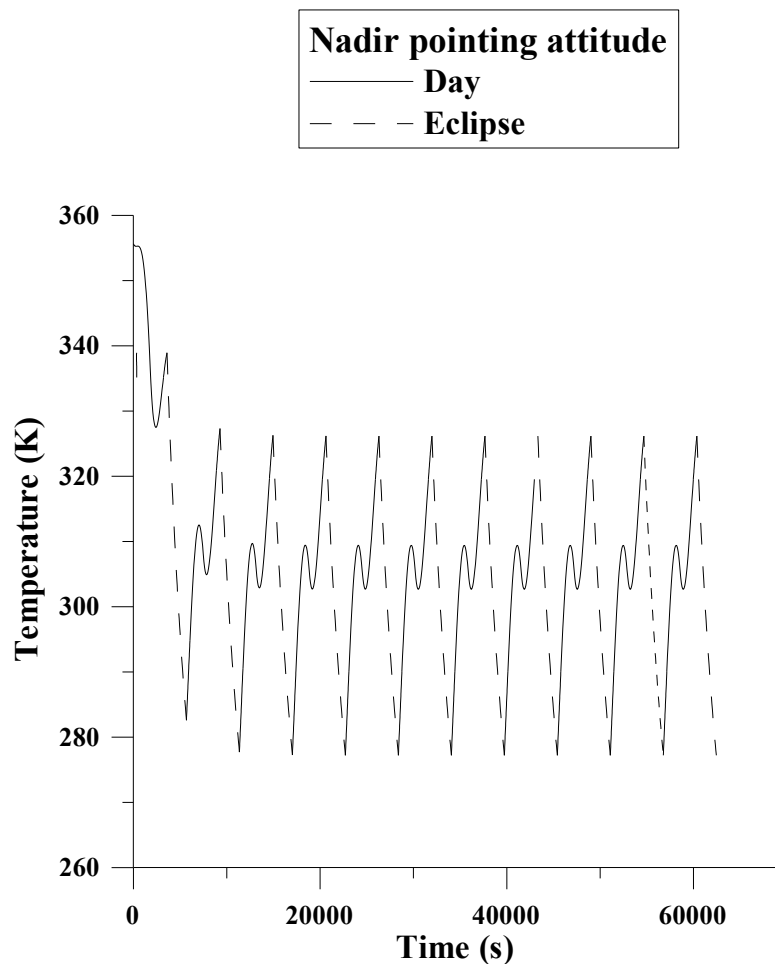


**Figure 2.8- Temperature of the heat pipe radiator during the nadir pointing attitude.**

The calculated mean temperature and fluctuations are:  $T = 303 \text{ }^\circ\text{K}$ ;  $\Delta T = \pm 24 \text{ }^\circ\text{K}$ . The large value of temperature fluctuations is due to the orbital motion. When the satellite exit from the eclipse period the heat pipe radiator is directly invested by solar radiation, so the temperature rapidly increase.

### 2.4.2 Sun pointing attitude

When the satellite has a sun pointing attitude the mean temperature decreases because solar panel obscures all the other satellite sub-systems, so the heat pipes don't absorb solar energy. Figure 2.9 shows the simplified orbital problem scheme.

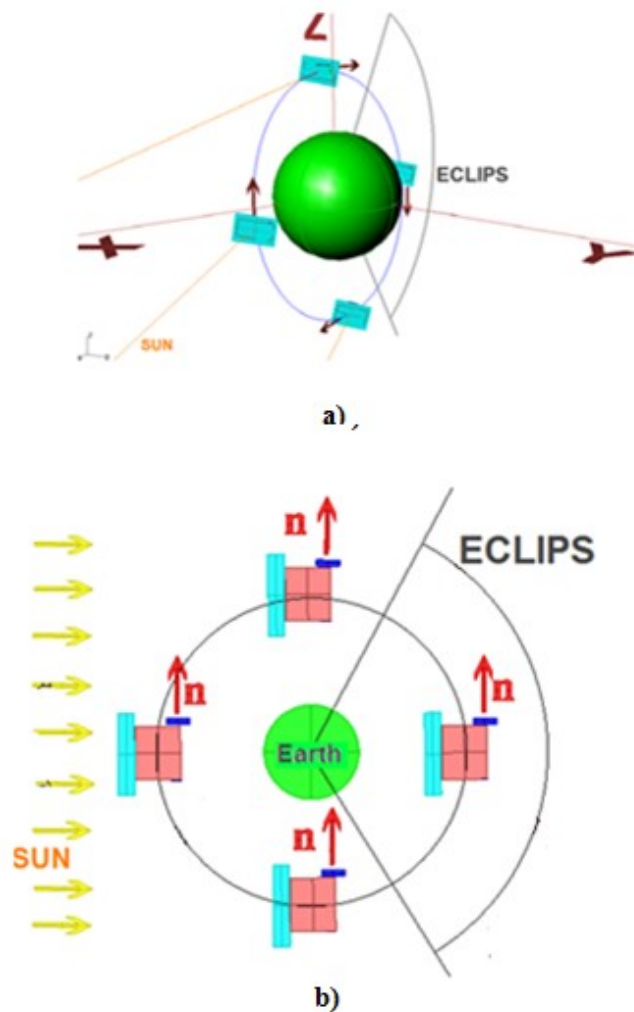


Figure 2.9 - Orbital scheme for the sun pointing attitude. a) prospective, b) lateral view.

Due to orbital motion the variation of earth factor of view is very complex. The earth factor of view is 0,86 when the radiator is perpendicular to nadir direction ( $\omega t = 0$  and  $\omega t = \pi$ ) and is  $0,27 * 2$  when the is parallel to the nadir direction ( $\omega t = \pi/2$ ).

To simplify the calculation the following interpolating law has been employed:

$$F_{EARTH} = 0.54 + 0.32|\cos\omega t| \quad (2.11)$$

Figure 2.10 show the variation of earth factor view during the orbital motion.

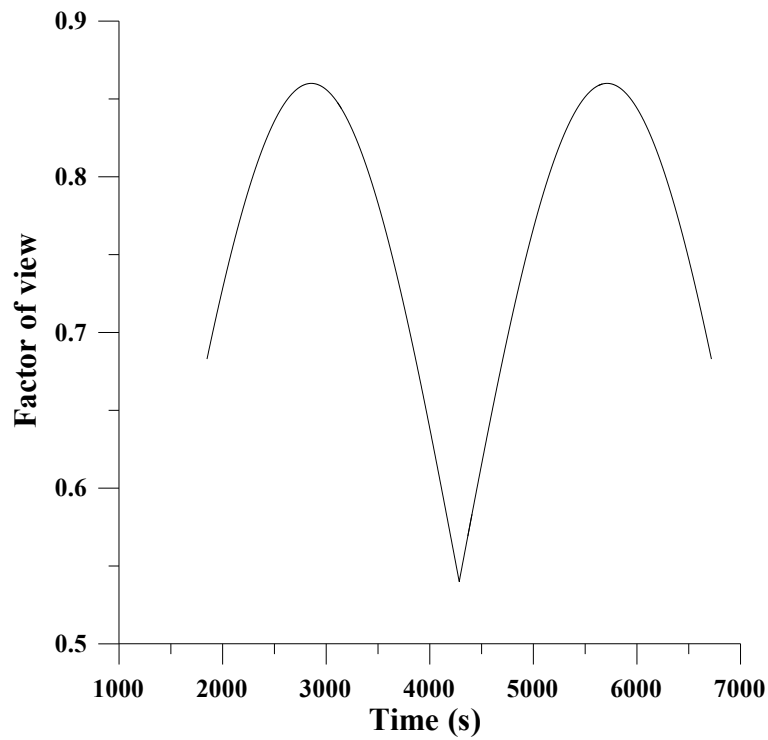
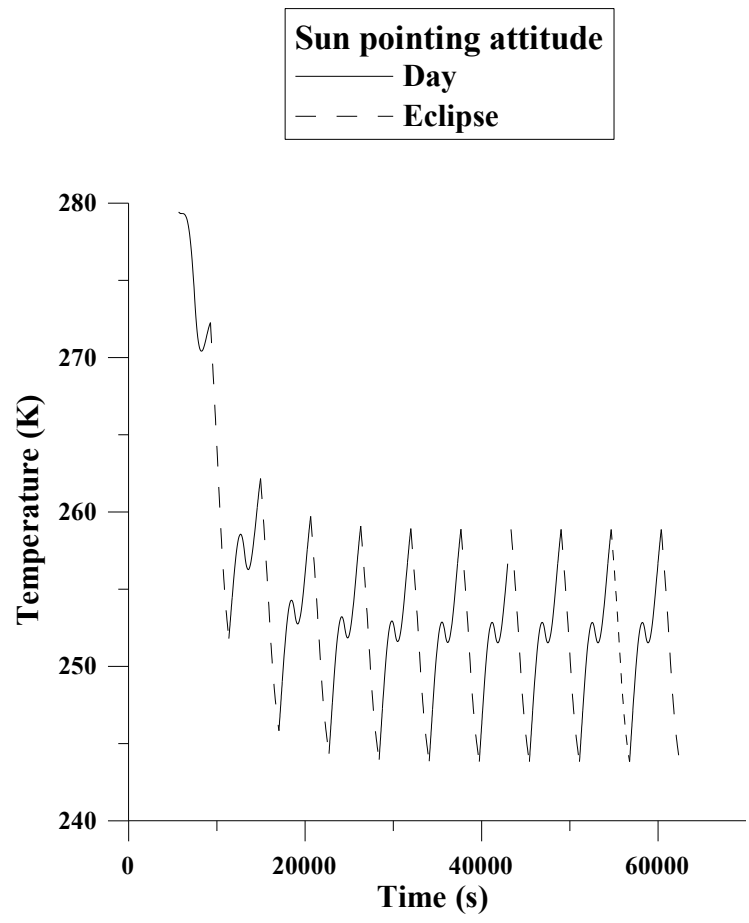


Figure 2.10 – Variation of earth factor of view during sun pointing attitude.

Figure 2.11 show the transient temperature of heat pipe radiator when the satellite is in the nadir pointing attitude.



**Figure 2.11 - Temperature of the heat pipe radiator during the sun pointing attitude.**

The calculated mean temperature and fluctuations are:  $T = 251 \text{ }^\circ\text{K}$ ;  $\Delta T = \pm 6$ .

## 2.5 Conclusion

The following table summarizes the results of thermal analysis:

**Table 2-3 Mean temperature and fluctuation for the two orbital configuration.**

<b>Attitude configuration</b>	<b>Mean Temperature</b>	<b>Fluctuation</b>
Nadir pointing attitude	303K	+24K
Sun pointing attitude	251K	+6K

If satellite has a nadir pointing attitude, the heat pipes have always a mean temperature major of  $0\text{ }^{\circ}\text{C}$ , so the working fluid is always liquid. Instead, if satellite has sun pointing attitude, heat pipes have a mean temperature less than  $0\text{ }^{\circ}\text{C}$ , so fluid is completely frozen.

Research activities pointed out to find new self-rewetting working fluids that above a self-rewetting behaviour has a lower freezing point (i.e. self-rewetting brines).

## 3 Surface tension measurements

### 3.1 Surface tension and wettability

Surface tension is a property of liquids arising from unbalanced molecular cohesive forces at or near the surface. Let us first consider a free surface, for example that between air and water (Figure 3.1). A water molecule in the fluid bulk is surrounded by attractive neighbours, while a molecule at the surface is attracted by a reduced number of neighbours and so in an energetically unfavourable state [47]. The creation of new surface is thus energetically costly, and a fluid system will act to minimize surface areas (it is thus that small fluid bodies tend to evolve into spheres)

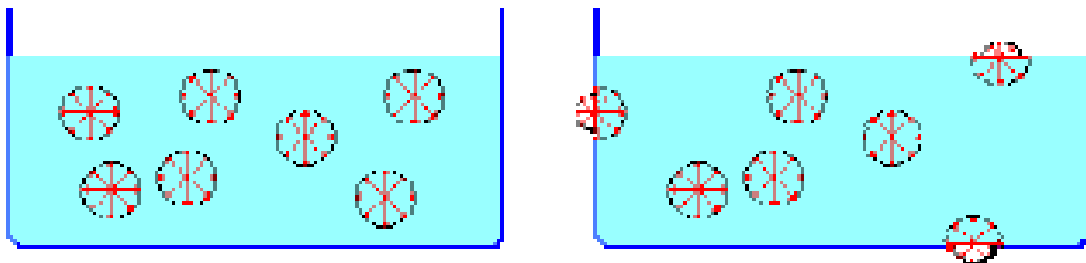


**Figure 3.1 – Molecular interaction at liquid-air interface**

Phenomenologically, surface tension, can be considered a force, directed tangentially to the surface, that act to contract the liquid surface. Surface tension, represented by symbol  $\sigma$ , has the dimension of force per unit length, or of energy per unit area. The two term are equivalent but normally when referring to energy per unit of area, the term is surface energy which is a more general term in the sense that it applies also to solids and not just liquids.

A number of different techniques have been developed to measure the surface tension. Two main categories can be considered: surface shape method (sessile drop and pendant drop), and capillary pressure method. Details on the different techniques are given in Ref. [15].

To completely understand the phenomena that govern capillarity is necessary to understand not only the interaction between the liquid and vapour regime but also the interactions occurring at the boundary between the solid and liquid regions and the solid and the vapour regions. When a liquid is in contact with a solid surface, molecules in the liquid adjacent to the solid will experience forces from the molecules of the solid in addition to the forces from other molecules in the liquid. Depending on whether these solid/liquid forces are attractive or repulsive, the liquid/solid surface will curve upwards or downwards, as indicated in Figure 3.2b). The two best known examples of attractive and repulsive forces, respectively, are water and mercury. Where the forces are attractive, the liquid is said to ‘wet’ the solid. The angle of contact made by the liquid surface with the solid is known as the contact angle,  $\theta$ . For wetting,  $\theta$  will lie between 0 and  $\pi/2$  rad and for nonwetting liquids,  $\theta > \pi/2$ .

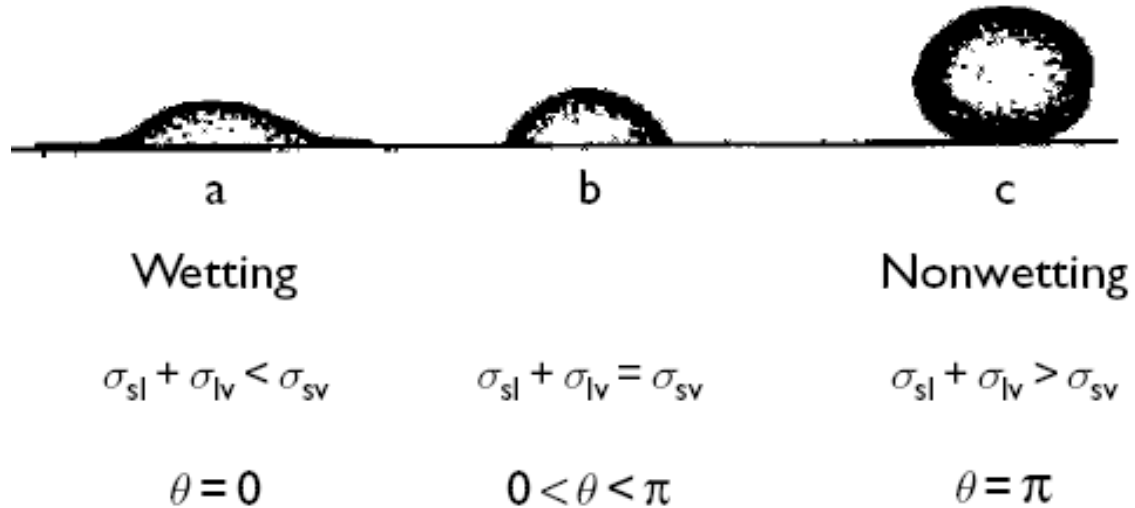


**Figure 3.2 - Wetting and non wetting contact.**

The condition for wetting to occur is that the total surface energy is reduced by wetting  $\sigma_{sl} + \sigma_{lv} < \sigma_{sv}$ , where the subscripts,  $s$ ,  $l$  and  $v$  refer to solid, liquid and vapour phases, respectively, as shown in Figure 3.2a).

Wetting will not occur if  $\sigma_{sl} + \sigma_{lv} > \sigma_{sv}$  as in Figure 3.2c), while the intermediate condition of partial wetting  $\sigma_{sl} + \sigma_{lv} = \sigma_{sv}$  is illustrated in Figure 3.2b).

As discussed in the first chapter both surface tension and wettability are important properties of working fluids because are responsible of capillary pressure necessary for the return of condensed liquid at evaporator side. In this chapter surface tension and contact angle measurements of different liquids, including water/alcohols solutions and innovative self-rewetting brines with relatively low freezing point, have been carried out. Objectives of researches are:

- characterization of water/alcohols solutions;
- identification and characterization of new self-rewetting fluids that above a self-rewetting behaviour exhibit a low freezing point suitable for low-temperature applications.

A comparison between the different working fluid has been carried out considering different thermo-physically properties of liquids.

### **3.2 Theory of pedant drop method**

The pendant drop method is one of the most convenient and versatile method to measure interfacial tension of fluids. The method is particularly suitable for high temperature systems and for systems where equilibrium is established after a long time.

The pendant drop method involves the determination of the profile of a drop of one liquid suspended in another liquid or fluid at mechanical equilibrium. The profile of a drop of liquid is determined by the balance between gravity and surface forces. Figure 3.3 show a typical pedant drop geometry.

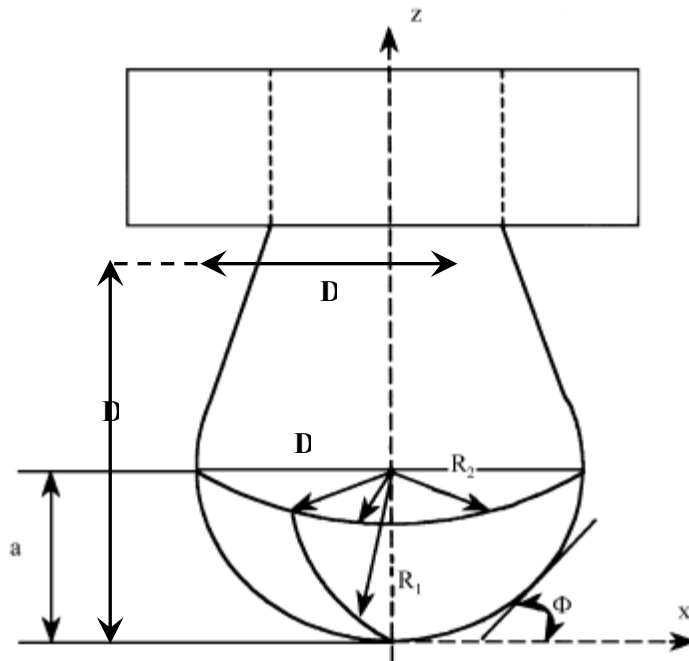


Figure 3.3 - The pendant drop geometry.

The shape drop is related to the Young-Laplace equation that describes the pressure difference across the liquid-vapour interface to the two main radii of curvatures:

$$\Delta p = \sigma \left( \frac{1}{R_1} + \frac{1}{R_2} \right) \quad (3.1)$$

where  $\sigma$  it is the surface tension,  $R_1$  and  $R_2$  the two main curvature radii and  $\Delta p = p_1 - p_2$  is the pressure difference across the interface.

In presence of the terrestrial gravitational field, the shape of a drop is deformed respect to the spherical shape because the hydrostatic pressure inside the liquid decreasing with heigh. The ratio of hydrostatic pressure is given by Stevino law:

$$p = p_0 - \rho g z \quad (3.2)$$

where  $z$  is the distance, in vertical direction, measured from the apex of the drop. (while the variations in the surrounding gas are negligible).

Using the Stevino law the Young-Laplace equation can be written as:

$$p_{01} - p_{02} + \Delta\rho g z = \sigma \left( \frac{1}{R_1} + \frac{1}{R_2} \right) \quad (3.3)$$

where:  $\Delta\rho = \rho_1 - \rho_2$  is the density difference between the two phases;  $p_{01}$  and  $p_{02}$  are the pressures at the two sides of the interface in a reference point.

If the reference point is the drop apex, and if we assume that in this point  $R_1 = R_2 = a$ , then:

$$p_{01} - p_{02} = \frac{2\sigma}{a} \quad (3.4)$$

and the Young-Laplace equation reads:

$$\Delta\rho g z + \frac{2\sigma}{a} = \sigma \left( \frac{1}{R_1} + \frac{1}{R_2} \right) \quad (3.5)$$

Using the coordinate system where  $x$  and  $z$  are respectively the horizontal and vertical coordinates measured from the bottom point of the drop the main curvature can be written in Cartesian coordinate as [48]:

$$z = z(x) \quad (3.6)$$

$$ds = \pm \sqrt{(dx)^2 + (dz)^2} \quad (3.7)$$

$$\phi = \arctan \left( \frac{dz}{dx} \right) \quad (3.8)$$

$$\frac{1}{R_1} = \frac{d\phi}{ds} = -\frac{d(\cos\phi)}{dz} = \frac{\frac{d^2z}{dx^2}}{\left( 1 + \left( \frac{dz}{dx} \right)^2 \right)^{\frac{3}{2}}} \quad (3.9)$$

$$\frac{1}{R_2} = \frac{\sin\phi}{x} = \frac{\frac{dz}{dx}}{x \left(1 + \left(\frac{dz}{dx}\right)^2\right)^{\frac{1}{2}}} \quad (3.10)$$

according to Bashforth and Addams [49] the Young-Laplace equation can be rewritten through an equivalent differential equations system:

$$\frac{dx}{ds} = \cos\phi \quad (3.11)$$

$$\frac{dz}{ds} = \sin\phi \quad (3.12)$$

$$\Delta\rho g z + \frac{2\sigma}{a} = \sigma \left\{ \frac{\frac{d^2z}{dx^2}}{\left(1 + \left(\frac{dz}{dx}\right)^2\right)^{\frac{3}{2}}} + \frac{\frac{dz}{dx}}{x \left(1 + \left(\frac{dz}{dx}\right)^2\right)^{\frac{1}{2}}} \right\} \quad (3.13)$$

with boundary condition

$$x(0) = z(0) = \phi(0) = 0 \quad (3.14)$$

$$\left(\frac{dx}{ds}\right)_{s=0} = 1; \left(\frac{dz}{ds}\right)_{s=0} = 1; \left(\frac{d\phi}{ds}\right)_{s=0} = 1; \quad (3.15)$$

where  $s$  it is the curvilinear abscissa along the surface of the drop,  $\phi$  is the angle between the tangent to the surface and the horizontal and  $a$  is the radius of curvature at the bottom of the drop.

If we consider (3.9) and (3.10), equation (3.13) it can be expressed as:

$$\frac{d\phi}{ds} = \frac{2}{a} + \frac{\Delta\rho g z}{\sigma} - \frac{\sin\phi}{x} \quad (3.16)$$

therefore, if all lengths of the equation are dimensionless with respect to  $a$ , the equation becomes:

$$\frac{d\phi}{ds^*} = 2 + \beta z^* - \frac{\sin\phi}{x^*} \quad (3.17)$$

where the only parameter  $\beta$ , is defined as:

$$\beta = \frac{\Delta\rho g a^2}{\sigma} \quad (3.18)$$

$\beta$  is the Bond number, measuring the ratio between the gravitational forces and the surface tension forces and is responsible of the shape of the drop. When the Bond number is close to zero, surface tension effects prevail and the drop becomes almost spherical, while for relatively high Bond number, the drop assumes the typical shape lengthened by the gravity effect.

For the evaluation of the surface tension the theoretical shape of drop must be compared with the experimental shape: from this comparison it's possible to evaluate the values of  $\beta$  and  $a$ . At this point the surface tension is computed as:

$$\sigma = \frac{\Delta\rho g a^2}{\beta} \quad (3.19)$$

In 1882, Bashforth and Adams derived the theoretical form of a pendant drop and calculated tables of drop contours. The tables can be used to determine the surface tension by fitting the experimentally measured drop contour to the theoretical curve. Photographs of the evolving drop could be taken as a function of time for comparison.

To simplify this procedure, the following empirical relationship was proposed by Andreas [50]:

$$\sigma = \frac{g D_e^2 \Delta\rho}{H} \quad (3.20)$$

Where  $D_e$  is the equatorial diameter of drop and  $H$  is a correction factor which is related to the shape factor of the pendant drop,  $S$ , defined as:

$$S = \frac{D_S}{D_e} \quad (3.21)$$

where  $D_S$  is the drop diameter measured horizontally at a distance  $D_e$  away from apex of the drop. Unfortunately, the above methods use only few measurements to define the entire shape of the drop, leading to imprecision in the comparison between the experimental profile and the numerical solution of the Bashforth and Adams equation.

Recent progress in image analysis and data acquisition systems has made it possible to obtain a direct digitization of the drop image with the aid of a video frame grabber of digital camera [51]. The digital signals are analyzed using different algorithms to determine the interfacial tension from the drop profile.

The pendant drop apparatus and the image processing used in this work are described below.

### 3.3 Experimental setup

The experimental setup is based on the Dataphysics OCA 15+ tensiometer [52] and include the following subsystems (see Figure 3.4):

- 1) Experimental cell;
- 2) Tensiometer;
- 3) Thermal control system;
- 4) Temperature acquisition system;
- 5) Personal computer for visualization, acquisition and direct control of experiment;

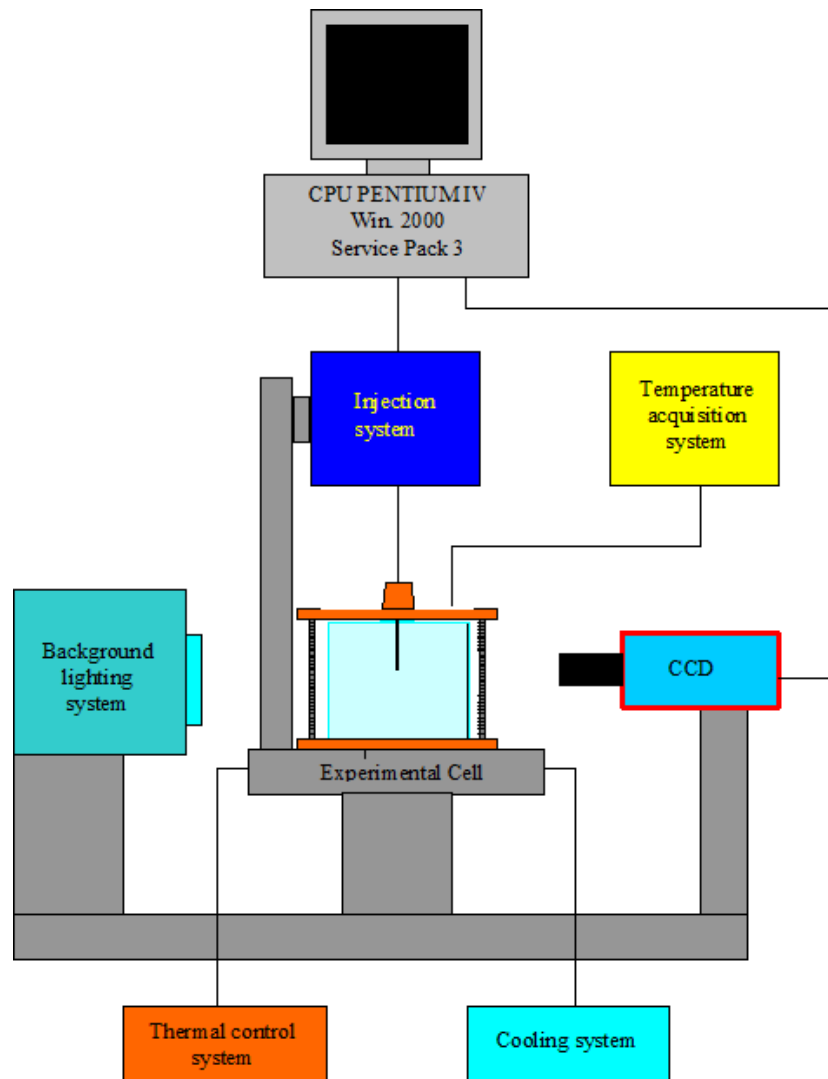


**Figure 3.4 - Experimental configuration with all subsystems**

The experimental cell (inner dimension: 9.5mm\*9.5mm\*43.5mm) is composed by an optical glass cell with good optical properties (refractive and dispersion index are very low, which guarantee a transmission in visible spectrum approximately of 80%), used as container of liquid and an external structure formed by two copper plates, one below and one above the glass cell. The plate above is pierced for putting in the needle and the thermocouple.

The tensiometer, provided by Data Physics, include: an electronic injection system, a background illumination system, a CCD-camera (zoom: 6x; matrix: 752 x 582 “square pixels”; field of view: from 1.31mm x 1.05 mm up to 8.77mm x 6.75 mm), and a thermal regulated plate (see Figure 3.5).

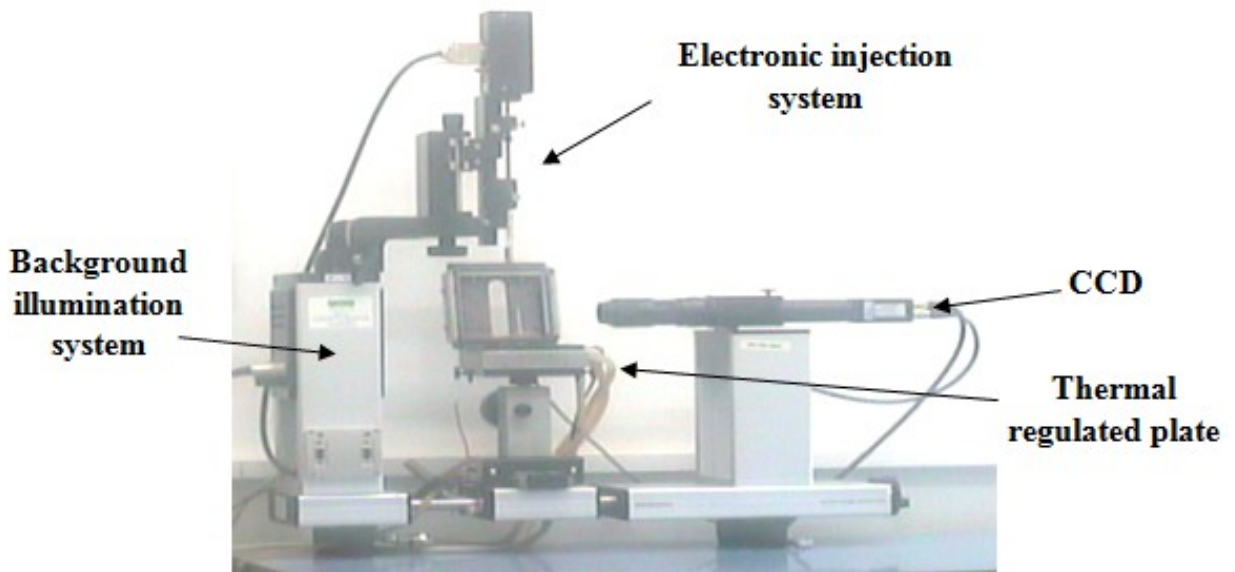


**Figure 3.5 - Tensiometer OCA15+**

The thermal-regulated plate where the experimental cell is located is free to translate in all three directions for correct alignment between the cell, the digital video camera and the light background. Thermal control is employed by a system control which uses a peltier element to heat the cell. A peltier's side is in contact with the base of the experimental cell while the other side is cooled by circulating water.

Typically, using an electronic injection system a pendant drop is formed, the drop image is acquired by the CCD camera and the contour is analyzed to infer the surface tension using suitable software. High-quality images of the drop are obtained using a background illumination system that allows the possibility to regulate the contrast.

The images are digitized by a frame grabber resident in the computer and are analyzed online measuring the interfacial tension in real time during the experiment. Figure 3.6 shows a typical image acquired by the software.

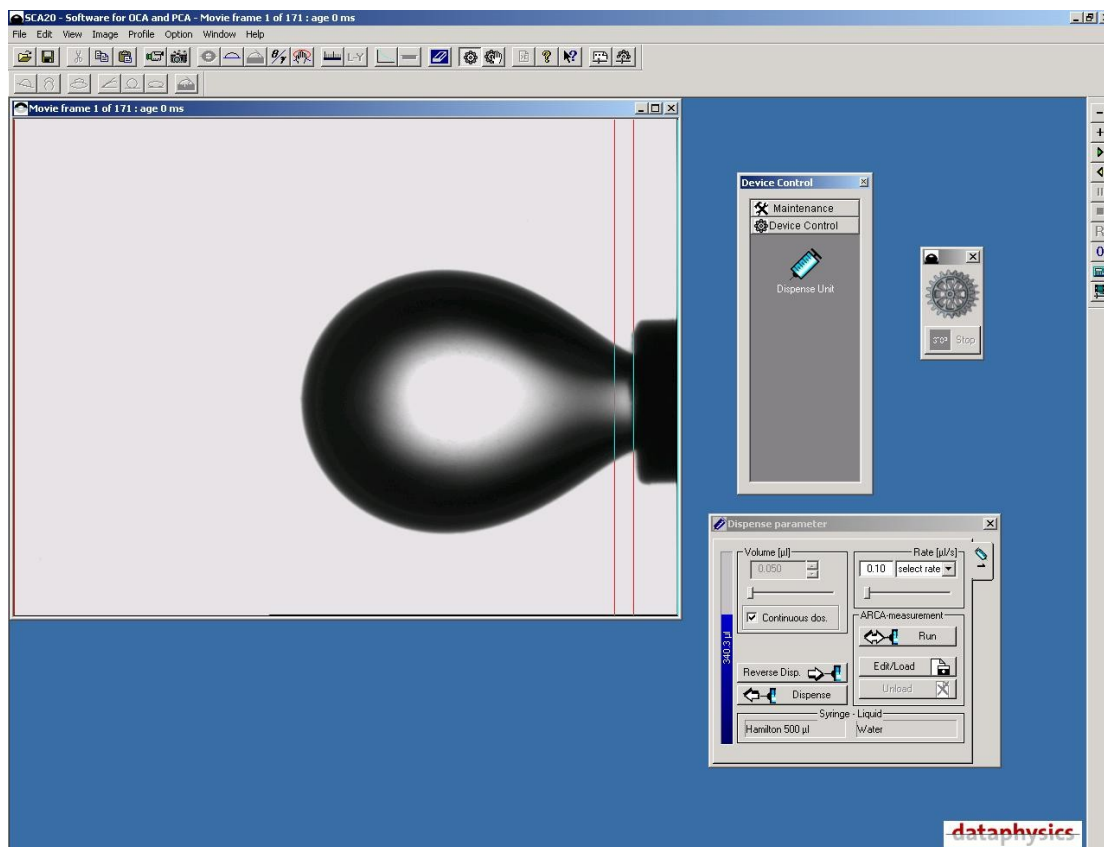


**Figure 3.6 - Graphic interface of SCA20 software control**

The whole process of analysis of the drop shape consists of four main steps:

1) the image of the pendant drop is captured and digitalized using a computer with a frame grabber;

2) the drop contour is extracted to evaluate the radius of curvature at the apex necessary for the calculation of the surface tension. The contour of the drop is defined by the last pixel with a gray level higher than the threshold value. In order to evaluate the interfacial tension using Eq. (3.19) it is necessary to know the radius of curvature at the apex of the drop. In many works, the value of the radius of curvature at the apex of the drop is taken as the distance between the apex and the center of the diameter as shown in Figure 3.7 a). In the case of longer drops as shown in Figure 3.7 b) the values of the radius at the apex are overestimated, consequently overestimating the values of interfacial tension.

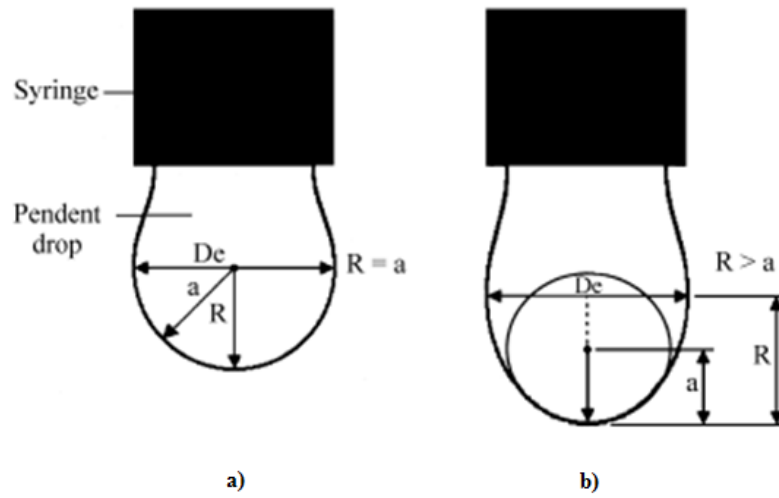


**Figure 3.7 - Evaluation of the radius of curvature at the apex of drop**

Once the edge detection has been performed, the symmetry axis of the drop is determined. The intersection between the drop profile and the symmetry axis is also determined. Circles of different radii are superposed to the maximum number of points around the apex. The radius of the circle that superposes to the maximum number of points is taken equal as the radius of curvature of the drop at the apex.

3) smoothing of the extracted contour is carried out using polynomial regression; Details on the algorithm used are given in ref.

4) the experimental drop shape is compared with theoretical results obtained solving the Bashforth and Adams equation [49] by a fourth order Runge–Kutta method. The Bashforth and Adams equation is first solved for a value of  $\beta$  approximated by the empirical formula [54]:

$$\beta = \sqrt{\exp\left(-6.70905 + 15.30025S - 16.44709S^2 + 9.92425S^3 - 2.585035S^4\right)} \quad (3.22)$$

where  $S$  is the ratio  $De/Ds$ ,  $De$  is the equatorial diameter of the drop,  $Ds$  is the diameter measured horizontally at a distance  $De$  from the apex of the drop.

Replacing in the 3.15 the  $\beta$  and  $a$  values it's possible to evaluate the surface tension.

### 3.4 Surface tension measurements

Surface tensions of several fluids, pure liquids and binary mixtures have been evaluated at different temperatures using the apparatus and technique described in the previous paragraphs. In particular, solutions with a small concentration of butanol, pentanol, exanol, heptanol or octanol in water have been investigated. The measurements have been performed in the temperature range 20–80°C.

In addition, innovative brines (FD-40, FP-40), with or without the addition of small concentrations of butanol or heptanol have been investigated for their interesting properties. The first one is a water solution of potassium hydroxide (24%), acetic acid (24%) and other components (6%), the second brine is a water solution of potassium formate (50%w) and inhibitors (1%w). Both brines are ecological liquids with freezing point at -40°C; in addition they are compatible to ordinary metallic materials, such as copper, aluminium et al..

The experimental cell is partially filled with the same liquid, in order to overcome problems related to possible liquid evaporation at relatively high temperatures. The bottom wall of the cuvette is heated by thermal control system so that the temperature of the surface is constant and controlled with an accuracy of 0.1°C in the range 20°C - 100°C during the experiments.

A thin thermocouples was used to measure the temperature close to the pendant drop surface. Once achieved the selected temperature as recorded by the thermocouple, the drop was formed and the surface tension was measured on the basis of the shape detected with a parallel light background illumination and a digital video camera. Each experiment was repeated several times. Nearly 10 acquisitions have been done for each selected temperature and the final value of the surface tension was taken as the average value of all the experimental data; for each temperature, the maximum deviation was equal to almost  $\pm 0.5\text{mN/m}$ . The results of the measurements for both pure liquids and alcohols binary mixtures are shown in Figure 3.8 and Figure 3.9.

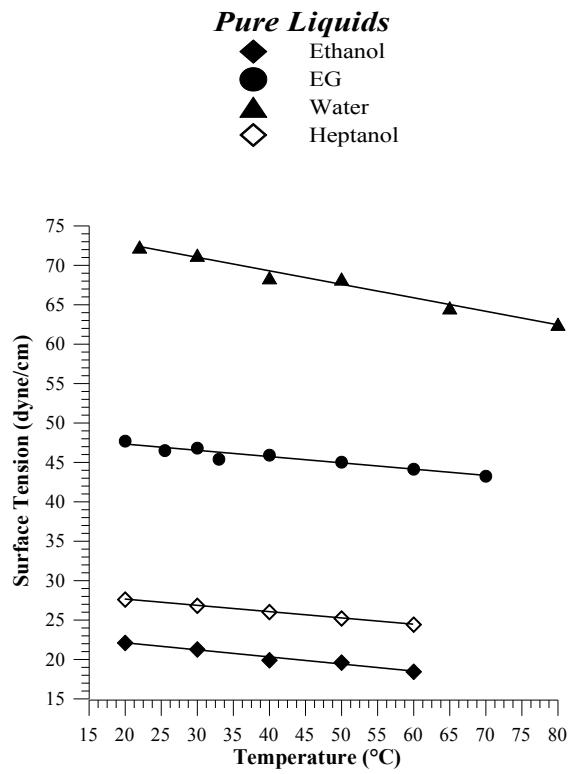


Figure 3.8 - Surface tension measurements of pure liquids.

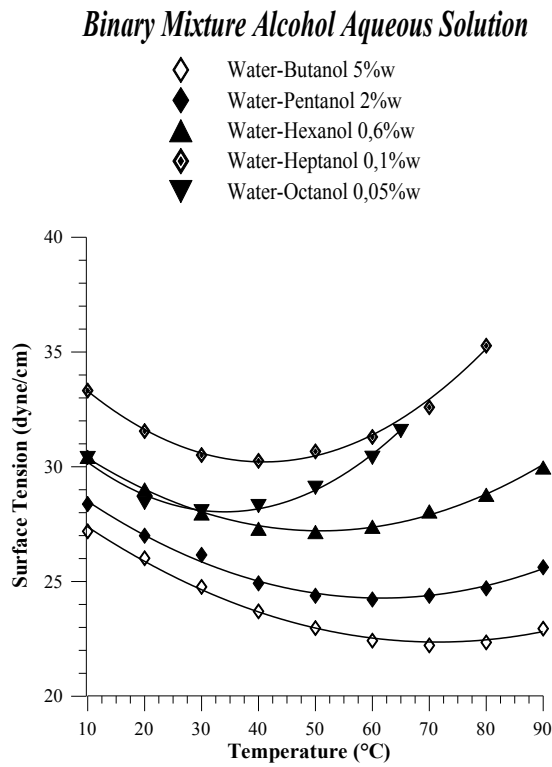


Figure 3.9 - Surface tension measurements of binary mixtures

As well known in literature, for all pure liquids analyzed (Ethanol, Water, EG, Heptanol) the surface tension is an almost linear, decreasing function of the temperature (Figure 3.8).

For aqueous binary mixtures containing long chain alcohols (Figure 3.9), the surface tension exhibits a non-linear dependence with temperature with a minimum above which the surface tension increases with temperature. For some solutions the experiments were repeated many times and the results were systematically confirmed.

Figure 3.10 show the results of water/alcohols solutions normalized with respect to the values of the surface tension at 20°C.

***Binary Mixture Normalized Alcohol Aqueous Solution***

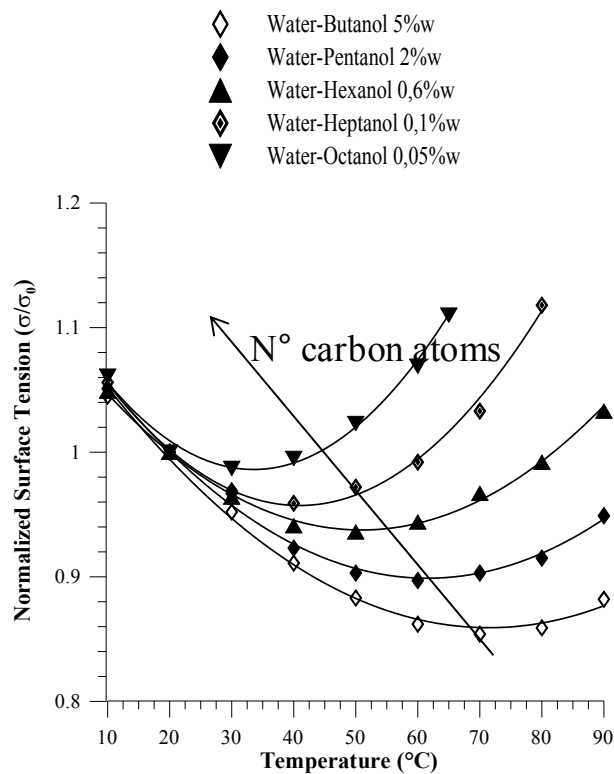


**Figure 3.10 - Normalized surface tension measurements of binary mixtures**

Typically, the temperature corresponding to the minimum of the surface tension is an increasing function of the number of Carbon atoms.

Figure 3.11 show results of surface tension measurements for FP40 and FD40 solutions.

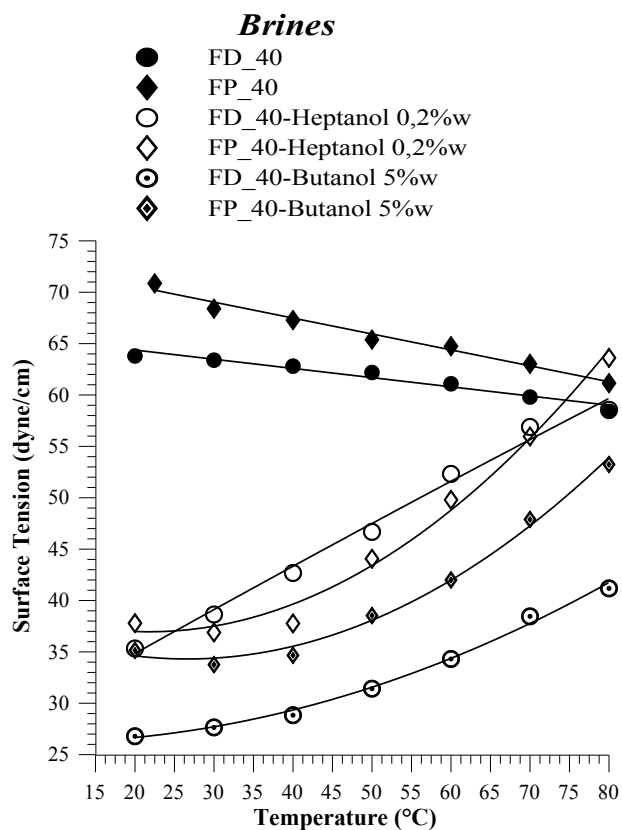


**Figure 3.11 - Surface tension measurements of self rewetting brines.**

Both FP-40 and FD-40 brines exhibit ordinary surface tension dependence with temperature (very similar to water); with the addition of heptanol or butanol alcohols (0,2%w and 5%w respectively) both FP-40 and FD40 brines gives rise to “self-rewetting brines”, i.e. low-freezing point fluids with the same positive surface tension behaviour of water/alcohols mixtures. In addition, for the self-rewetting brine based on FD40 and butanol, the temperature of the minimum of surface tension is shifted from 70°C to 20°C with respect to the water/butanol mixture at the same concentration. Considering FP-40 based brines, the temperature of the minimum of surface tension is reduced to 20°C. Furthermore, the value of the surface tension derivative for the self-rewetting brines is higher. This should produce a relatively stronger reverse Marangoni effect at liquid-vapor interface.

### 3.5 Contact Angle Measurements

Contact angles have been measured for the different liquids at room temperature with the same apparatus used for the surface tension measurements, using the sessile drop method. An advantage of this technique is that the needle does not remain inside the drop during the measurement, the drop is produced before the measurement and has a constant volume during the experiment. This prevents the drop from being distorted (particularly important for small drops). Contact angle is evaluated from the image of the drop obtained with a CCD camera with a optical zoom 6x (Figure 3.12).

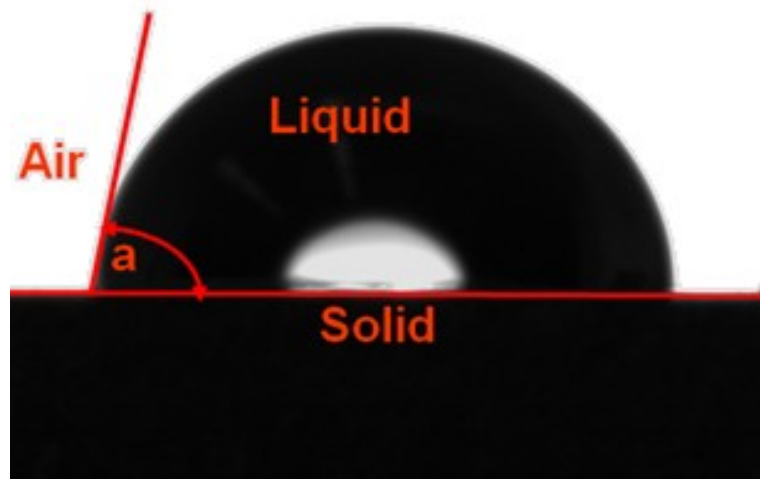


**Figure 3.12 - Sessile drop method for contact angle measurements**

The drop shape and the contact line (baseline) with the solid, are first evaluated by the software analyzing the grey level values of the image pixels. Then, the found drop shape is adapted using a mathematical fitting model based on Young-Laplace equation. Therefore, the contact angle is determined as the slope of the contour line of the drop at the 3-phase contact point (air, liquid, solid).

In order to have a good reproducibility of the measurements a standard procedure for the experiments has been defined: the volume of the injected drop is always of  $2 \mu l$  and the measurements are carried out five seconds after the drop injection in order to reduce evaporation effects.

Each experiment was repeated several times. Nearly 15 acquisitions have been done for each measure and the final value of the contact angle was taken as the average value of all the experimental data, the maximum deviation was equal to almost  $\pm 1^\circ$ .

Table 3-1 summarize the results of the measurements for the selected materials and liquid solutions.

**Table 3-1 Contact angle measurements.**

<b>Fluids</b>	<b>Contact angle on copper (°)</b>	<b>Contact angle on alluminium (°)</b>
Water	80,2	85,6
Ethanol	9	7
FP40	62,9	52,6
FD40	75	72
Water-Heptanol 0,2% wt	58.5°	56.4°
Water – Butanol 5% wt	53.5°	50.9°
FP40 - Heptanol 0,2% wt	66.8°	64.0°
FP40 – Butanol 5% wt	58.5°	56.4°
FD40-Heptanol 0,2% wt	75	72
FD40 – Butanol 5% wt	73	69

The measurements show that, in general, the addition of a small amount of alcohol, in particular butanol and heptanol, improves the metal wettability.

### 3.6 Syntesis

As discussed in the first chapter, self-rewetting fluid exhibit interesting surface tension properties that, in combination with wetting properties and a relatively low freezing point, could be properly exploited for heat transfer applications. Selection of the working fluid for heat transfer applications depends on a number of considerations regarding:

- 1) the operating temperature range;
- 2) the compatibility with the materials;
- 3) the fluid thermophysical properties.

Fundamental requirements for the liquid are: good thermal stability, good wettability of the liquid with wick and wall materials, high latent heat, high thermal conductivity, low liquid and vapor viscosities, high surface tension and acceptable freezing point.

Table 3-2 summarizes different thermophysical properties and some of their combinations for the several liquids considered in the present study [55]. The most relevant thermo-physical properties, such thermal conductivity and heat of vaporization have been founded in literature [56]. Each of these parameters is of particular relevance and represents a figure of merit for the fluid, when selected as heat transfer fluid in heat pipes. Some properties like surface tension and thermal conductivity have been evaluated at different temperatures (i.e. 20°C and 80°C).

**Table 3-2 Thermophysical properties of self-rewetting fluids.**

Fluids	Temperature range (°C)	Contact angle on copper (°)	Thermal conductivity (W/mK)	Heat of vaporization at 1atm (MJ/Kg)	Capillary driving force (m/s)	Thermo-capillary driving force (m/sK)
Water	0/100	81	0.603*	2.448*	11.23*	-0.173*
			0.668**	2.309**	27.28**	-0.490**
FP-40	-55/122	88	0.478*	1.224*	1.45*	-0.095*
			0.525**	1.154**	3.129**	-0.238**
Butanol	-89/118	45	0.155*	0.716*	6.10*	-0.031*
			0.143**	0.640**	32.58**	-0.196**
Heptanol	-35/176	45	0.161*	0.584*	2.77*	-0.011*
			0.147**	0.522**	20.35**	-0.100**
Water-butanol	-1.3/100.4	53	0.581*	2.361*	16.88*	-0.176*
			0.642**	2.225**	40.41**	+0.179**
FP40-butanol	-56/122	67	0.462*	1.199*	7.57*	+0.033*
			0.506**	1.128**	28.54**	+0.622**
Water-heptanol	-0.03/100.01	52	0.602*	2.444*	17.01*	-0.026*
			0.667**	2.305**	55.16**	+0.663**
FP40-butanol	-55.03/122.01	62.26	0.477*	1.223*	9.93*	+0.118*
			0.524**	1.153**	38.01**	+0.908**

The temperature working range is defined by the freezing and boiling points. The freezing and boiling temperatures (the latter corresponding to 1 atmosphere pressure) are reported for the different liquids in Table 3-2. It is evident that pure water or relatively dilute water

solutions cannot be used in space applications at temperatures below 0°C. Other pure liquids (e.g. Butanol or Heptanol) exhibit a relatively low freezing point, but rather poor heat transfer properties, like thermal conductivity and latent heat of vaporization, when compared to water. Another important property is the contact angle that, in combination with the surface tension, provides the relative capillary/viscous driving force responsible for the return, to the evaporator, of the condensate liquid in the wick structure ( $\frac{\sigma \cos \theta}{\mu}$ ). In the present case the contact angles are evaluated with reference to a copper surface.

Finally, in order to consider Marangoni effect, the thermo-capillary driving force, defined as  $\sigma_T \mu$ , has been evaluated. This parameter can be positive or negative depending on the sign of Marangoni convection (negative in the ordinary case of liquid flow directed from the hot side to the cold one).

In order to compare the different working fluids at each liquid a score for each parameter has been assigned, from 1 to 8, 8 being best rank. The final scores are summed over all of the parameters and the liquid with the highest total score is the “preferred” working fluid (Table 3-3).

**Table 3-3 Comparison of the different working fluid**

Fluids	Thermal conductivity	Heat of vaporization	Capillary driving force	Thermo-capillary driving force	Final score
Water	8	8	3	1	20
FP-40	5	5	1	2	13
Butanol	1	2	5	3	11
Heptanol	2	1	2	4	9
Water-Butanol	6	6	7	5	24
FP-40 Butanol	3	3	4	7	17
Water-Heptanol	7	7	8	6	28
FP-40 Heptanol	4	4	6	8	22

Generally, all the self-wetting fluid have a final score higher in comparison to the base liquid. In particular, based on the parameters considered in this work, the best working fluid is the water/heptanol solution, but the freezing point in this case is very close to that of water.

Self-rewetting brines exhibit also a relatively high score and should be taken into account as heat transfer fluids for space applications.

## **4 On ground activity in view of the MIOsat mission**

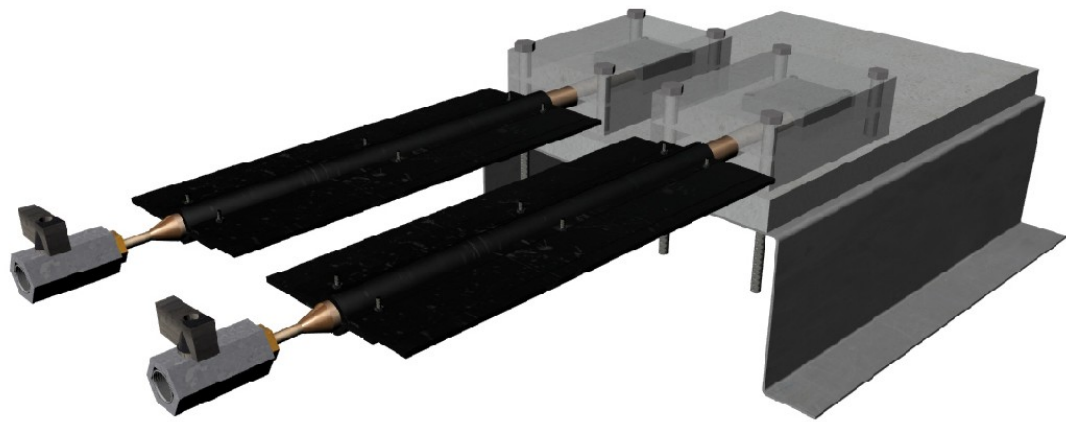
### **4.1 Introduction**

In view of the heat pipe MIOsat experiment a number of on-ground activities have been carried out to show the behaviour of the self rewetting fluid in heat transfer process of heat pipe. For this scope, a breadboard similar to the flight payload and a filling facility has been developed at laboratory of DIAS to analyze the thermal performances of wickless and wicked heat pipe. In particular, a wicked heat pipe has been characterized both numerically and experimentally and the effect of filling ratio on the thermal performances has been studied.

Preliminary flow visualization of heat pipe filled with different self rewetting fluids has been carried out using glass capillary. A comparison between ordinary, self rewetting fluid and self-rewetting brine has been carried out.

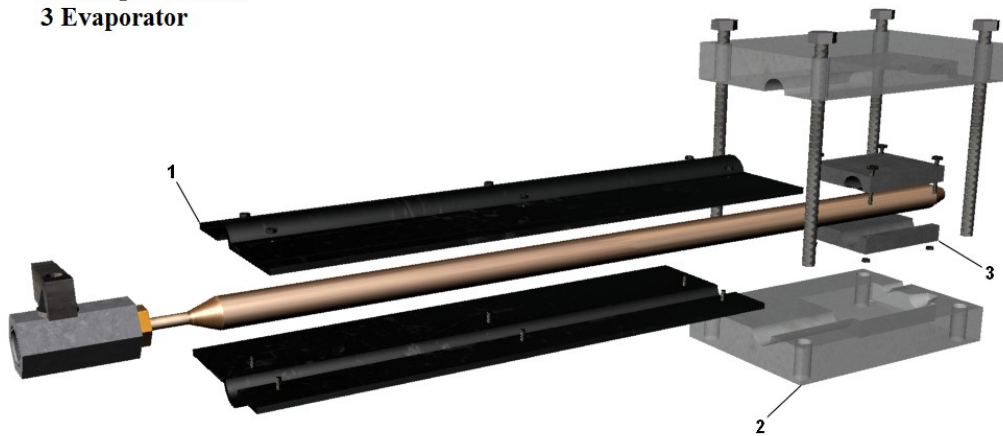
### **4.2 Breadboard for the thermal characterization of heat pipe**

In preparation of the MIOsat heat pipe experiment, a dedicated laboratory test bench for thermal characterization of heat pipe has been developed. The apparatus is similar to the space payload design described in the second chapter. Figure 4.1a) show the laboratory test bench [57].



a)

1 Condenser  
2 Plexiglass Block  
3 Evaporator



b)

Figure 4.1 - Laboratory breadboard for thermal test of heat pipe. a) prospective view, b) extrude view.

The test bench is able to accommodate two heat pipes with a diameter of  $8\text{ mm}$  and a length of  $250\text{ mm}$ . According to the space payload design the radiator has been realized using an aluminum plate. Heat exchange during laboratory test is due both to the natural convection and thermal radiation. The size of the radiator is the same as in the flight payload; in this case,

contrary to the space design, the plate has been black painted because there is no need to reduce the surface absorbance (the white painting foreseen in the space payload will guarantee a relative high emissivity in the infrared spectrum and a relatively low absorbance in visible range).

At the evaporator side the pipes are placed between aluminum blocks (length of 30 mm) held together by screws (see Figure 4.1b)). Cartridge heaters with length 28 mm and diameter 6.25 mm (provided by Watlow) are introduced inside holes and are heated by a power supply. In order to minimize the heat loss a Plexiglas block has been added to the evaporator and adiabatic section of the heat pipe.

Four thermocouple (K-type) for every heat pipe has been used to measure the wall temperature of heat pipes. The thermocouple T1 is located in the center of the evaporator block and measures the interface temperature between the block and the heat pipe. The thermocouple T2 is located close to the evaporator at the beginning of the adiabatic region. The thermocouples T3 and T4 are placed, respectively at the beginning and in the mid of the condenser.

The temperature signals are monitored and stored by a multiple channels data logger connected by Ethernet to a work station (Figure 4.2).



**Figure 4.2 – Data acquisition system.**

The data logger (Keithley Integra 2701) allows the possibility to store the temperature signals, as well as of the electrical current and voltage provided by the power supply to the cartridge heaters.

### 4.3 Filling procedure

Figure 4.3 shows a sketch of the facility used to fill heat pipes. Each pipe was connected to a vacuum valve from one side. Preliminary test have been carried out with a manometer on the other side. The vacuum valve was linked to the circuit connected to the pump. The valve was welded on the pipe. Several hours after the pipe was evacuated the pressure was still well below 400 microbar indicating the welding on the valve was successfully.

A precise amount of working fluid was been introduced into the pipe using a syringe and the pipe closed with the valve V2. The pipe was first set up in vertical configuration and heated at the evaporator section to boiling the working fluid in order to degassing.

To prevent mass loss and change of composition of the solution, during the evacuation process the working fluid was frozen using a cooling system. For instance for a water solution a HAAKE DC50-K50 Refrigerated Circulator with alcohol ethylic as cooling liquid has been used. Temperature of thermal bath is set to  $-40^{\circ}\text{C}$ .

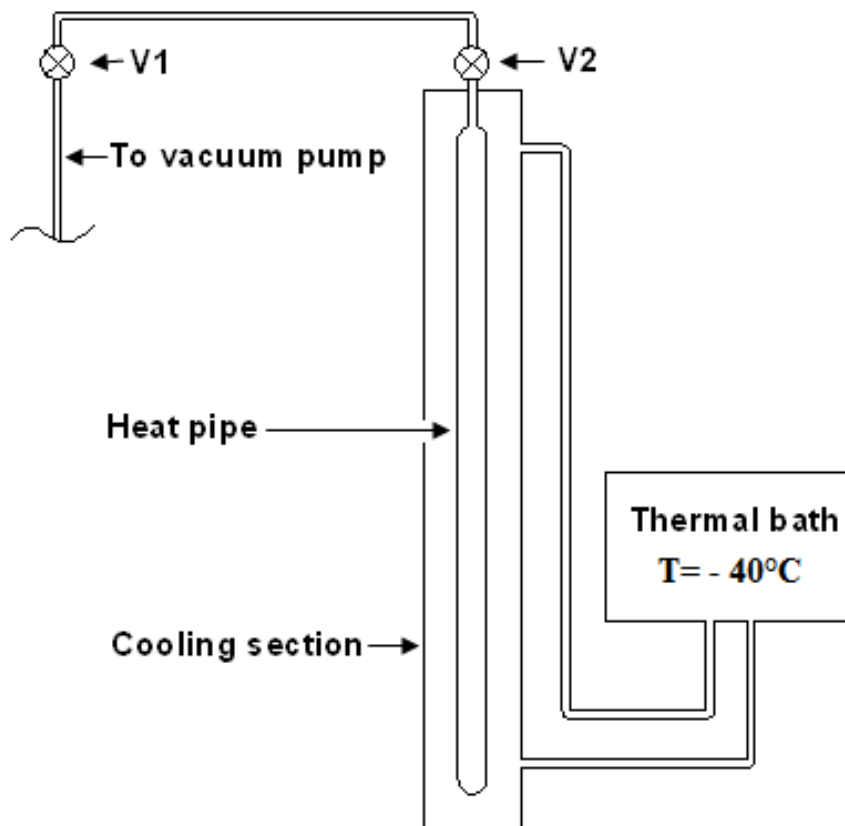


**Figure 4.3 - Sketch of the filling facility used to fill heat pipes**

When the fluid was frozen the pipe was evacuated opening the valve V1 and V2. Typically, a vacuum level down to 400 microbar is employed. Heat pipe was weighted first and after the filling process to control the working fluid inventory.

The pipe was then pinched on the valve side using a dedicated tool, cut and welded. Several preliminary test with the manometer connected to the pipe demonstrated that the pressure level reaming well below 400 microbar after several days, showing that the pinching and relative process was successfully.

#### 4.4 Numerical simulation of groove heat pipe

In this section a commercial heat pipe for terrestrial applications has been characterized. The pipe is a copper pipe with a axial groove structure provided by Fujikura Ltd. Figure 4.4 show the geometry of heat pipe considered.

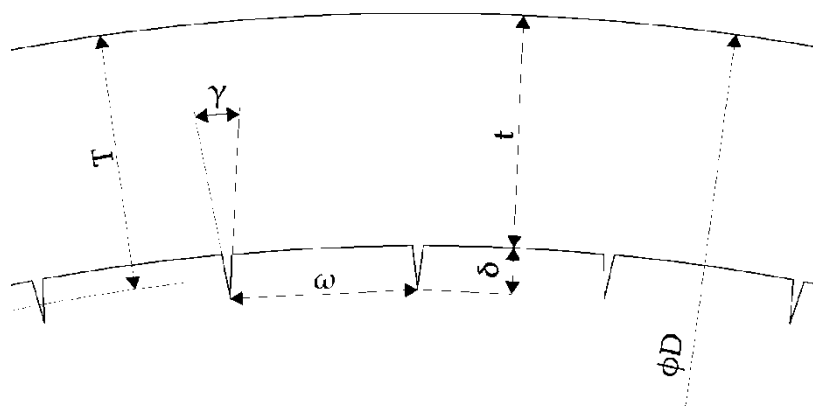


Figure 4.4 - Groove geometry

The groove have a trapezoidal cross section, the main parameter of wick structure are listed in Table 4-1.

**Table 4-1 Groove dimension.**

Outside Diameter	D(mm)	8
Average wall thickness	T(mm)	0,44
Bottom wall thickness	t (mm)	0,4
Groove Depth	h (mm)	0,075
Lead angle	x (°)	0
Number of Grooves	n(-)	75
Apex angle	γ (°)	5

The wicked heat pipe has been modeled both analytically and numerically using model proposed in literature.

#### 4.4.1 Analytic model

An analytical model has been employed to investigate the performance of heat pipe using water as working fluid. The model has been used to determine the limits of heat transport capacity, which expresses the thermal performance of heat pipes. The model is defined in terms of the physical shape of the heat pipes and evaluates the limits of heat transport capacity as functions of the properties of the working fluid used and the inclination angle  $\psi$ .

The capillarity limit has been evaluated according to the relationship:

$$(\Delta p_c)_m = \Delta p_v + \Delta p_l + \Delta p_{\perp} + \Delta p_{\parallel} \quad (4.1)$$

where  $(\Delta p_c)_m$  is the maximum capillary pressure difference generated within capillary wicking structure,  $\Delta p_v$  and  $\Delta p_l$  are the sum of inertial and viscous pressure drops occurring in vapor and liquid phase respectively and  $\Delta p_{\perp} = \rho_l g d_v \cos \psi$  and  $\Delta p_{\parallel} = \rho_l g L \sin \psi$  are the normal and axial hydrostatic pressure drop ( $\rho_l$  is density of liquid,  $d_v$  and  $L$  the length of heat pipe).

For a groove geometry the maximum capillary pressure difference is given by the Young-Laplace equation:

$$(\Delta p_c)_m = \frac{2\sigma}{\omega} \quad (4.2)$$

where  $\omega$  is the groove width (see Figure 4.4). The inertial and viscous pressure drops occurring in vapor and liquid phase has been evaluated through a model proposed in Ref [58]:

$$\Delta p_v = \left( \frac{C(f_v Re_v)\mu_v}{2(r_{h,v})^2 A_v \rho_v \lambda} \right) L_{eff} q \quad (4.3)$$

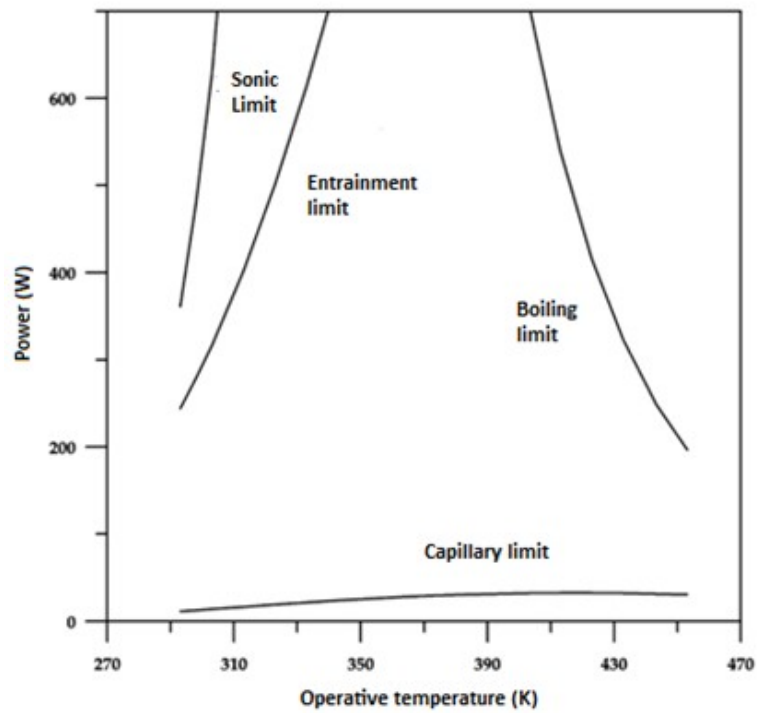
$$\Delta p_l = \left( \frac{\mu_l}{KA_w \lambda \rho_l} \right) L_{eff} q \quad (4.4)$$

where  $r_{h,v}$  is the hydraulic radius of vapor space,  $C$  is a constant that depend on Mach Number,  $\mu_v$   $\mu_l$   $\rho_v$   $\rho_l$  are respectively dynamic viscosity and density of vapor and liquid phase,  $L_{eff} = L_{Evaporator} / 2 + L_{Adiabatic} + L_{Condenser} / 2$  is the effective length,  $A_w$  the wick area,  $\lambda$  the latent heat of vaporization and,  $K$  the permeability of wick structure and  $q$  the hat flux.

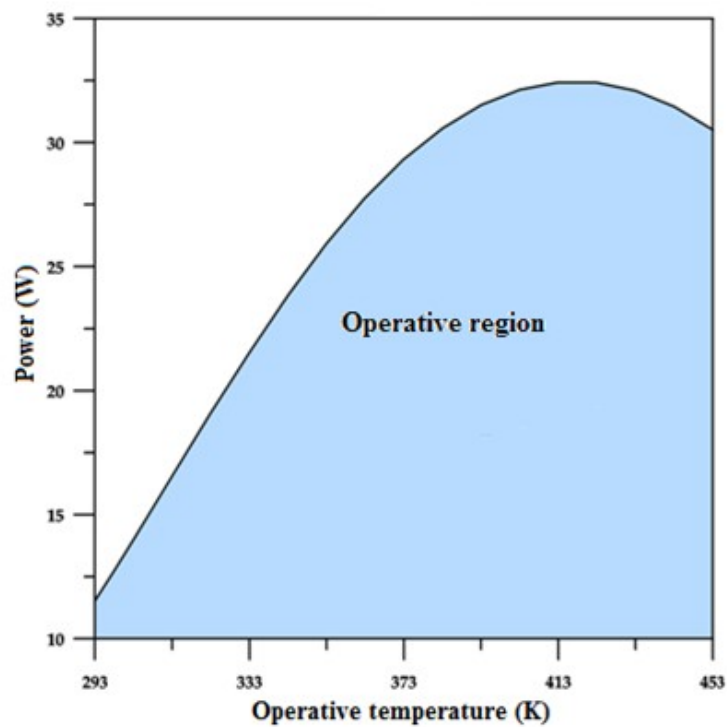
Sonic, entrainment and boiling limit has been obtained by model proposed in ref. (4). The main heat transfer limitations analyzed are:

- Boiling Limit- occurs when the radial heat flux into the heat pipe causes the liquid in the wick to boil and evaporate causing dry-out.
- Entrainment Limit- at high vapor velocities, droplets of liquid in the wick are torn from the wick and sent into the vapor. Results in dry-out.
- Sonic limit- occurs when the vapor velocity reaches sonic speed at the evaporator and any increase in pressure difference will not speed up the flow; like choked flow in converging-diverging nozzle. Usually occurs during startup of heat pipe.

Figure 4.5 show the operative limit of heat pipe system (Figure 4.5a)) and the operative region of heat pipe (Figure 4.5c)).



a)



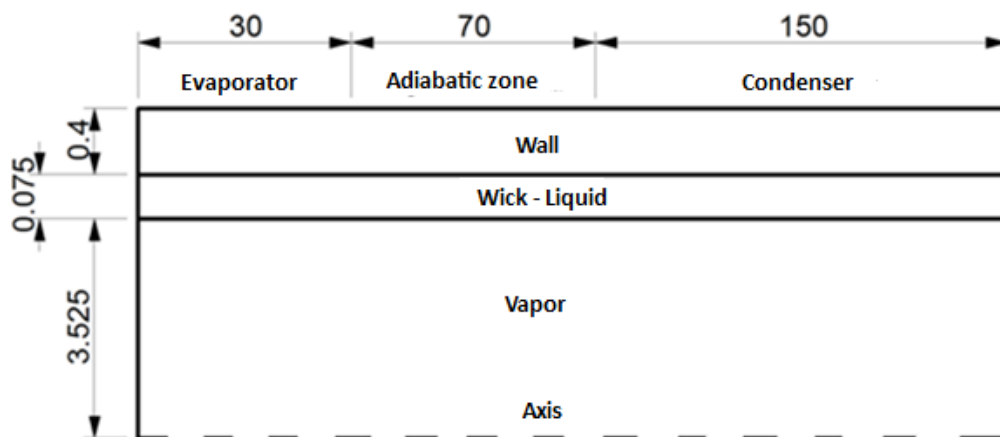
b)

Figure 4.5 – a) operative limit of heat pipe b) operative region due to the capillary limit.

The main limit is the capillary limit (Figure 4.5a)). Depending on the operative temperature of the heat pipe the capillary limit can occur at different input power voltage (Figure 4.5b)) defining the operative region of heat pipe.

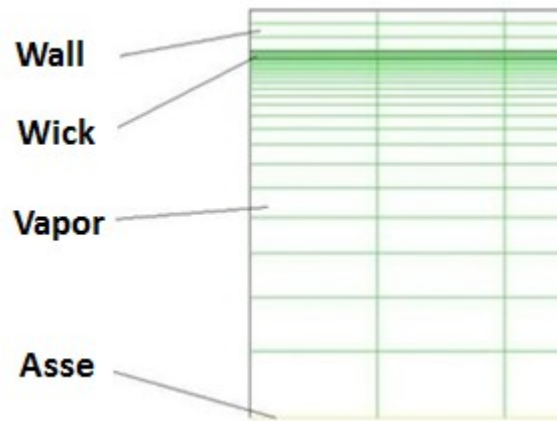
#### 4.4.2 Numerical simulation

Transient numerical simulation has been carried out to better investigate the behaviour of groove heat pipe using a model proposed in literature [59]. Figure 4.6 show a sketch of numerical model used for the simulation.



**Figure 4.6 - Sketch for the groove heat pipe used for the numerical simulation.**

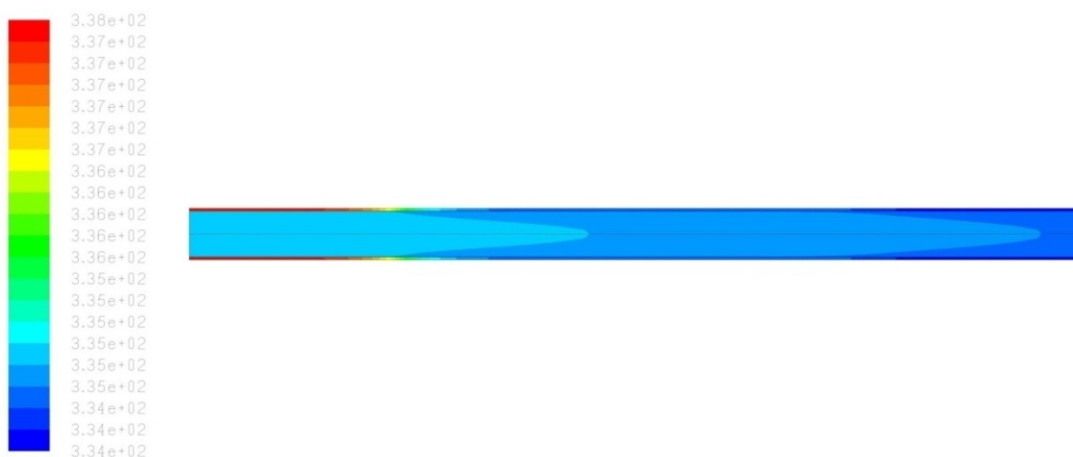
Heat pipe has been modeled using an axial-symmetric model with a lateral wall, a vapor zone and a wick structure modeled as a porous material. The geometry is the same used for the analytical model (see Figure 4.4). The computational domain consist of vapor core, the wick and the walls of the heat pipe (see Figure 4.7).



**Figure 4.7 - Geometrical model of groove heat pipe.**

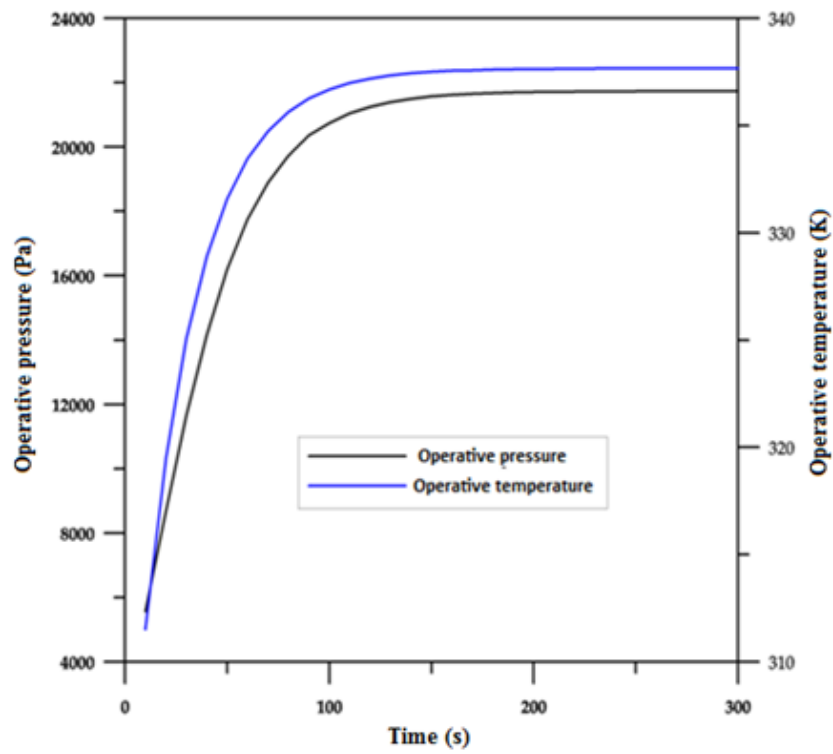
Due to the little dimension of wick structure the grid has been refined at liquid-vapour interface to improvement the resolution. The liquid vapor interface is assumed to be coincident with the interface between the vapor core and the wick. Thus, the computation assume that there is sufficient capillary head to pull the free surface to the vapor/wick interface. Flow, temperature, and pressure fields are computed under this assumption and are evaluated “*a posteriori*” for consistency.

Figure 4.8 show the temperature distribution at steady state conditions for a power input of 10 W.

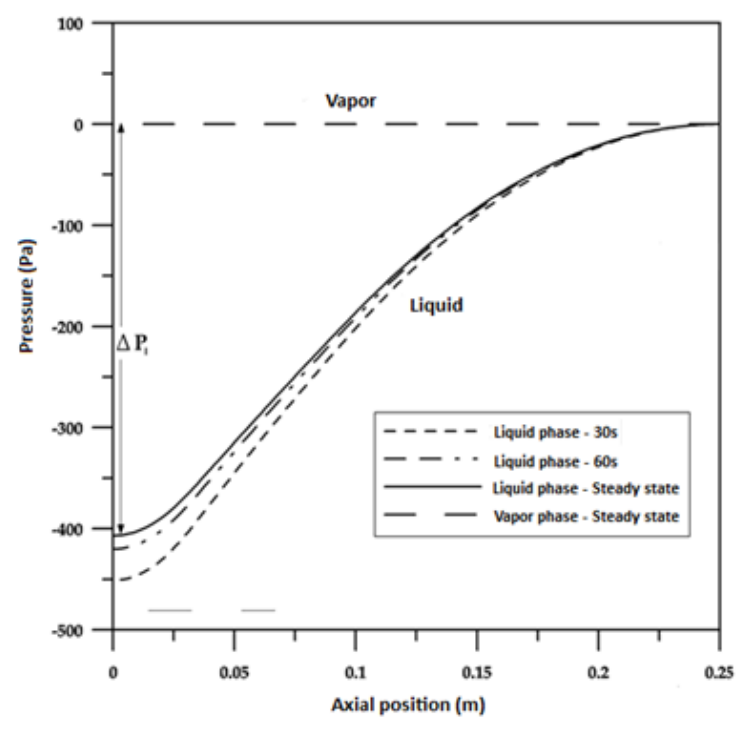


**Figure 4.8 - Temperature distribution of liquid and vapor at steady state condition.**

Figure 4.9a) show the transient operative and temperature pressure of vapour.



a)



b)

Figure 4.9 - Transient variation of the pressure and temperature vapour.

Figure 4.9b) show the transient and steady state value of pressure loss in liquid and vapor phase. Numerical simulation has been repeated until the maximum capillary pressure inside the groove reach the sum of liquid and vapour pressure loss, i.e. dry-out condition. Results show that dry-out conditions are established for a power input of 13Watt.

#### **4.4.3 Experimental result**

Thermal test has been carried out using the apparatus described in the previous paragraphs for a filling ratio (i.e. the ratio between liquid and total pipe volume) of 4%. During each test a prescribed electrical power is supplied to the cartridge heaters, providing the initial input voltage and therefore the initial power to the different heat pipes. During this phase the voltage, current and the thermocouples signals are continuously detected and shown in form of charts on the laptop monitor. At this point in the tests, it took approximately 20 minutes to reach steady state. Once the steady-state condition had been reached, the temperature distribution along the heat pipe is measured and recorded, along with the other experimental parameters. The power input is then increased incrementally, and the process repeated until dryout occurs as determined by rapid spikes in the evaporator thermocouple farthest from the condenser. Once dryout was reached, the temperature difference between the evaporator and condenser rapidly increases.

In addition, thermal test has been carried out at different filling ratio. Research pointed out to investigate the effect of filling ratio on the thermal performances of groove heat pipe. The thermal resistance has been defined as  $R = \Delta T/Q$ , with  $\Delta T$  the temperature difference between the average temperatures at the evaporation region and at the condensation region, respectively, and  $Q$  the thermal input, i.e. the electric power provided by the cartridge heaters. Experimental result are show Figure 4.10.

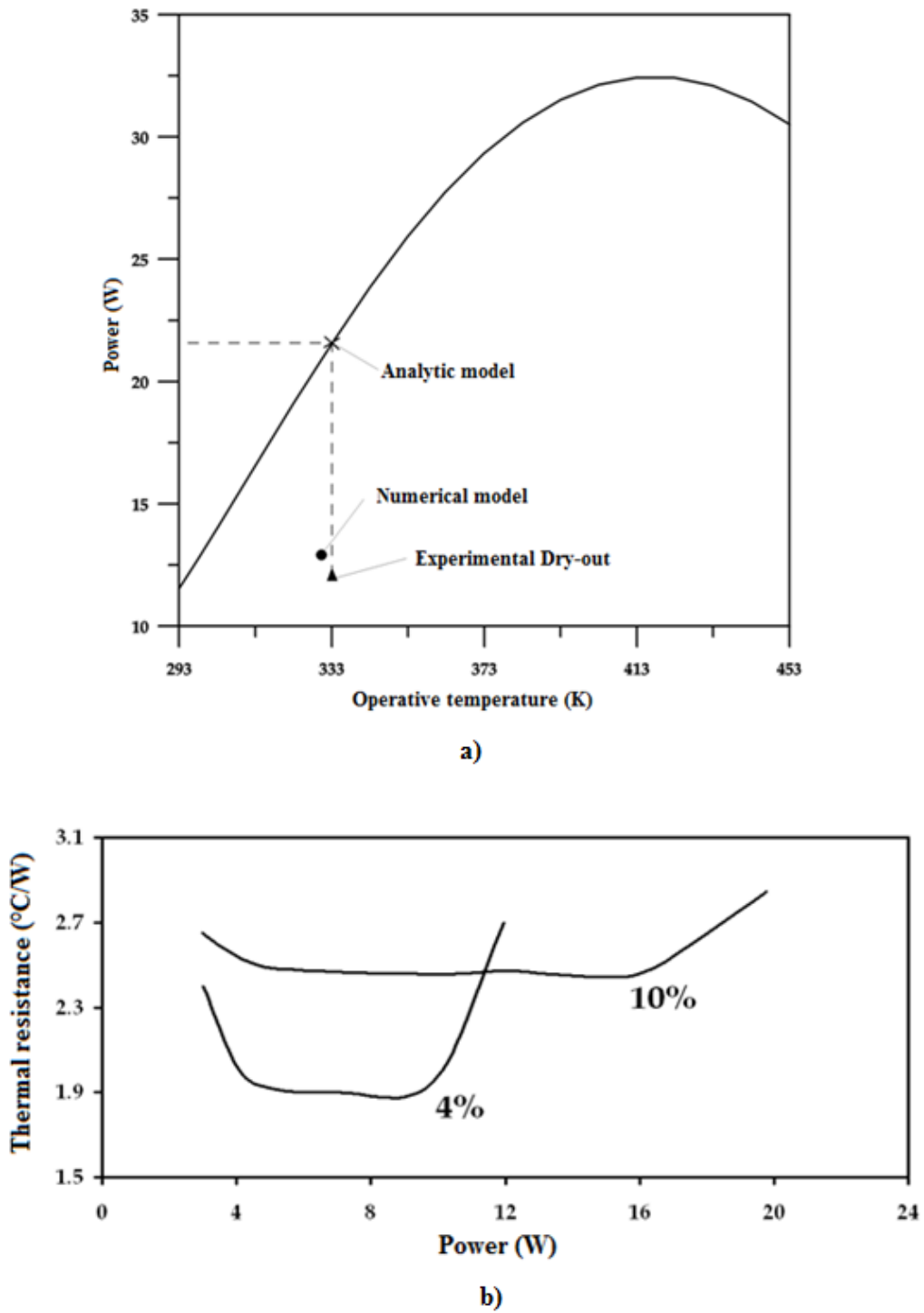


Figure 4.10 - Comparison between experimental, numerical and analytical result. a) capillary limit of heat pipe system, b) thermal resistance at different filling ratio.

Figure 4.10a) show a comparison between analytic model, numerical model and experimental result for the grove heat pipe filled with a filling ratio of 4%. Experimental dry-out has been reached at a power input of 13Watt. Experimental results are in good agreement with the numerical result. The discrepancy with the analytical prediction is due to errors arising from approximations of the model and the introduction of effective length, which, reducing the viscous losses, extended the capillary limit.

Figure 4.10b) show the thermal resistance for heat pipe with different filling ratio. Result show that the dry-out limit increase with filling ratio, so based on the range power where the heat pipe must operate is possible to select the filling ratio. This is important because range power for heat pipe experiment is 0/40W.

## **4.5 A comparative study of different working fluid**

A comparison between different fluids including aqueous alcoholic solutions and multicomponent brines have been investigated as candidate working for heat pipes for space applications. Preliminary flow visualization has been carried out using capillary glass tube. The goal of this experimental session was to analyze the heat transfer characteristics associated with the particular Marangoni flow expected for the self-rewetting solution and self-rewetting brine and to compare the results with pure fluids, using a preliminary configuration. Then thermal characterization of copper heat pipe filled with ordinary and self-rewetting solution has been carried out using.

### **4.5.1 Flow visualization in glass capillary**

Preliminary flow visualization experiments have been performed with glass capillary tubes with inner diameter 5mm, outer diameter 8mm and length 160mm [60]. The capillaries were partially filled with different working fluids. The filling ratio (i.e. the ratio between liquid and total pipe volume) was 30%. In order to establish a surface temperature gradient, the glass pipe was heated up with a thin copper wire, connected to a power supply, wrapped around the

outer surface for a length of 6 cm. The input power was in the range 10W-30W. The system was investigated in the vertical and horizontal configuration and at different inclinations with respect to the gravity vector, without additional cooling units (the only mechanism for heat transfer at the cold side of the pipe was radiation and natural convection)

The diagnostic system included an infrared thermal camera (Flir Thermacam SC3000) to detect the surface temperature distributions at the different experimental conditions and a CCD camera with a frame grabber, which allows to store digital images in a computer. Preliminary experiments have been carried out with water and binary self-rewetting fluids. Furthermore, the same configurations have been investigated with FP-40 brines and self-rewetting brines.

Figure 4.11 show the different boiling behaviour of heat pipes filled with water and with self-rewetting fluid, when the capillaries are in the vertical, gravity-assisted, configuration.

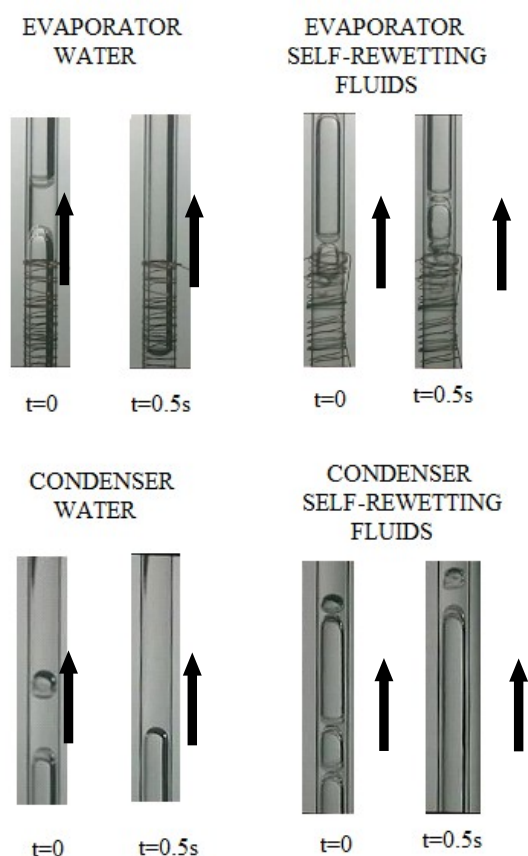


**Figure 4.11 - Boiling behaviour of heat pipes filled with water and with self-rewetting fluid in vertical configuration. Input power 18W.**

For the heat pipe filled with pure water there is more liquid in the condensation region and less liquid in the evaporation region in comparison to the heat pipe filled with self-rewetting fluid. No significant differences are evident in the merging behavior of vapour slugs. However, although the nucleation site (position and density) is different, for the self-rewetting liquid the size of vapour slugs, generated at the heating region, is much smaller in comparison to water. In this case a very wavy interface of the vapour slugs can be observed in the condensation region of the heat pipes filled with self-rewetting fluids, which implies a very strong liquid downward flow. Similar considerations apply to the case of heat pipes inclined  $45^\circ$  with respect to the gravity direction (Figure 4.12 and Figure 4.13).



**Figure 4.12 - Slug boiling behaviour in water  $\alpha = 45^\circ$ . Input power 18W.**

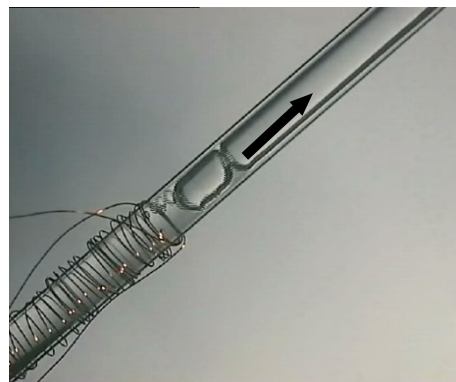


**Figure 4.13 - Slug boiling behaviour in self-rewetting fluid  $\alpha = 45^\circ$ . Input power 18W.**

When the heat pipes are in the horizontal configuration dry-out conditions are established in the evaporator of the capillary filled with pure water (see Figure 4.14). On the contrary, the

heat pipe filled with self-rewetting liquid still continues to operate (Figure 4.15), slug vapour bubbles are continuously generated and move from left to right toward the condenser, where the condensed liquid is spontaneously supplied at the evaporator. As in the case of Figure 4.14, the interface of the vapour slugs is very wavy, which implies a strong shear stress between vapour and liquid film around the slug.



**Figure 4.14 - Dry-out behaviour in water (horizontal). Input power 18W.**



**Figure 4.15 - Slug boiling behaviour in self-rewetting fluid (horizontal configuration). Input power 18W.**

The thermal performances of the wickless heat pipes have been evaluated by means of the IR thermocamera, measuring the surface temperature distributions along the cylindrical wall of each capillary. The results are summarized in Table 4-2. The thermal resistance, for the wickless heat pipe containing pure water, is higher than in the heat pipe filled with self-rewetting fluid. In particular in the horizontal configuration, the wickless heat pipe filled with water exhibits a higher temperature at the evaporator and a relatively lower temperature at the condenser and its thermal resistance becomes very large.

**Table 4-2 Thermal resistance of glass wickless heat pipe. Input power 18W**

Inclination	Liquid	Evaporator Temperature (°C)	Condenser temperature (°C)	Thermal resistance (°K/W)
Vertical ( $\psi = 90^\circ$ )	Water	137	113	1.3
	Self-rewetting fluid	130	118	0.66
Inclined ( $\psi = 45^\circ$ )	Water	143	103	2.2
	Self-rewetting fluid	135	105	1.66
Slightly inclined ( $\psi = 5^\circ$ )	Water	155	88	3.7
	Self-rewetting fluid	146	101	2.5
Horizontal ( $\psi = 0^\circ$ )	Water	205	70	7.5
	Self-rewetting fluid	156	101	3

A very similar behaviour was found for pure brines and self-rewetting brines. Typical examples are shown in Figure 4.16 for the capillaries filled with FP-40 and FP-40/heptanol, already show in Figure 4.14.

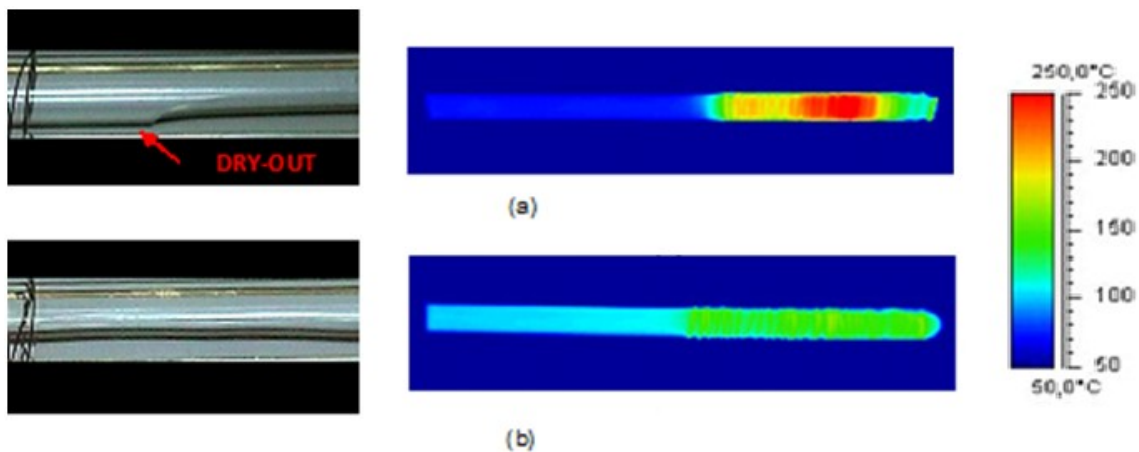


**Figure 4.16 - Digital and thermographic images of glass capillary in horizontal configuration filled with pure FP-40 (a) and with self-rewetting brine FP-40/heptanol solution (b). Input power 18W.**

The thermal resistance, for the heat pipe containing the pure brine is typically higher than in the heat pipe filled with self-rewetting brine. In particular, the heat pipe filled with FP-40 exhibits a very large temperature at the evaporator and a relatively smaller temperature at the condenser and its thermal resistance is growing in time due to dry-out at the evaporator.

The thermal image confirms that, due to the absence of liquid at the evaporator section, the temperature at evaporator increases and simultaneously the temperature at the opposite side

decreases. When the glass capillary is filled with self-rewetting brine, at the same input power, the temperature difference along the heat pipe axis is much lower. A comparison between self-rewetting fluids and self-rewetting brine is summarized in Table 4-3.

**Table 4-3 Thermal resistance of glass wickless heat pipe. Horizontal configuration. Input power 18W.**

<b>Liquid</b>	<b>Evaporator Temperature (°C)</b>	<b>Condenser temperature (°C)</b>	<b>Thermal resistance (°C/W)</b>
Water	205	70	7,5
Self-rewetting fluid	156	101	3
FP-40	250	50	11,1
Self-rewetting brine	160	100	3,3

Generally the thermal resistance, for the glass wickless heat pipe containing pure liquid, is higher than in the heat pipe filled with self-rewetting fluid. The preliminary result show that in wickless glass heat pipe self-rewetting-brine show the same behaviour of self rewetting fluid but with a high value of thermal resistance.

#### **4.5.2 Thermal characterization of copper wickless heat pipe**

A comparison between pure liquids (water), self-rewetting fluid and self-rewetting brine in a configuration quite similar to the flight payload has been carried out using BARE copper heat pipe and the test bench described in the previous paragraphs. The filling ratio in this case is 40%. The test bench is set in horizontal configuration.

Thermographic image in Figure 4.17 show the dry-out condition of the water heat pipe (top) and the good performances of heat pipes filled with self-rewetting fluid (down) and self-rewetting brine (centre) for a power input of 20 Watt.

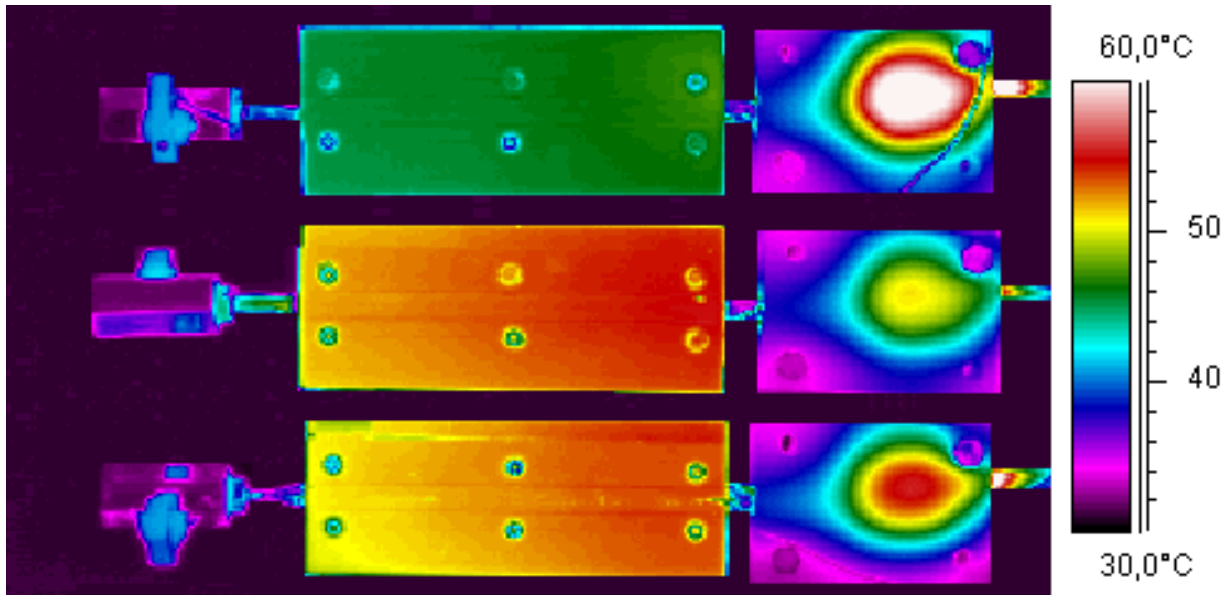


**Figure 4.17 - Thermographical image of copper wickless heat pipes with aluminum radiators filled water (top), self-rewetting brine (centre) and self-rewetting fluid (down).**

At the same input power voltage the temperature at evaporator side in the case of water is very high in comparison to the self-rewetting fluid and self-rewetting brine. This is due to the dry-out condition for the heat pipe filled with water. Contrary, for both self-rewetting solution the heat supplied to the evaporator section is correctly transferred to the condenser side.

Table 4-4 summarizes the values of the thermal resistance and the maximum temperature ( $T_{max}$ ) at the evaporator section for water, self-rewetting fluid (water/butanol solution) and self-rewetting brine (FP40/butanol solution), at different power input.

**Table 4-4 Thermal resistance of heat pipe filled with water, self-rewetting fluid, and self-rewetting brine.**

	Water		Self-rewetting fluid		Self-rewetting brine	
Q (W)	Thermal resistance (K/W)	T max (°C)	Thermal resistance (K/W)	T max (°C)	Thermal resistance (K/W)	T Max (°C)
10	5	109	0.52	63	0.8	67.3
20	>5 Dry-out	>160	0.43	86.2	0.6	93.7
30	-	-	0.41	114.6	0.6	127.1
35	-	-	0.35	126.3	0.73	146.3
40	-	-	Dry-out	>166.4	0.81	165

The heat pipe filled with water and self-rewetting fluid exhibits dry-out condition for a power value of 20 Watt and 35 Watt respectively. Heat pipe with self-rewetting brine, although exhibit higher value of thermal resistance compared to the pipe filled with self-rewetting fluid, do not reach the dry-out even for an input power of 40 W.

#### **4.6 Conclusion**

Different fluids including aqueous alcoholic solutions and multicomponent brines have been investigated as candidate working fluids for heat pipes for space applications. The flow visualization experiment performed with these liquid mixtures in different configuration have pointed out that pool thermal performances can be obtained using heat pipes filled with innovative self-rewetting fluids.

## 5 Marangoni convection in a shallow cell

### 5.1 Introduction

In this chapter, laboratory and numerical activities has been carried out to study the behaviour of thin liquid layers in the presence of horizontal thermal gradients. The liquids investigated exhibit different surface tension behaviour, i.e. usual decreasing surface tension with temperature or unusual surface tension behaviour, increasing with temperature (as for some water-alcohol solutions).

Experiments have been carried out in collaboration between the Microgravity Advanced Research and Support (MARS) Center and Microgravity Research Center of Université Libre de Brussels (MRC-ULB).

### 5.2 Experimental setup

Reverse Marangoni flow of water/alcohols solutions has been investigated in past both in microgravity [61] and on ground [62] condition. Results show that the surface motions going from a cold region to a hot region for temperatures higher than that of the minimum of the static surface tension.

As discussed in the present work, due to the evaporation–condensation phenomenon, both thermo-capillary and solutal Marangoni effect are responsible of these surface motion. In fact, any imposed temperature difference across a liquid-vapour interface creates a surface concentration gradient. Alcohol evaporates in the hot region of the surface and condenses in the cold one (27). The inversion of the Marangoni flow on the surfaces of water/alcohols

systems was observed for temperatures lower than that of the static surface tension minimum with a radial temperature gradient in a cylindrical geometry [63-64] and in an apparatus where motions can be assumed bi-dimensional [65]. In addition, it has been shown theoretically [66] and experimentally [67] that alcohol evaporation increases the surface tension. Thus, it is reasonable to assume that alcohol condensation has nearly the opposite effect. The solutal Marangoni effect, due to gradient concentration, can play a role in the reverse Marangoni flow in water/alcohols system but nevertheless has been investigated experimentally.

In this chapter reverse Marangoni flow has been investigated using a shallow cell. The cell has been designed to favor bi-dimensional flow and present a configuration close to heat transfer applications. The cell is a transparent optical quartz cuvette (external dimension: 12,5 mm, 3 mm, 45 mm and internal dimension: 10 mm, 1 mm, 39 mm) and present a configuration close to heat transfer applications (see Figure 5.1).

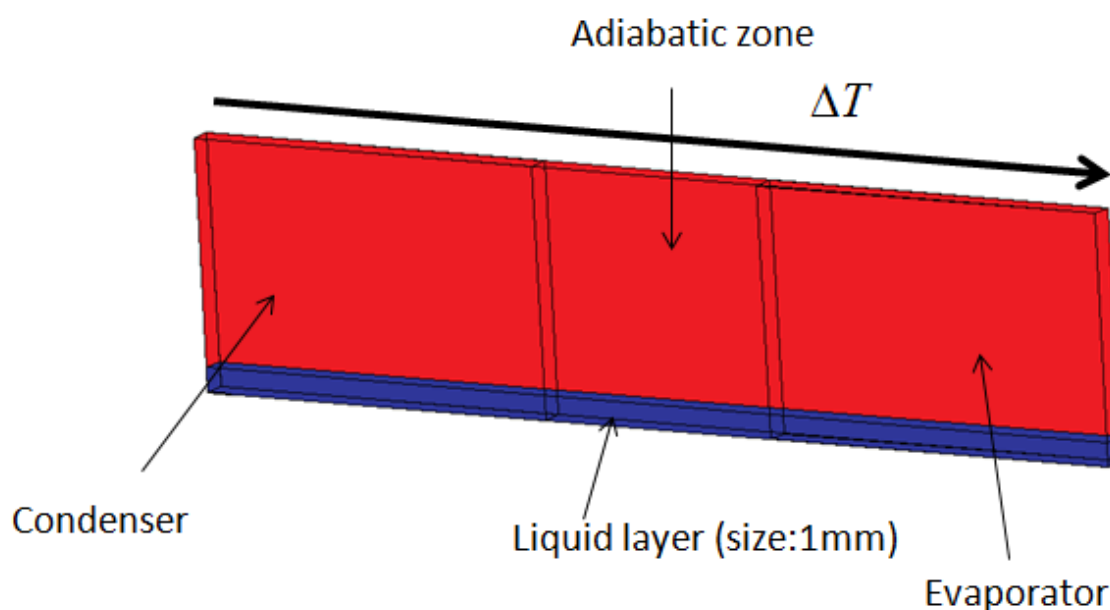


**Figure 5.1 - Sketch of shallow cell used for the experiments.**

Two opposite side of the cell are set at different temperature using an electrical nickel-chrome wire wrapped around the cell.

The target of the experiment was to observe the Marangoni flow at liquid-vapor interface. Flow visualization has been obtained using optical diagnostic systems. In particular, in order

to analyze the velocity field, preliminary experiments have been carried out adding tracer particles at the liquid and then a Mach-Zehnder interferometer has been used to measure the index of refraction variation of liquid.

The hotter end was chosen in order to confirm the existence of a surface tension driven flow directed toward the cold instead of the hot side in the case of self-rewetting solutions and analyze, by the index of refraction measurements, the existence of a solutal Marangoni effect for the water alcohols solutions.

The liquid investigate are listed in Table 5-1 with the classification based on the surface tension behaviour and the temperature of hot and cold side.

**Table 5-1 Liquid used in the experiment.**

<b>Fluids</b>	<b>Classification</b>	<b>T_cold (°C)</b>	<b>T_hot (°C)</b>
Ethanol	Ordinary	40	60
Water	Ordinary	40	60
Water-heptanol	Self-rewetting	40	60
Water-butanol	Self-rewetting	70	80

Two self-rewetting fluids have been investigated. The hotter end was fixed at 60 °C while the colder end at 40 °C for the water/heptanol solution and 70 °C and 80 °C for the water/butanol solution. These temperatures have been fixed after realizing that for the solution investigated, the minimum temperature at which the surface tension gradient starts to have a positive slope is near 40 °C for water/heptanol and near 70°C for water/butanol.

For pure liquids, in order to have a comparison between ordinary and reverse Marangoni flow the same temperature of water/heptanol has been used.

### **5.3 Flow visualization**

The target of the experiments was to observe the velocity field of thin liquid layer subject to a horizontal thermal gradient.

A parallel background illumination has been used to illuminate tracer particles of glass powder (diameter  $10\ \mu\text{m}$ , density  $450\ \text{kg}/\text{m}^3$ ) inside the test liquid, while a CCD camera recorded the tracers movements. Figure 5.2 show an example of particles tracked for the ethanol case.

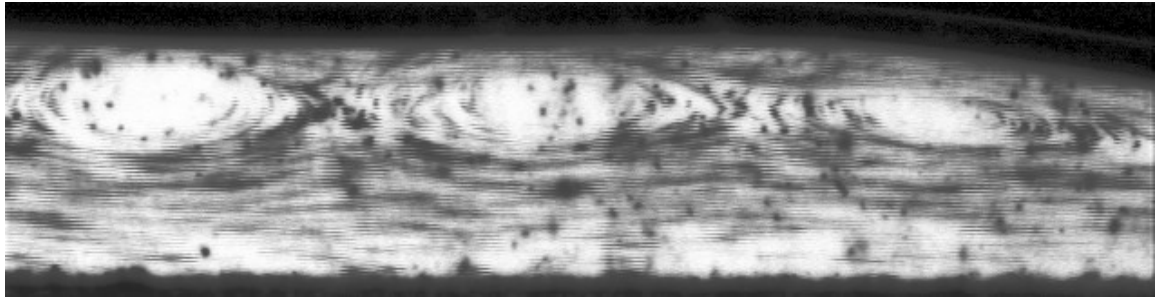


**Figure 5.2 - Tracks of aluminum particles seeded in the fluid.**

To have a qualitative idea of flow inside the liquid, small video clips were recorded and then analyzed monitoring the history of tracers inside the images.

Results of flow visualization are:

- 1) both self-rewetting solutions have show a self-rewetting behaviour, i.e. liquid at interface direct towards the hot side;
- 2) pure liquids, i.e. ethanol and water has show ordinary Marangoni flow direct towards the cold side;
- 3) a low velocity at interface has been observed for water.

In the next paragraphs the same experiments will be carried out using optical interferometry.

## 5.4 Mach Zehnder interferometry

A dedicated mach zehnder interferometer has been developed at MARS center laboratory to measure the index of refraction variation of the different liquids at the same configuration described in the previous paragraphs.

The system allow the possibility to use two-color. Two color interferometry is capable of separating two quantities from the cumulative interference data. Basically two interferograms under identical conditions but with different wavelengths are obtained. At each point, these fringes yield cumulative refractive index information. However, for binary mixtures, the refractive index can be a function of temperature and concentration. Having two independent relationships, the two quantities can be separated. Figure 5.3 show a view of the optical bench.

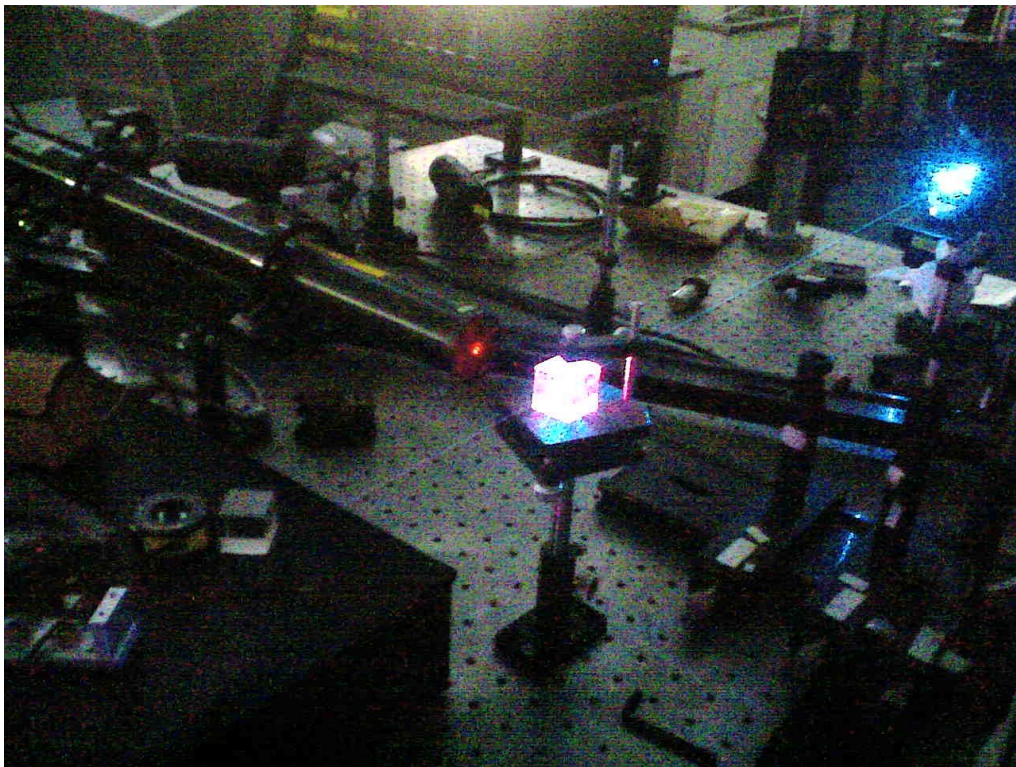
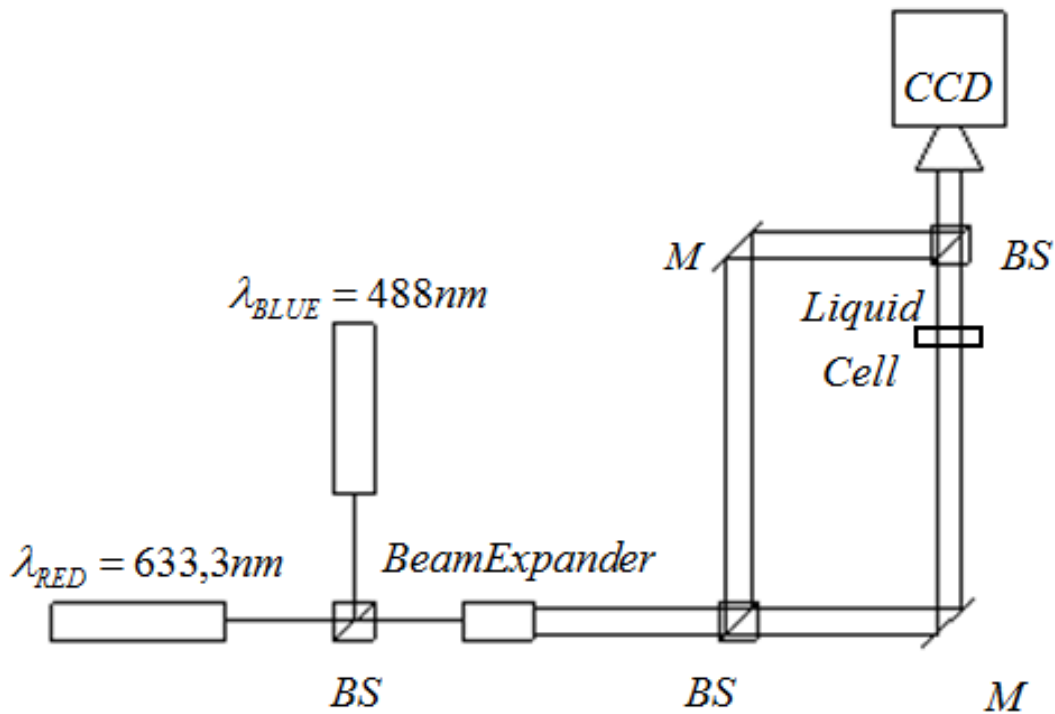


Figure 5.3 - View of two-color mach zehnder setup developed at MARS laboratory.

Figure 5.4 show the scheme of optical set-up.



**Figure 5.4 - Mach-Zehnder experimental set-up**

The He-Ne laser beam ( $\lambda_{RED} = 633.3\text{nm}$ ) is expanded and cleaned using a spatial filter, towards a beam splitter, which splits it into a reference beam and an object beam. The reference beam passes through the ambient air while the object passes through the test cell. Finally, the two beams are recombined by a second beam splitter and imaged on a CCD camera by a Micro-Nikor objective with a focal length of  $20\text{mm}$ . Due to refractive index differences inside the cell, the optical paths of the two beams are different and an interference pattern is recorded. A second laser beam ( $\lambda_{BLUE} = 488\text{nm}$ ) is directed towards the beam expander using a beam splitter mounted above the spatial filter, in this way the optical path of the two laser beam are the same.

The entire interferometer is mounted on an optical table to isolate the system from environmental vibration.

The experimental procedure includes the following steps:

- 1) a liquid layer of  $1\text{mm}$  is established inside the cell;
- 2) when the temperature is constant (equal to the ambient temperature) a reference image is detected;

3) a temperature gradient is established (typically the left wall is set at 40°C and the right wall at 60°C);

4) the interference fringes are detected during the transient period until steady state conditions are established.

Figure 5.5 shows an example of the change in interference pattern at reference and steady state conditions.

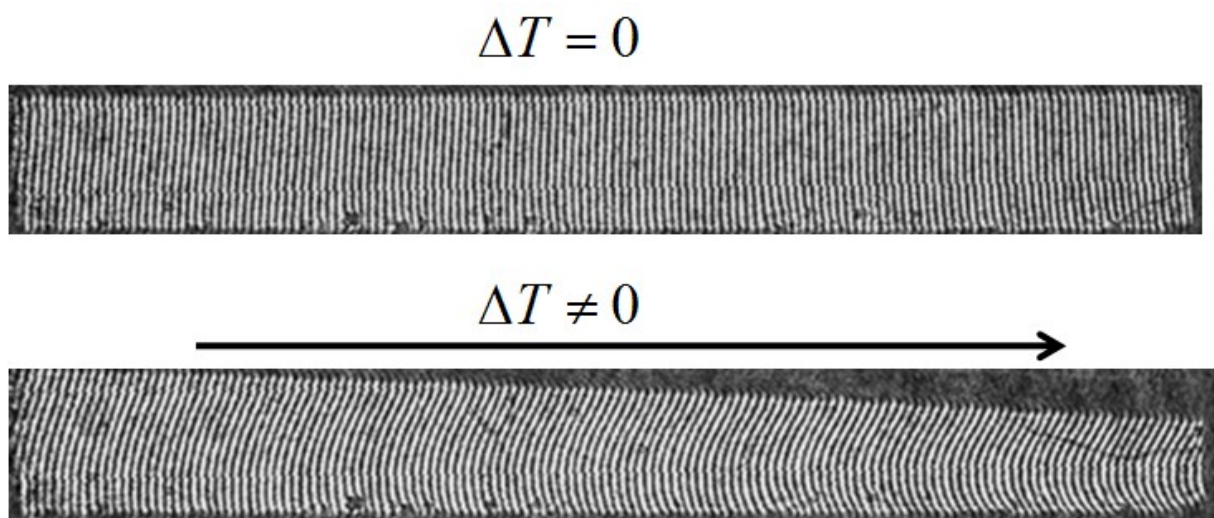


**Figure 5.5 - Change in interference pattern at initial and steady state condition.**

The change in refractive index evaluated by difference between the initial and steady state condition after a post-processing of image.

#### **5.4.1 Index of refraction measurements**

Measurements of index of refraction for water alcohols solutions have been carried out at sodium D-line wavelength ( $\lambda_D = 589.3nm$ ) using an Abbe Refractometers. The systems allow the possibility to measure the index of refraction with an accuracy of  $\pm 0.0002$  at different concentration and different temperature using a water circulation system. Experimental results are show in Figure 5.6.

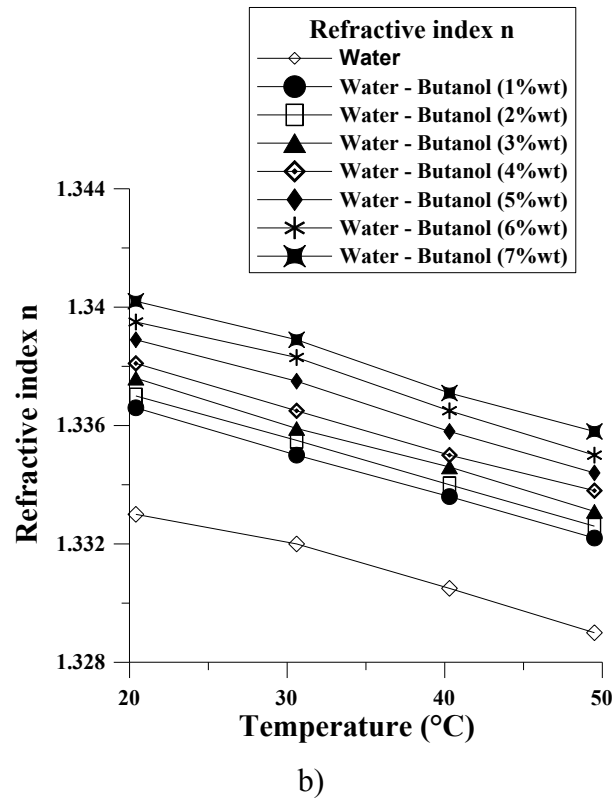
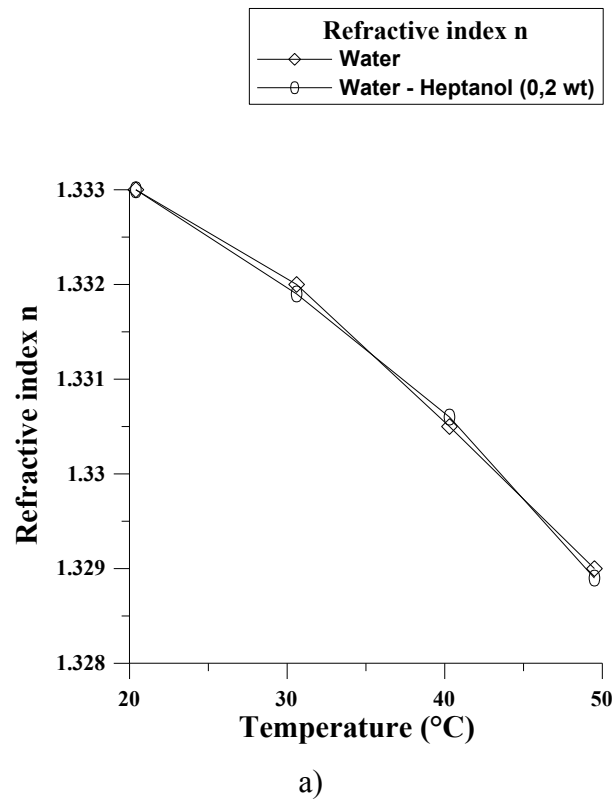


Figure 5.6 - Refractive index measurements. a) water/heptanol, b) water/butanol.

Figure 5.6 a) show the index variation for water and water/heptanol solution. In this case the refractive index is the same of water so the index of refraction is function only of temperature. This is due to low solubility of heptanol in water.

For water butanol solution the refractive index has been measured at different concentration of butanol in water (Figure 5.6 b)). The refractive index is function of both the temperature and concentration. So, in order to retrieval information with interferometer, is necessary to use two leaser with two different wavelength.

### 5.4.2 Data processing

An image processing program has been developed to extract the variations of the refractive index from the interference pattern. The method, based on the two-dimensional Fourier Transform, is described in Ref. [71]. The carrier phase component can be removed in the frequency domain via a spectrum shift. The center of fundamental frequency component is shifted to the center of the frequency spectrum shifting by  $-f_x$  in the  $x$  direction and  $-f_y$  in the  $y$  direction. An inverse Fourier transform of the shifted spectrum would produce a phase distribution without the carrier phase component.

The routine employed involves the following steps (see Figure 5.7):

- 1) performing a two-dimensional Fourier transform of the interferogram;
- 2) applying a filter operation;
- 3) performing a frequency shift in the Fourier transform plane, so that the data is located around zero frequency;
- 4) performing a two-dimensional inverse Fourier transform;
- 5) determining the phase by evaluating the arctangent of the ratio of the imaginary and real parts of the inverse transform:

$$\Delta\phi(x, y) = \arctan\left(\frac{Im}{Re}\right) \quad (1.1)$$

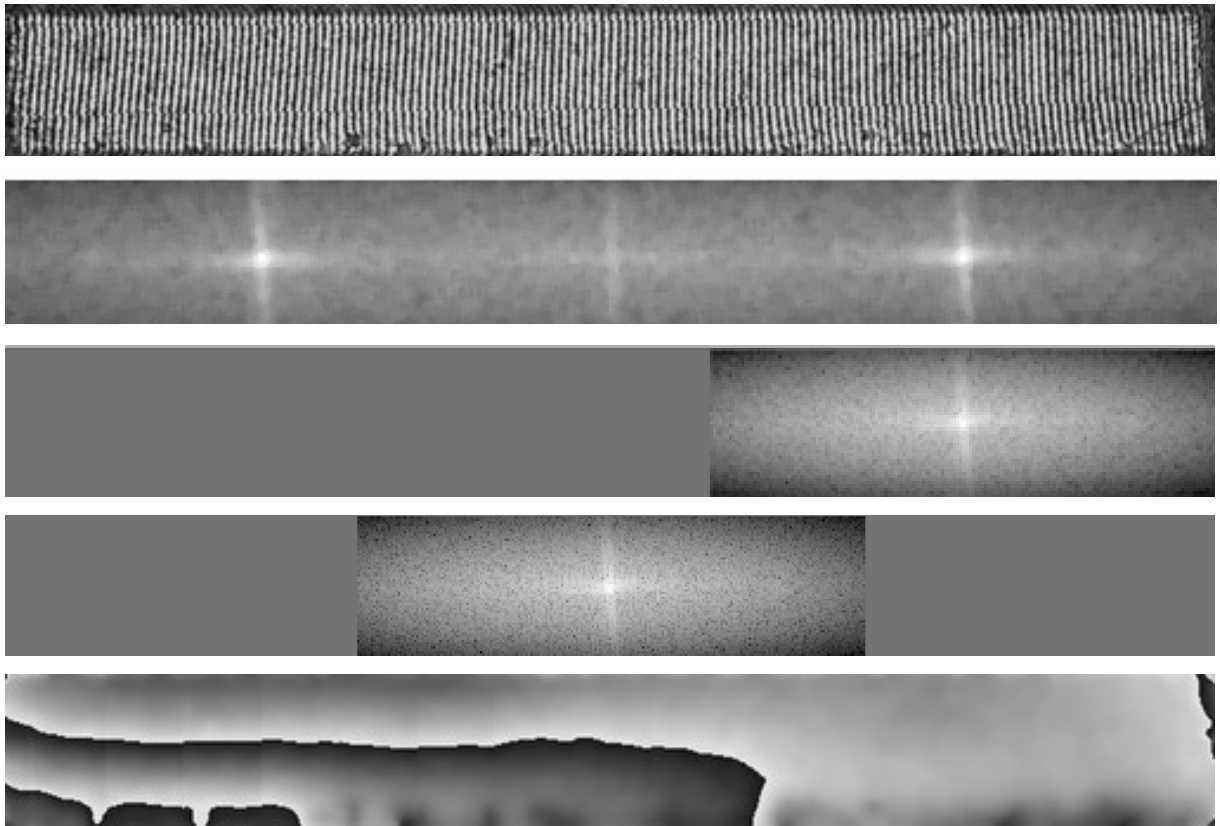


**Figure 5.7 - Routine employed to retrieval the phase by the fringe pattern using FFT.**

Finally, the phase variation can be evaluated by the difference between the phase at stationary condition and the initial phase (see Figure 5.8).

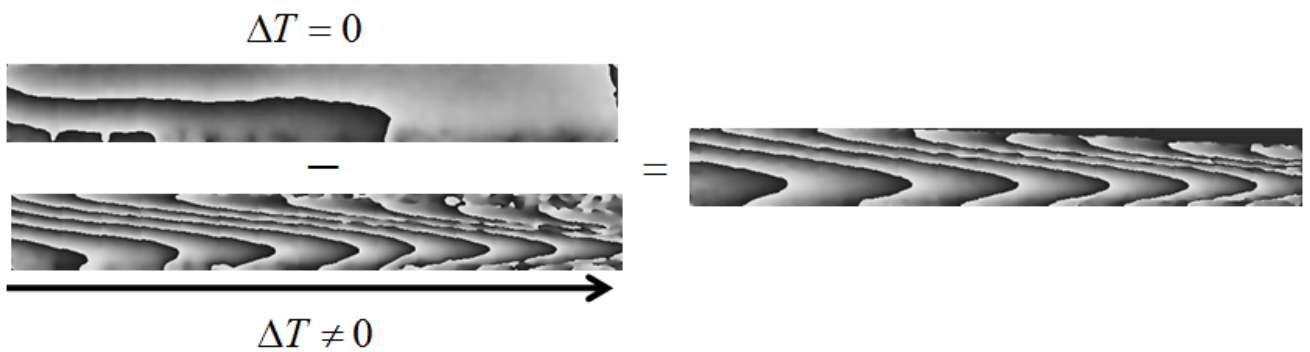
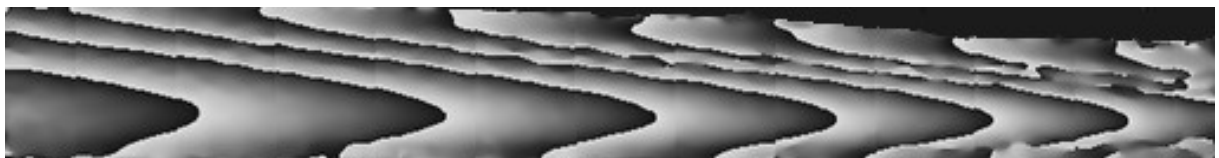


**Figure 5.8 - Unwrapped phase between steady-state and initial condition.**

### 5.4.3 Laboratory results

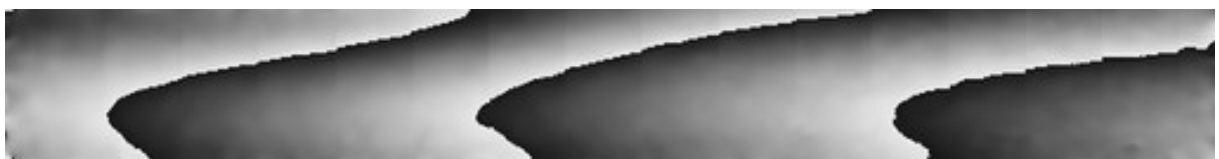
Experiments for pure liquids and water/heptanol solution has been carried out using only red color. Figure 5.9 show unwrapped iso-phase image detected for ethanol, water and water/heptanol solution.



a)



b)



c)

**Figure 5.9 - Unwrapped phase for pure liquid and water heptanol solution. a) ethanol, b) water, c) water-heptanol.**

In this case, phase variation is proportional to the index of refraction variation that depend on the temperature ( $n = n(T)$ ). For the water/heptanol solution the variation of refractive index due to the concentration has been neglected for the low solubility of heptanol in water.

The change in refractive index  $\Delta n(x, y)$  was calculated by the relationship between the phase difference  $\Delta\phi$  and  $\Delta n(x, y)$  [72]:

$$\frac{\Delta n(x, y)d}{\lambda_{RED}} 2\pi = \Delta\phi(x, y) \quad (5.2)$$

$$\Delta n(x, y) = \frac{\Delta\phi(x, y)\lambda_{RED}}{2\pi d} \quad (5.3)$$

$$n(x, y) = n_0 + \Delta n(x, y) \quad (5.4)$$

where  $d = 1\text{mm}$  is the size of the cell.

The phase variation  $\Delta\phi(x, y)$  has been obtained unwrapping the iso-phase image using a quality-guided path unwrapping algorithm [73].

Data for refractive index as a function of temperature was founded in literature and are listed in Table 5-2.

**Table 5-2 Coefficient of refractive index with temperature**

Liquids	$\frac{\partial n}{\partial T}$
Ethanol	0,0002
Water	0,0001
Water-heptanol	0,0001

Figure 5.10 show the temperature map retrieval by the post processing process. Figure 5.10a) show the isothermal for the ethanol case. The deformation of isothermal towards the cold side indicate a strong liquid in flow at interface direct from the hot side to the cold side due to the thermo-capillary effect (Ordinary Marangoni flow). The same experiment has been repeated with water. The result show that the thermo-capillary effect is null, the slow convection at interface is due to a buoyancy effect Figure 5.10b).

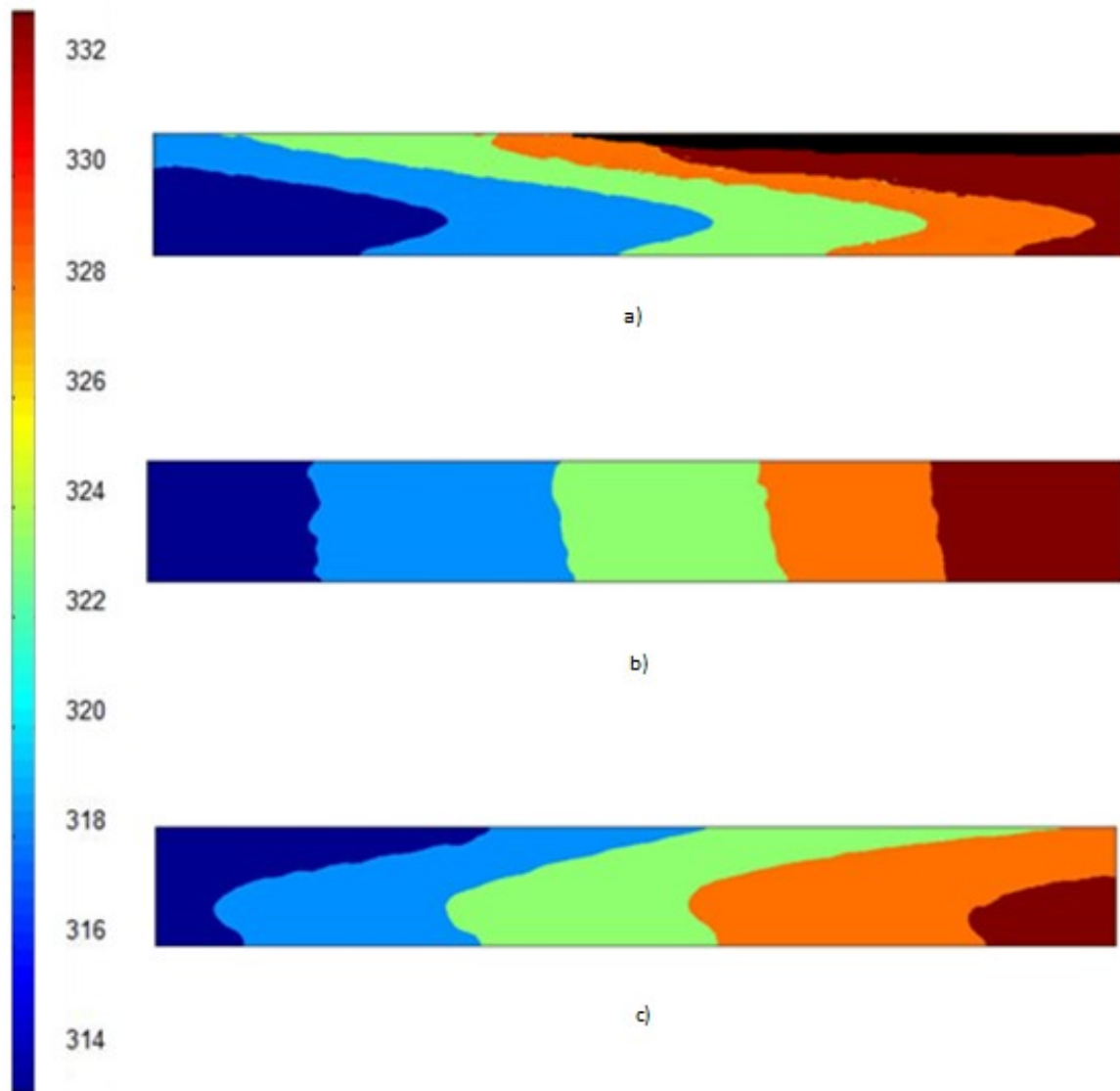


**Figure 5.10 - Temperature map. a) ethanol, b) water, c)water/heptanol mixture**

Figure 5.10c) show the results obtained when “inverse” Marangoni flow, due to the positive surface tension derivative with temperature, is superimposed to natural convection. In particular, the surface velocity, direct from the cold (left) towards the warm (right) side is responsible for an evident deformation of isothermal close to the liquid-vapor interface.

## 5.5 Numerical simulation

Numerical simulation has been carried out to better interpret the experimental result. Figure 5.11 show the geometric model used. In this case three-dimensional simulations have been carried out.

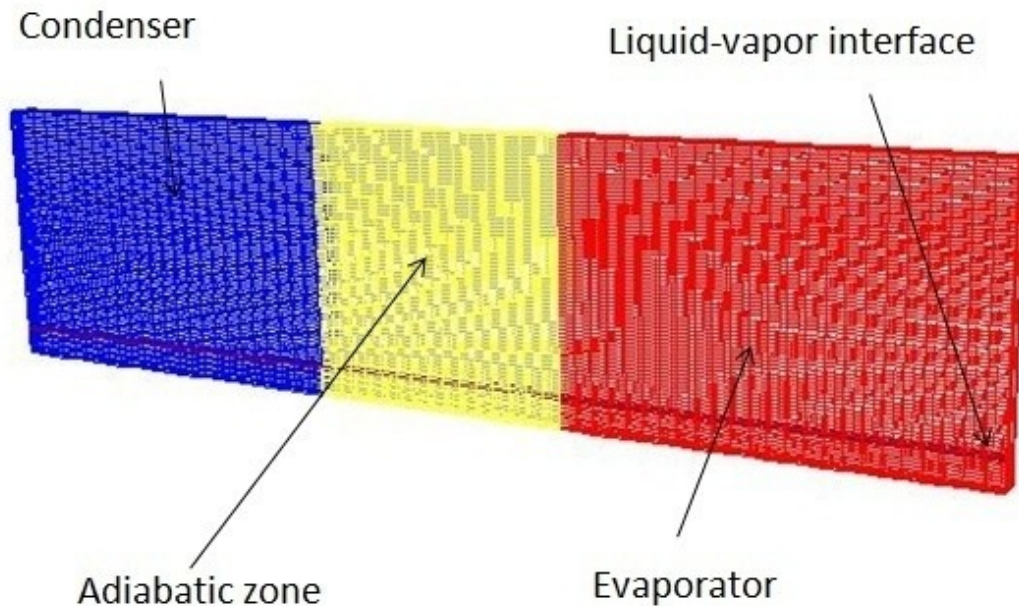


**Figure 5.11 - Geometric model of quartz cuvette.**

The theoretical model for this problem, involving a two-phase flow with a liquid–vapor interface, is based on the solution of the continuity, Navier–Stokes and energy equations for a viscous incompressible liquid; the boundary conditions at the liquid–vapor interface are the continuity of the mass flux and the surface balance equation of tangential momentum. The interface tension at interface generates a velocity at the interface and is balanced by tangential viscosity forces. The equilibrium condition at interface, indicate by subscripts “1” and “2” (the two fluids at the two sides of the interface shown in the Figure 5.12), reads:

$$\underline{\nabla}_s \sigma = \mu_2 \left. \frac{\partial V}{\partial n} \right|_2 - \mu_1 \left. \frac{\partial V}{\partial n} \right|_1 \quad (5.4)$$

where  $\sigma$  is the surface tension,  $\mu_1$  and  $\mu_2$  are the viscosity at liquid and vapor interface,  $V$  the interface velocity, and  $n$  the versor normal at interface.

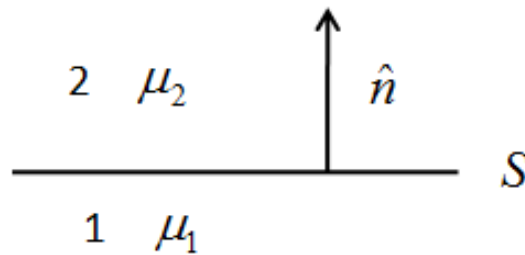


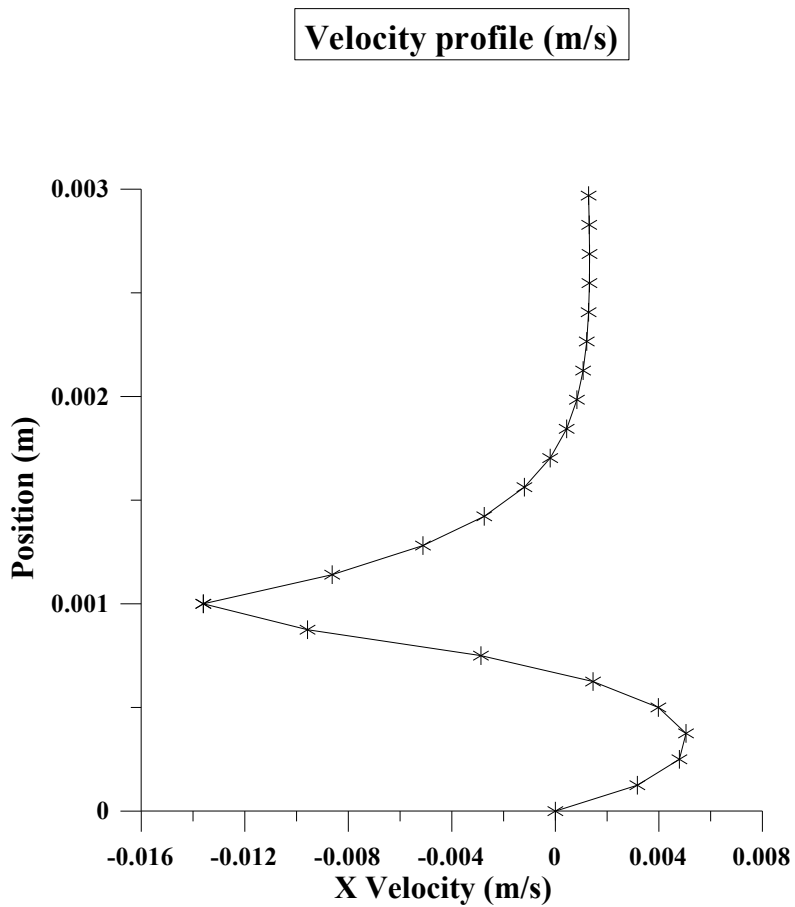
**Figure 5.12 - Scheme of air-liquid interface.**

The shear stress at liquid-vapor interface have been implemented through user-defined functions (UDFs). The value of the surface tension derivative in the case of ethanol and water/heptanol solution has been evaluated by the surface tension measurements and are listed in Table 5-3.

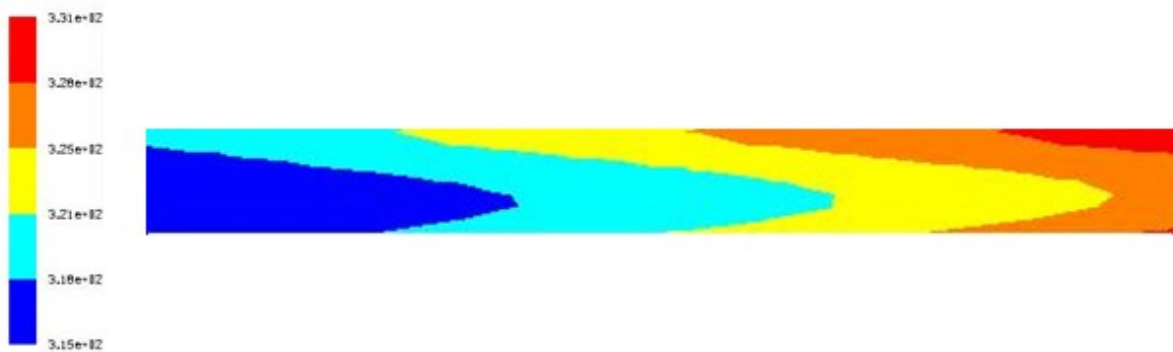
**Table 5-3 Surface tension derivative used in the numerical simulation.**

<b>Liquids</b>	$\sigma_T \left( \frac{N}{mK} \right)$
Ethanol	-8e-5
Water	0
Water-heptanol	9,6e-5

For the water – heptanol solution a medium value between 40/60°C has been considerate. In the case of pure water, due to the high contamination of water, the Marangoni effect is null. The above figure show the result of the numerical simulation for the liquid analyzed (Figure 5.13-Figure 5.15).



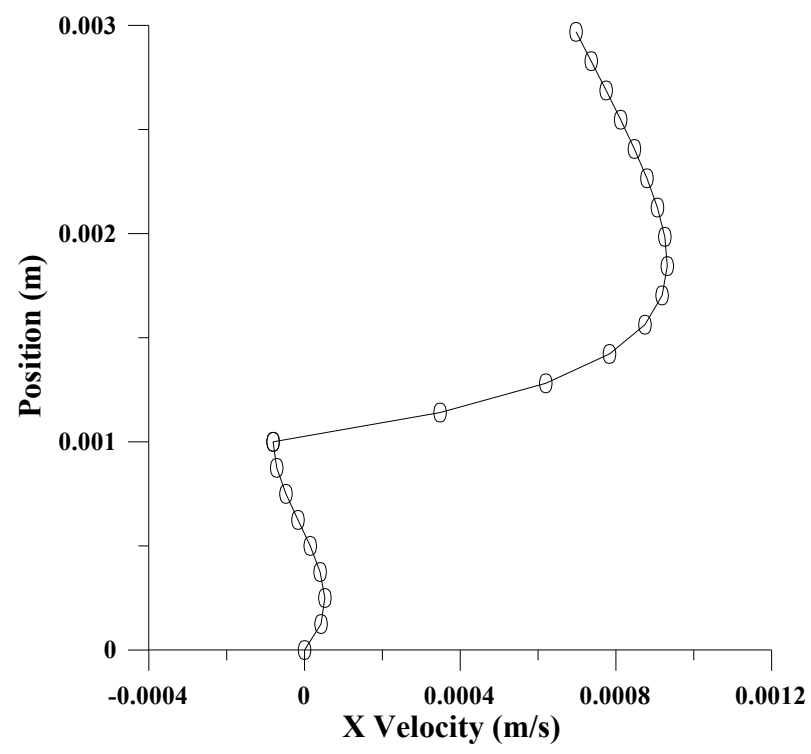
a)



b)

**Figure 5.13 – Numerical results of Marangoni flow – Ethanol. a) Velocity profile, b) temperature map**

Velocity profile (m/s)

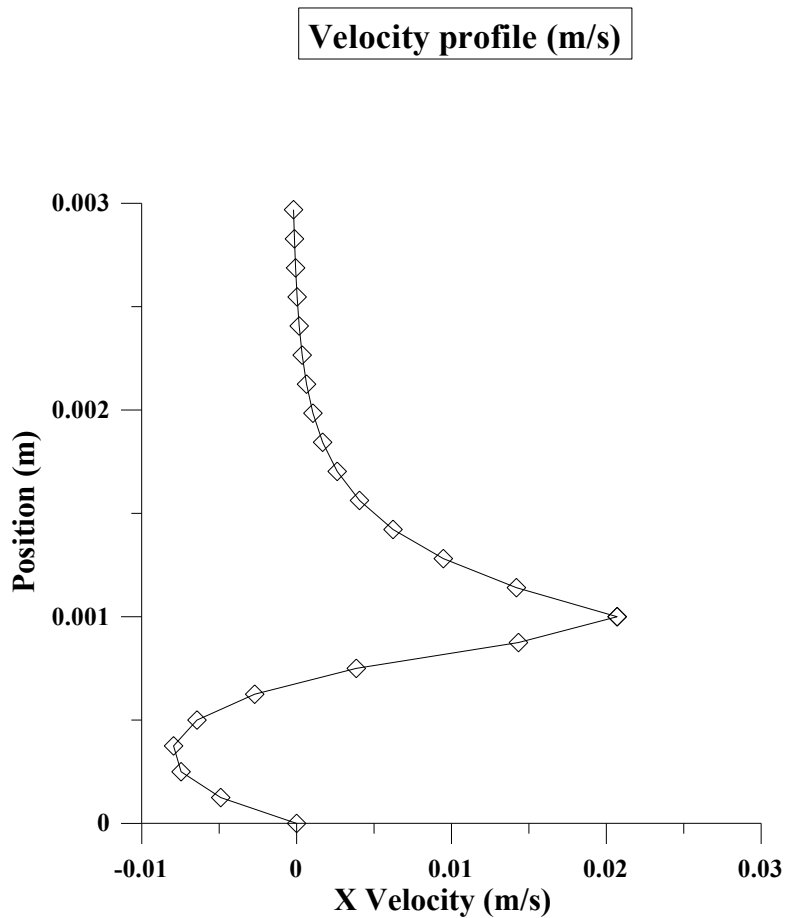


a)

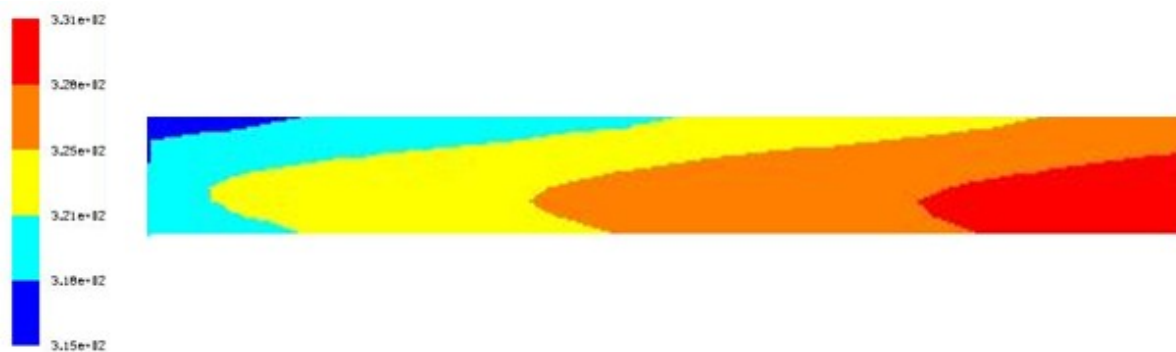


b)

Figure 5.14 - Numerical results of Marangoni flow – Water. a) Velocity profile, b) Temperature map



a)



b)

Figure 5.15 - Numerical results of Marangoni flow – Water/heptanol. a) Velocity profile, b) Temperature map.

Numerical results are in good agreement with the experimental results obtained with the Mach-Zehnder interferometer (see Figure 5.10). Figure 5.16 show a comparison between the velocity profile of ordinary and self-rewetting fluid obtained by the numerical simulation.

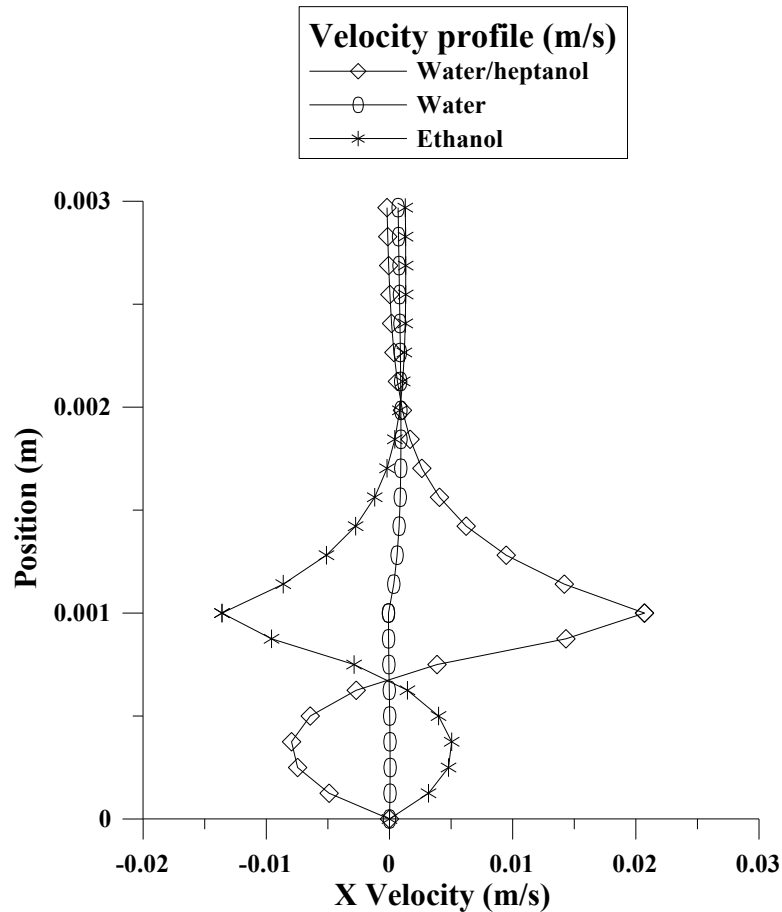


**Figure 5.16 - Comparison between the three different case**

For self-rewetting fluid, contrary to the ordinary liquid, the reverse Marangoni flow at liquid-vapour interface spontaneously driven liquid to the hot side of the cell.

### 5.6 Two-wavelength Mach Zehnder interferometer: water butanol case

As discussed in the introduction self-rewetting fluids are particular solutions that over an anomalous behaviour of surface tension with temperature show a positive effect due to a gradient concentration along the liquid-vapour interface. To investigate this effect a water/butanol solution (5%wt) has been investigated using two-color Mach-Zehnder system.

Figure 5.17 show the unwrapped iso-phase image acquired during the experiment at two different wavelength.



a)



b)

**Figure 5.17 - Unwrapped iso-phase for water/butanol solution. a)  $\lambda_{RED} = 633.3nm$ , b)  $\lambda_{BLUE} = 488nm$**

Also in this case the distortion of iso-phase toward the hot side show a reverse Marangoni flow at liquid-vapour interface. For practical application, two-color interferometry assumed linear refractive index variation against temperature and concentration [74]. The variation of index at two different wavelength are given by the relationship:

$$\begin{cases} \left( \frac{\partial n}{\partial c} \right)_{RED} \Delta c + \left( \frac{\partial n}{\partial T} \right)_{RED} \Delta T = \frac{2\pi d \Delta \phi_{RED}}{\lambda_{RED}} \\ \left( \frac{\partial n}{\partial c} \right)_{BLUE} \Delta c + \left( \frac{\partial n}{\partial T} \right)_{BLUE} \Delta T = \frac{2\pi d \Delta \phi_{BLUE}}{\lambda_{BLUE}} \end{cases} \quad (5.5)$$

The value of the coefficient of refractive index with mass fraction and temperature at two wavelength has been provided by Prof. Tanaka of Shibaura Institute of Technology and are listed in Table 5-3.

**Table 5-4 Coefficient of refractive index with mass fraction and temperature.**

$\left(\frac{\partial n}{\partial T}\right)_{RED}$	$\left(\frac{\partial n}{\partial c}\right)_{RED}$	$\left(\frac{\partial n}{\partial T}\right)_{BLUE}$	$\left(\frac{\partial n}{\partial c}\right)_{BLUE}$
0,000909	-0.000141	0.000837	-0.000159

Figure 5.18 show the temperature and concentration map obtained by the iso-phase.

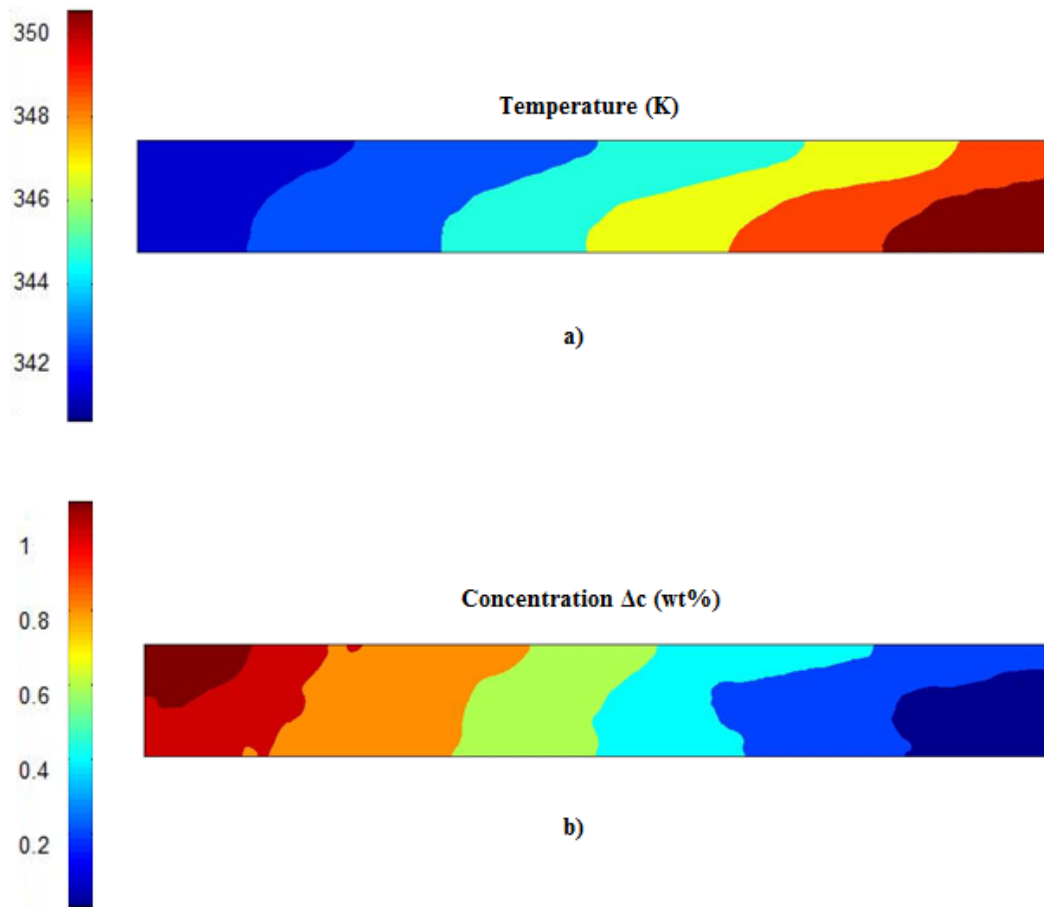


**Figure 5.18 - Temperature and map concentration for water butanol solution.**

A thermo-capillary and solutal effect, due to evaporation-condensation process is established between cold and hot side of the experimental cell. So, the experiment highlighted the self-wetting behaviour of self-wetting fluid.

To quantify the two effect separately the temperature and concentration profile at liquid-vapour interface have been evaluated (see Figure 5.19 and Figure 5.20).

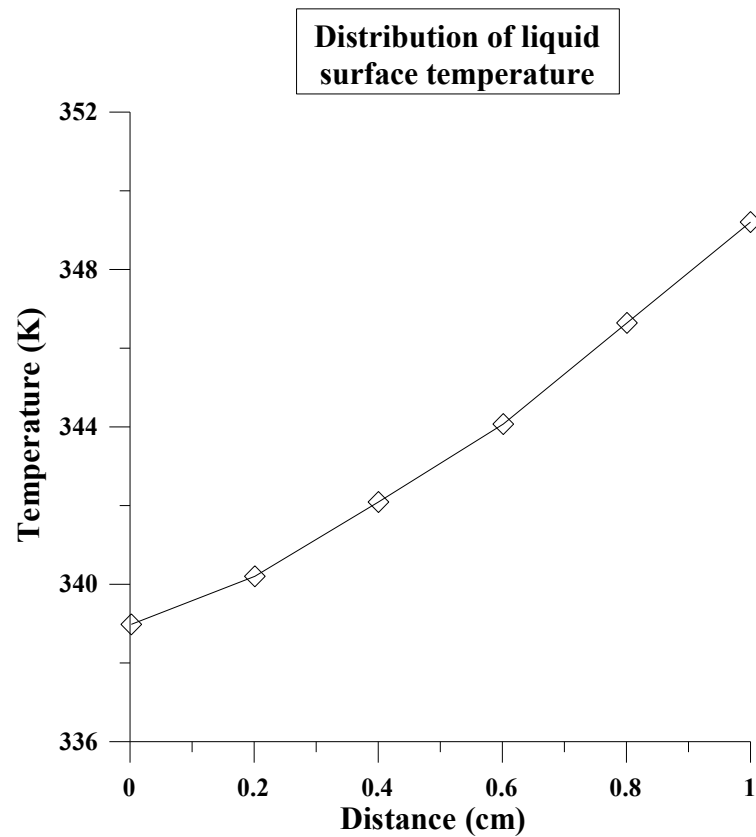
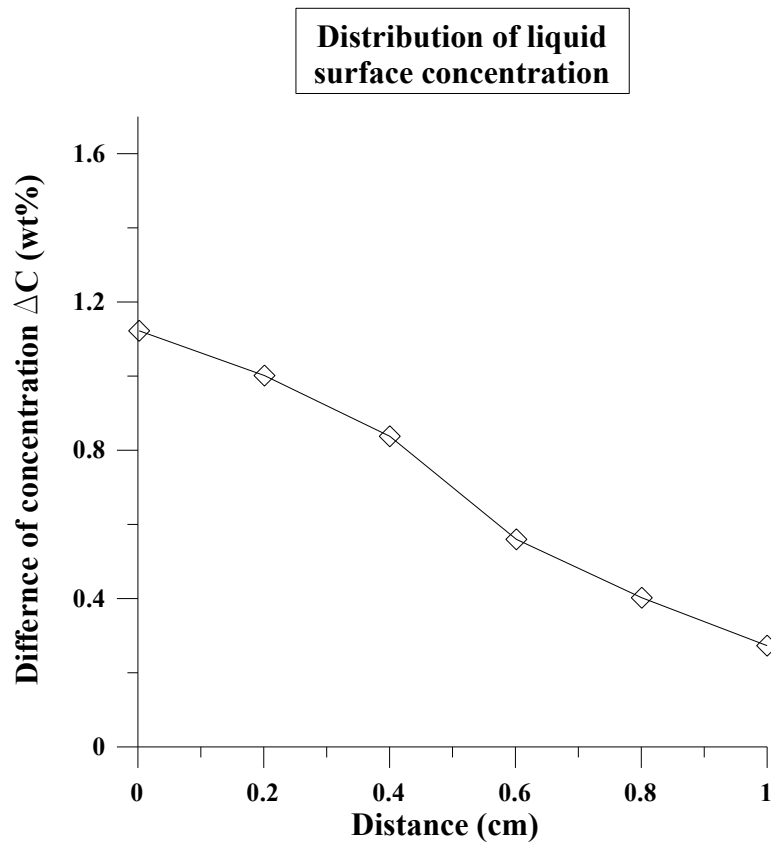


Figure 5.19 - Distribution of liquid surface temperature for water butanol mixture.



**Figure 5.20 - Distribution of liquid surface concentration.**

A thermal gradient of 10K and a concentration gradient of 1.2% have been founded. In the Table 5-5 the thermo-capillary effect and solutal Marangoni effect have been analyzed separately. The surface tension derivative for water self rewetting fluid has been evaluated by surface tension measurements. A positive mixtures has been considered, in this case the value has been founded in literature.

**Table 5-5 Comparison between different self-rewetting solutions and self-rewetting brine.**

Liquids	Classification	$\sigma_T \frac{\partial T}{\partial x} \left( \frac{dyne}{cm^2} \right)$	$\sigma_c \frac{\partial c}{\partial x} \left( \frac{dyne}{cm^2} \right)$
Water-Butanol (5%wt)	Self-rewetting	0,67	1,3
FP40 – Butanol (5%wt)	Self-rewetting	4,52	1,3*
Water-Ethanol	Positive Mixtures	-1,18	0,9**

\* has been hypothesized that the value are the same of water-butanol case

\*\* from literature.

In this configuration, thermo-capillary and solutal Marangoni effect for water/butanol solution are comparable and both give a positive contribute to the reverse Marangoni flow. Positive mixtures, already proposed as working fluids for heat pipe applications show a thermo-capillary effect that is high on comparison to solutal effect. So, this mixture cannot be used as working fluid for heat transfer application because, similar to ordinary liquids, thermo-capillary effect is negative.

In addition, improvement in self-rewetting behaviour can be avoid using self-rewetting brines. For this mixture the thermo-capillary effect is  $4/5$  times higher then the water/alcohols solution.

## 6 Conclusion and future research

The main objective of this work was to show the benefit of self-rewetting fluids in heat transfer device like heat pipe systems. Contrary to the ordinary working fluid, self-rewetting fluid show a reverse Marangoni flow at liquid-vapour interface that driven the liquid towards hot side. A number of different self-rewetting have been investigated and characterized trough extensive laboratory activities.

The main results include temperature and concentration distribution measurements by optical interferometric system for the water/alcohol solution; the results are original because highlighted self-rewetting behavior of such solutions and for the first time thermal and concentration effect has been simultaneous investigated.

In addition:

- new self-rewetting fluids with low freezing point have been identified and characterized;
- better thermal performances have been obtained for heat pipe filled with new self-rewetting fluids;
- the architecture of a flight payload, dedicated to the study of heat pipe filled with self-rewetting fluids in microgravity environment, has been defined.

The results on the surface tension behaviour of brine containing a small amount of Heptanol or Butanol may open new horizons towards more efficient heat transfer devices for different applications.

Future research regarding the use of suspension nanoparticle in self-rewetting fluids. Nanofluids are a new class of solid-liquid composite materials consisting of solid particles, with size typically in the order of 1-100nm, suspended in a heat transfer fluid. Nanofluids have attracted interest from scientific community owing to their greatly enhanced thermal proprieties [75].

More recently, study have show that is possible to realize self-rewetting nanofluids [76-77], i.e suspension of nanoparticles in self-rewetting fluid. This fluids can further improve the thermal performances of heat pipe systems.

## References

- [1] **Pierce, M.A.** *Theodore Newton Vail and the Boston Heating Company, 1886-1890*, <http://www.energy.rochester.edu/us/ma/boston/bhc>.
- [2] **Grover, G. M., Cotter, T. P. and Erikson, G. F.** Structures of Very High Thermal Conductivity. *J. Appl. Phys*, Vol. 35, 1964.
- [3] **Brennan, P.J., Krolczek, E.J.** *Heat Pipe Design Handbook, Vols. 1 and 2*. s.l. : B & K Engineering, 1979. NTIS n81-700113.
- [4] **Peterson, G.P.** *An Introduction to Heat Pipes: Modelling, Testing and Applications*. New York : John Wiley and Sons, 1994.
- [5] **Rea, D., Kew, P.** *Heat Pipes: Theory, Design, and Applications*. Butterworth-Heinemann, 2006.
- [6] **Hoa, C., Demolder, B., Alexandre, A.** Roadmap for developing heat pipes for ALCATEL SPACE's satellites, *Applied Thermal Engineerin.*, Vol. 23, 9, pp. 1099-1108, 2003.
- [7] **Wang, Y., Peterson, G.P.**, Investigation of a Novel Flat Heat Pipe, *Journal of Heat Transfer*, Vol. 127, pp. 165-170, 2005.
- [8] **Peterson, G.P.**, Analytical development and computer modelling of a bellows-type heat pipe for the cooling of electronic components, *Heat Transfer Engineering*. 1988, Vol. 9, 3, pp. 101-109.
- [9] **Maydanik, Y.F.** Loop heat pipes. *Applied Thermal Engineering* . 2005, Vol. 25.
- [10] **Vasiliev, L.**, Heat pipes in modern heat exchangers, *Applied Thermal Engineering*, 25, Vol. 25, 2003.
- [11] **Ku, J.**, Start-up issues in capillary pumped loops, *Ninth International Heat Pipe Conference*. Albuquerque, New Mexico, 1995.
- [12] **Swanson, T.D.**, Thermal control technologies for complex spacecraft, *Proceedings of the 13th IHPC*. Shanghai, China, 2004, pp. 1-11.
- [13] **Faghri, A.**, Heat Pipe Science and Technology, *Taylor & Francs, Washington, DC*. (1995).

- [14] **Seibert, G. et al**, A World Without Gravity – Research in Space for Health and Industrial Processes . *ESA SP-125*, June 2001.
- [15] **Monti, R.** *Physics of Fluids in Microgravity*. s.l. : Taylor and francis, 2001.
- [16] **Pratt M., Hallinan, K. P.** Thermocapillary effects on the wetting characteristics of a heated curved meniscus, *J. Thermophys. Heat Transfe*, Vol. 11, 1997.
- [17] **J. M. Ha, G. P. Peterson.** Analytical prediction of the axial dryout point for evaporating liquids in triangular microgrooves, *ASME J. Heat Transfer*, Vol. 116, p. 498, 1994.
- [18] **Pratt D.M., Kihm K.D.,** Binary Fluid Mixture and Thermocapillary Effects on the Wetting Characteristics of a Heated Curved Meniscus, *J. Heat Transfer.*, 125, pp. 867-874, 1997.
- [19] **Zhang, N. and Chao D.** Models for enhanced boiling heat transfer by unusual Marangoni effects under microgravity conditions. *Int. Comm. Heat Mass Transfer*, Vol. 20, 8, pp. 1081-1090, 1999.
- [20] **Abe, Y., Iwasaki, A., Tanaka, K.** Microgravity Experiments on Phase Change of Self-Rewetting Fluids, *Ann. N.Y. Acad. Sci*, Vol. 1027, pp. 269–285, 2004.
- [21] **Zhang, N., Chao, D.,** Models for enhanced boiling heat transfer by unusual marangoni effect under microgravity conditions, *Int. Comm. Heat Mass Transfer*, Vol. 26, 8, pp. 1081-1090, 1999.
- [22] **Zhang, N.,** Innovative heat pipe systems using a new working fluid, *Int. Comm. Heat Transfer*, Vol. 28, 8, pp. 1025-1033, 2001.
- [23] **Savino, R., Monti, R.** Heat pipes for space applications, *Space Technology*, Vol. 25, 1, pp. 59-61, 2005.
- [24] **Abe, Y.,** About Self-Rewetting Fluids – Possibility as a new working fluid, *Thermal Science & Engineering*, Vol. 8, 4, 2003.
- [25] **Abe, Y.** Heat Transfer with Self Rewetting Fluids. *Proceedings of IMECE-2005-79174: International Mechanical Engineering Conference & Exposition*, November 5-11, Orland, 2005.
- [26] **Vochten, R., Petre, G.,** Study of the heat of reversible adsorption at the air-solution interface, *Journal Colloid Interface Science*, Vol. 42, 2, pp. 320–327, 1973.

- [27] **Azouni, M.A., Normand, C.,Petre, G.**, Surface tension driven flows in a thin layer of a water-n-heptanol solution, *Journal Colloid Interface Science*, Vol. 239, 2, pp. 509–516, 2001.
- [28] **Chao, D. F., Zhang, N.**, Heat pipe systems using new working fluid, *US 6,448,940 B1 United States*, Feb. 3, 2004.
- [29] **Kuramae, M., Suzuki, M.**, Two components heat pipes utilizing the Marangoni effect, *Chemical Engineering of Japan*, 26, pp. 230–231, 1993.
- [30] **Kuramae, M.**, Condensation mechanism of binary mixture under a microgravity, *Proceedings of the 11th International Heat Pipe Conference*, Tokio, 1999.
- [31] **Kuramae, M.**, Numerical simulation of the Marangoni convection in a two component heat pipe. *Proceedings of the 37th National heat Transfer Symposium of Japan*, 2000.
- [32] **Abe, Y., Iwaski, A., Tanaka, K.**, Thermal Management With Self-Rewetting Fluids, *Microgravity sci. technol*, Vols. XVI - I , 2005.
- [33] **di Franciscantonio, N., Savino, R., Abe, Y.**, New alcohol solutions for heat pipes: Marangoni effect and heat transfer enhancement, *International Journal of Heat and Mass Transfer*, Vol. 51, pp. 6199–6207, 2008.
- [34] **Savino R., Paterna D.**, Marangoni effect and heat pipes dryout. *Physics of Fluids*, Vol. 18, 11, 2006.
- [35] **Suman, B.**, Effects of a surface-tension gradient on the performance of a micro-grooved heat pipe: an analytical study, *Microfluid Nanofluid*, Vol. 5, pp. 655–667, 2008.
- [36] **Savinoa, R., Franciscantonio, N., Fortezza, R., Abe, Y.**, Heat pipes with binary mixtures and inverse Marangoni effects for microgravity applications, *Acta Astronautica*, , Vol. 61, pp. 16 – 26, 2007.
- [37] **Abe Y.**, Applications of Self-Rewetting fluids as a Working fluid in Heat Transfer, *The Eighteenth International Symposium on Transport Phenomena*, 27-30 August, Daejeon, KOREA, 2007.
- [38] **Savino, R., di Franciscantonio, N., Fortezza, R., Abe, Y.**, Heat Pipes with Binary Mixtures and inverse Marangoni effects for microgravity applications, *Acta Astronautica*, Vol. 61, pp. 16-26, 2007.

[39] **Savino, R., Piccolo, C., Fortezza, R., Abe, Y.**, Heat pipes with self rewetting fluids under low-gravity conditions, *Microgravity Science & Technolog.*, Vol. XIX 3/4, pp. 75-77, 2007.

[40] **Savino, R., Di Paola, R., Cecere, A., Abe, Y., Tanaka, K., Nakagawa, M., Sato, M.** Self-Rewetting Fluid for Space Applications, *38th International Conference on Environmental Systems*. San Francisco, California, USA, June 29 - July 2, 2008.

[41] **Savino, R., Abe, Y., Fortezza, R.**, Comparative study of heat pipes with different working fluids under normal gravity and microgravity conditions, *Acta Astronautica*, Vol. 63, pp. 24 – 34, 2008.

[42] **Agostara, C., Dionisio, C., Di Salvo, A., Sgroi, G.**, MIOSAT: an Italian low-cost technological/scientific microsatellite, *59th International Astronautical Congress*, 29 September – 3 October 2008, Glasgow (Scotland).

[43] **Savino, R., Cecere, A., Di Paola, R., Abe, Y., Castagnolo, D., Fortezza, R.**, Marangoni heat pipe: an experiment on board MIOSAT italian microsatellite, *59th International Astronautical Congress*, 29 September – 3 October 2008, Glasgow (Scotland).

[44] **Tanaka, K., Abe, Y., Nakagawa, M., Piccolo, C., Savino, R.**, Low-Gravity Experiments of Lightweight Flexible Heat Pipe Panels with Self-Rewetting Fluids, *Ann. N.Y. Acad. Sci.*, 1161, pp. 554–561, 2009.

[45] **Fortescue, P., Stark, J., Swinerd, G.**, Spacecraft Systems Engineering (Third Edition), *s.l. : John Wiley & Sons*, 2003.

[46] **Wertz, J.R.**, Space Mission Analysis and Design, *Kluwer Academic Publishers (3<sup>^</sup> ediz.)*, 1999.

[47] **Gennes P.J, Brochard-Wyart, B., Quéré, D.**. Capillary and Wetting Phenomena — Drops, Bubbles, Pearls, Waves. *Springer*, ISBN 0-387-00592-7, 2002.

[48] **Adamson, A.W.** Physical Chemistry of Surfaces, *New York: Wiley interscience*, 1967.

[49] **Bashforth, S., Addams, J.C.**, An attempt to test the theory of capillary action, *London : Cambridge University Press and Deighthen*, Bell and Co, 1882.

[50] **Andreas, J.M., Hauser, E.A., Tucker, W.B. J.**, Boundary Tension by Pendant Drops, *J. Phys. Chem.*, Vol. 42, 7, pp. 1001-1019, 1938.

- [51] **Girault, H.H., Schiffrin, D.J. and Smith, B.D.V.**, Drop image processing for surface and interfacial tension measurements, *J. Colloid Interfaces Sci.*, v. 93 p. 169, 1984.
- [52] [http://www.dataphysics.de/english/produkte\\_oca-15+.htm](http://www.dataphysics.de/english/produkte_oca-15+.htm). [Online]
- [53] **Anastasiadis, S.H., et al.** The determination of polymer interfacial tension by drop image processing: comparison of theory and experiment for the pair, poly(dimethyl siloxane)/polybutadiene. *Polymer engineering and science* . 1986, Vol. 26, pp. 1410-1418 .
- [54] **Huh, H.; Reed, R.L. J.**, A method for estimating interfacial tensions and contact angles from sessile and pendant drop shapes, *Colloid Interface Sci*, Vol 91, Issue 2, February 1983, pp 472-484, 1983.
- [55] **Savino R., Di Paola R., Cecere A., Fortezza R.**, Self-wetting heat transfer fluids and nano-brines for space heat pipes, *60th International Astronautical Congress*, 12-16 Oct, Deajeon, Republic of Korea, 2009.
- [56] **Perry, R.H. and Green, D.W.**, Perry's Chemical Engineers' Handbook (7th Edition), *McGraw-Hill*, 1997.
- [57] **Savino R., Cecere A., Di paola R., Abe Y., Castagnolo D., Fortezza R.**, Marangoni heat pipe: an experiment on board MIOsat microsatellite, *Acta Astronautica*, 65 (2009), pp. 1582–1592, doi:10.1016/j.actaastro.2009.04.005.
- [58] **Chi, S. W.**, Heat Pipe Theory and Practice, *McGraw-Hill*, New York, 1976.
- [59] **Veddu, U. V., Garimella, S. V., Murty, J.** Transient three-dimensional modelling of flat heat pipes with discrete heat sources. *CTRC Report 2004-01*. August 2004.
- [60] **Savino R., Cecere, A., Di Paola, R.**, Surface tension-driven flow in wickless heat pipes with self-wetting fluid, *International Journal of Heat and Fluid Flow*, 2009, Vol. 30, pp. 380–388.
- [61] **Villers, D., Platten, K.**, Influence of interfacial tension gradients on thermal. *Applied Scientific Research* . Vol. 47, pp. 177-191, 1990.
- [62] **Petre, G., Azouni, M. A., Tsinyama, K.**, Marangoni convection at alcohol aqueous solutions-air interfaces, *Applied Scientific Research*, pp. 97-106, 1993.
- [63] **Petre, G., Azouni, M. A.**, Experimental evidence for the minimum of surface tension with temperature at aqueous alcohol solution/air interfaces, *J. Colloid Interface Sci.*, 98, pp 261-263, 1984.

[64] **Petre, G., Azouni, M. A., Tshinyama, K.,** Marangoni convection at alcohol aqueous solutions-air interfaces, *Appl. Sci. Res.*, 50, 97, 1993.

[65] **Azouni, M. A., Petre, G.,** Experimental Evidence of the Effect of Evaporation-Condensation on Thermal Marangoni Flows in Aqueous Fatty Alcohol Solutions, *J. Colloid Interface Sc.*, 206, 332, 1998.

[66] **Hansen, R.,** The theory of diffusion controlled absorption kinetics with accompanying evaporation, *J. Phys. Chem.* 64, pp. 637–641, 1960.

[67] **Hommelen, J.,** The elimination of errors due to evaporation of the solute in the determination of surface tension, *J. Colloid Interface Sci.* 14, 385, 1959.

[68] **Ecker, A.,** Two-wavelength holographic measurement of temperature and concentration during alloy solidification, *J. Thermophys. Heat Transf.*, Vol. 2, pp. 193–196, 1988.

[69] **Mehta, JM,** Dual wavelength interferometric technique for simultaneous temperature and concentration measurement in liquids, *Appl. Opt.*, Vol. 29, pp. 1924–1932, 1990.

[70] **Vikram, CS, Witherow, WK,** Critical needs of fringe-order accuracies in two-color holographic interferometry, *Exp. Mech.*, Vol. 32, pp. 74–77, 1992.

[71] **Takeda, M., Ina, H., Kobayashi, S.,** Fourier-transform method of fringe-pattern analysis for computer-based topography and interferometry, *J. Opt. Soc.*, Vol. 72, 1, January 1982.

[72] **Duan, L., Kang, Q., Sun, Z. W., Hu, L., Cui, H. L.,** The Real-Time Mach-Zehnder Interferometer used in Space Experiment, *Microgravity Sci. Technol.*, Vol. 20, pp. 91–98, 2008.

[73] **Herráez, M. A., Burton, D.R., Lalor, M.J., Gdeisat, M.A.,** Fast two-dimensional phase-unwrapping algorithm based on sorting by reliability following a noncontinuous path, *Appl. Opt.*, Vol. 41, pp. 7437-7444, 2002.

[74] **Vikram, C. S., Witherow, W. K.,** Two color interferometry with nonlinear refractive properties, *International Journal for Light and Electron Optics*, Vol. 114, 3, pp. 118–122, 2003.

[75] **Jacopo, B. et al,** A Benchmark Study on the Thermal Conductivity of Nanofluids, *Journal of Applied Physics*, Vol. 106, pp. 094312, 2009.

[76] **Sato M., Suzuki T., Di Paola R., Urita Y., Cecere A., Savino R., Abe Y., Iimura K., Shinmoto Y., Ohta H., Fukagava M.** Anomalous Temperature Dependence of the Surface Tension in

Polyol-Process-Synthesized Silver Nanofluids with Higher Alcohols, *Sixth Interdisciplinary Transport Phenomena Conference: Fluid, Thermal, Biological, Materials and Space Sciences*, October 4-9, Volterra (Tuscany), Italy, 2009.

[77] **Sato M., Abe Y., Urita Y., Di Paola R., Cecere A., Savino R.**, Thermal Performance of Self-rewetting Fluid Heat Pipe Containing Dilute solutions of Silver Nanoparticles Synthesized by Microwave-Polyol Process, *Sixth Interdisciplinary Transport Phenomena, 17th Symposium on Thermophysical Properties*, June 21 - 29, Colorado, Usa, 2009.